Study of the flow in a hydrocyclone using positron emission particle tracking and computational fluid dynamics simulation

Yu-Fen Chang

Dissertation for the degree of philosophiae doctor (PhD)

at the University of Bergen

2016

Dissertation date: 22.06.2016

Acknowledgements

I would like to thank my supervisor Prof. Alex C. Hoffmann, for educating, developing, and guiding me. Thank you for leading me into the fascinating world of cyclones and the PEPT technique. Thank you for being a lighthouse and a knowledge-teeming well for me. Thanks for your trust, patience, and comprehensive help. Words are never enough for expressing my gratitude to Prof. Hoffmann.

I would like to thank my colleagues in the group of Multiphase systems and energy science and technology. Thanks for all your company, sharing, and support. Special thanks go to Dr. Gleb I. Pisarev: Thank you for teaching me the CFD knowledge and technique step by step unweariedly. Thank you for always bringing in a sprightly atmosphere. It would be impossible for me to work out the complexity in such an instant without your help. Special thanks to Maryam Ghaffari: Thank you for sharing your thoughts and viewpoints, enlivening me, and laughing with me.

Dr. Michael E. Casey from Siemens is appreciated for explaining the Siemens PET camera. Dr. Tom C.H. Adamsen and staff from Centre for Nuclear Medicine and PET, Haukeland University Hospital are appreciated for their sophisticated techniques and equipment support.

Staff of the Department of Physics and Technology in University of Bergen are appreciated for assistance and establishing a professional yet cosy environment. With special thanks to Leif Egil Sandnes in the mechanical workshop at the University of Bergen for helping with the experimental systems. Norges forskningsråd (Research Council of Norway) and Aker Solutions are appreciated for funding this work.

I would like to thank my Bergen friends for filling my heart and my stomach. 'Home is where friends always belong.' Thank you for making me a home.

Thanks for everyone who walked and has been walking with me on my road of learning. I hope to exert myself to give, like you did to me.

Abstract

This thesis presents my work of studying the flow in a hydrocyclone using positron emission particle tracking (PEPT) and computational fluid dynamics (CFD) simulation. Hydrocyclone separators are a type of cyclone separators with liquid as the carrier phase. Applications of the hydrocyclones can be found in numerous diverse industries.

The thesis starts with an introduction of cyclone and hydrocyclone separators (Chapter 1). Theoretical models are described to enunciate the physics of the separation process. The anterior experimental Lagrangian studies and numerical studies of the flow in (hydro)cyclones, both of which are related to the research approaches used in this work, are reviewed.

In Chapter 2 the 'end of the vortex' (EOV) phenomenon, which is observed by PEPT and analyzed in this work, is introduced. Most prior researches about the EOV, including experimental and theoretical studies, targeted the gas cyclones. Here, implicit and direct experimental observations of EOV in gas cyclones and swirl tubes are reviewed, followed by more detailed analysis of the flow field at the EOV area, the influencing factors and the consequences.

In Chapter 3 the positron emission particle tracking (PEPT) technique used to track the particles and quasi-fluid elements is explicated. The essentials of this technique—the camera, the tracer and labelling technique, and data processing algorithms, are expounded.

Chapter 4 gives a summary of papers included in this thesis and some unpublished results. Concluding remarks and suggestions for further work on the cyclone and EOV as well as PEPT technique are given in Chapter 5. The papers are displayed in Chapter 6. **Paper I** reports the first set of particle trajectories obtained using PEPT with the first version of the refined data processing algorithms. The tracks and some preliminary analyses have indicated the occurrence of the EOV phenomenon in the hydrocyclone. This is the first time that the trajectories in a hydrocyclone are obtained with such high temporal and spatial resolutions. The clearly observed influence of EOV on the particles is also unprecedented. In **Paper II** the flow field of the EOV phenomenon in a hydrocyclone is successfully simulated for the first time using the LES (large eddy simulation) turbulence model. **Paper III** gives a detailed account of the development and verification of the algorithm used thus far, which is the foundation of the further developed variations of algorithm. In **Paper IV** PEPT was utilized to compare the tracks and flow patterns in the hydrocyclone operated under different conditions. An abnormally long residence time of the particle in the hydrocyclone under certain operational conditions was observed. An algorithm finding the cyclone axis and transforming the particle Cartesian positions to cylindrical coordinates was developed. The cylindrical positions and velocity components as a function of axial position and time show in detail the peculiar flow pattern caused by the EOV. The section where

the anomalous flow field appeared and the time the particle wandered in the EOV area were specifically determined. In **Paper V** the 3-D particle trajectory was simulated using Lagrangian tracking in the fluid field calculated using the LES turbulence model. The characteristics of the simulated and PEPT-obtained particle tracks conform to each other very well. The superposition of simulated particle trajectories on the static pressure shows how the particle behavior is influenced by the EOV. The goal of **Paper VI** is to follow neutral-density particles to study the flow of the fluid elements. The flow condition was modified to render the tracer neutrally buoyant, which, however, created a difficult tracking condition where radioactivity dispersed into the fluid due to ion exchange. A new tracking strategy was developed to cope with the decreasing signal-to-noise ratio. Several smoothing strategies were also employed to de-noise, and their effects and applicability were scrutinized. The tracks of neutral-density tracers reveal the pathlines of quasi-fluid element. The cylindrical velocity components derived using the aforementioned coordinate-transformation algorithm makes it possible to study the flow patterns close to the tangential inlet and in the cyclone body. The tangential velocities as a function of radius were fitted using theoretical formulae, which yielded the parameters necessary for describing the tangential velocity profile. Cylindrical velocity components as a function of time show the correlations between the different velocity components, which elucidates the separation process and principle.

The unpublished results in Section 4.2 include CFD simulations of a hydrocyclone using the LES turbulence model and Lagrangian particle tracking for understanding the effect of the underflow discharge on the 'end of the vortex' phenomenon and the associated flow field and particle tracks. The difference between 20% and no underflow discharge is significant. The characteristics of simulated particle tracks under conditions of different underflow discharge conform to experimental particle tracks obtained using the PEPT technique.

During the series of studies, the algorithm for positioning the tracer has been continuously developed, improved and verified, which means that the temporal and spatial resolutions, as well as the data processing efficiency continually improved.

List of papers

Papers included in the thesis

1. Y.-F. Chang, C. G. Ilea, Ø. L. Aasen, and A. C. Hoffmann. Particle flow in a hydrocyclone investigated by positron emission particle tracking. *Chemical Engineering Science*, 66(18):4203–4211, 2011.

2. Y.-F. Chang, G. I. Pisarev, and A. C. Hoffmann. Numerical study of the "end of the vortex" phenomenon in a hydrocyclone separator. *AIP Conference Proceedings*, 1389(1):183–186, 2011.

3. Y.-F. Chang, T. C. H. Adamsen, and A. C. Hoffmann. Using a PET camera to track individual phases in process equipment with high temporal and spatial resolutions: Algorithm development. In *Proceedings of 2012 IEEE International Instrumentation and Measurement Technology Conference (I2MTC)*, pages 2326–2330, 2012.

4. Y.-F. Chang, Å. Skorpen, D. Fonnes, and A. C. Hoffmann. Detecting anomalies in the separation process in a hydrocyclone using a medical PET scanner. In *Proceedings of the 6th International Symposium on Process Tomography*, 2012.

5. Y.-F. Chang, T. C. H. Adamsen, G. I. Pisarev, and A. C. Hoffmann. PEPT: An invaluable tool for 3-D particle tracking and CFD simulation verification in hydrocyclone studies. *European Physical Journal Web of Conferences*, 50:05001p.1–p.8, 2013.

6. Y.-F. Chang and A. C. Hoffmann. A Lagrangian study of liquid flow in a reverse-flow hydrocyclone using positron emission particle tracking. *Experiments in Fluids*, 56(1):1–14, 2015.

Papers not included in the thesis

1. Y.-F. Chang, C. G. Ilea, Ø. L. Aasen, and A. C. Hoffmann. Particle trajectories in a hydrocyclone measured by PEPT. In *FILTECH 2011 Conference Proceedings*, volume 1, pages 173–180, 2011.

2. S.-A. Marthinussen, Y.-F. Chang, B. Balakin, and A. C. Hoffmann. Removal of particles from highly viscous liquids with hydrocyclones. *Chemical Engineering Science*, 108(0):169–175, 4 2014.

Contents

Chapter 1

Cyclone separators

1.1 Introduction

Cyclones are one of the most widespread equipment for separating mixtures composed of substances of different densities [1]. Their advantages include simple construction, low pressure drop, variable separation range and easy operation. In addition, cyclones are applicable in difficult conditions, such as extreme pressure and temperature, and in chemically aggressive environments.

The separation principle of cyclones is based on enhanced settling of particles in the centrifugal field. As a particle is subjected to a centrifugal field, the general equation of motion for a particle in a Newtonian fluid can be expressed as:

$$\binom{mass}{times\ acceleration} = \binom{centrifugal}{force} - \binom{fluid}{drag} - (buoyancy) - \binom{added}{mass} - \binom{Basset}{force} \qquad (1.1)$$

The two last terms on the right-hand side of of Eq. 1.1 relate to fast, unsteady motion. The 'added mass' term arises from that during acceleration of a particle from rest, the surrounding fluid must also be accelerated. This appears as 'added mass' to the particle. The Basset force is associated with that the acceleration of the particle relative to the velocity of the surrounding fluid can lead to a time-varying viscous force as the flow pattern around the particle changes. These two terms are zero in steady movement. Practical plant experiences with hydrocyclone design and operation indicates that it is not necessary to include either the added mass or the Basset terms.

To utilise the principle of enhanced settling, the geometry of cyclones is designed to cause the mixture to flow in a swirling pattern. Schematic geometries of two types of the reverse-flow cyclones are shown in Figure 1.1. Figure 1.1 (a) is the cylinder-on-cone type and (b) shows the swirl tube type. After entering the separation space through the inlet, the mixture flows in a helical path, and due to the centrifugal force the components of higher density would be flung onto the wall. Due to the pressure distribution in the cyclone, the lighter continuous phase, normally the gas or liquid, turns its axial direction,

forming an inner vortex swirling towards the overflow outlet, also called the vortex finder. In the cyclone the pressure gradient can cause the particle being subjected to a force akin to the buoyancy force. This force is negligible as the particle density is much higher than that of the carrier fluid.

Under steady state condition in the centrifugal field the particle will be centrifuged outward resisted by drag, and will move with a terminal velocity of:

$$U_r = \frac{x^2(\rho_p - \rho_f)}{18\mu}\left(\frac{{v_\theta}^2}{r}\right) \tag{1.2}$$

where x is particle diameter, ρ_p is the particle density, ρ_f is the fluid density, μ is fluid viscosity, v_θ is the particle tangential velocity, and r is radius of swirl motion.

This outward movement of the particle is faster as the difference between the particle density and the fluid density increases. Also the particles with bigger size or higher tangential velocity are flung outwardly faster.

In addition to its mean movement, a particle in a hydrocyclone also undergoes a small scale, fluctuating motion in response to the local turbulence in the fluid. This is more severe for smaller particles, which are most affected by the fluctuations in the fluid velocity due to their smaller dynamic response time. The turbulent motion gives rise to some dispersion and mixing of the particles.

The term 'hydrocyclone' is used when the carrier fluid is a liquid rather than a gas and the cyclone is applied to separate mixtures containing liquid. Hydrocyclone for solid/liquid separation is the objective of this work.

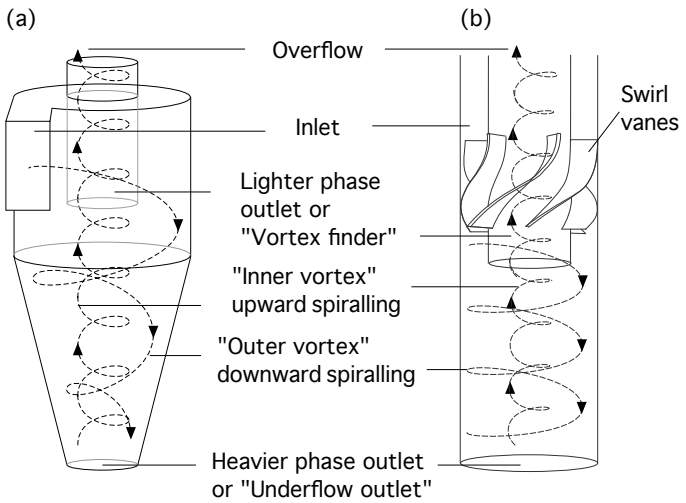

Figure 1.1: Schematics of the hydrocyclone separator with (a) cylinder-on-cone design and (b) swirl tube design.

Despite the simple principle and uncomplicated construction of the cyclone, the designs of the parts, including inlet, cone section, underflow outlet, vortex finder, total length,

and roof, affect the flow field and consequently the separation efficiency, and thus require sophisticated considerations [1]. For instance, shorter vortex finder may lead to some reduction in overall pressure loss. But if the vortex finder is too short (on the order of half that of the inlet height, or less), some fraction of the incoming mixture will tend to pass directly from the inlet to the vortex finder, which 'short circuits' the cyclone and decreases separation performance. A sophisticated method to reveal the flow field is therefore vital for understanding the differences between various designs and subsequently improving the design.

Apart from the geometry design, the operation conditions, e.g. inlet velocity and underflow fraction, also influence the flow field and the performance of the cyclones to a great extent.

The underflow fraction, a fraction of the total inflow that flows out of the underflow outlet, is an important variable in hydrocyclone operations. For instance, the underflow density can be adjusted by altering the underflow discharge rate. If the solids content in the feed varies, automatic underflow regulators, as those used in Ref. [2], helps keeping the underflow density stable. However, how the underflow affects the flow field in hydrocyclones has not been investigated systematically.

Therefore, to investigate and understand the flow characteristics in hydrocyclones, e.g. the velocity field and pressure field, under various operating conditions would allow utilising hydrocyclones in a reasonable and optimal manner.

1.2 Models for deriving separation performance

There are in principle two modeling concepts for cyclone separation efficiency in the literature: the 'equilibrium-orbit' models and 'time-of-flight' models.

1.2.1 Equilibrium-orbit models

Imagining a cylindrical control surface (CS) that is formed by continuing the vortex finder wall to the bottom of the cyclone, the equilibrium-orbit models consider the centrifugal force and the inward drag force acting on the particle, which is rotating in CS [3]. If the two forces are in balance the particle will not move inward or outward. The particle size for which the two forces balance (the size that orbits in CS) stands a 50-50 chance of being captured and is taken as the 'cut size' x_{50} of the cyclone.

The forces acting on a particle rotating in CS are:

- the outwardly directed centrifugal force with a magnitude of $\frac{\pi x^3}{6}(\rho_p - \rho_f)\frac{{v_{\theta CS}}^2}{R_x}$, where R_x is the radius of CS, and
- the inward Stokesian drag caused by the fluid flowing through, and normal to, surface CS and into the inner part of the vortex: $3\pi x \mu v_{rCS}$.

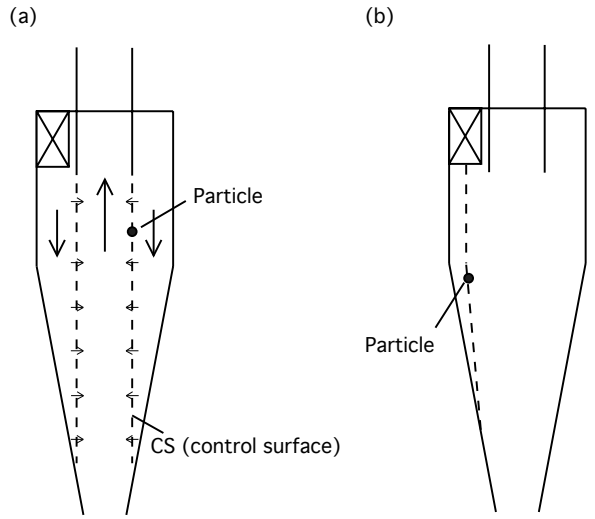

Figure 1.2: Sketches showing the concept of (a) the 'equilibrium-orbit' models and (b) the 'time-of-flight' models.

The centrifugal force is proportional to the particle mass and therefore to x^3, while the Stokesian drag is proportional to x. Large particles are therefore 'centrifuged' onto the hydrocyclone wall, and small particles are dragged in and escape through the vortex finder.

Equilibrium-orbit theory is useful in correlating and explaining the relation between flow rate, velocity field, and hydrocyclone cut size. It, however, does not account for the pressure drop, nor the sharpness of the grade-efficiency curve. It does not fully explain the consequence of the cyclone length either. Extending length increases the surface area and hence imposes an additional friction on the flow. The increase in friction weakens the rotation in the inner vortex. A less intensive vortex means less centrifugal force on the particles in CS. On the other hand, the equilibrium orbit model does account for the radial velocity across a longer CS being less in a longer cyclone, so that the inward drag on a particle in CS is also reduced. The net result of these to opposing effects cannot be predicted with certainty.

1.2.2 Time-of-flight models

The time-of-flight models consider whether a particle, injected at some lateral position in the inlet, had the time to reach the cyclone wall and be collected before reaching the cyclone bottom. The total path length for a particle swirling close to the wall (assumed cylindrical) is: $2\pi R_{in} N_s$, where N_s is the number of spiral turns the particle takes on its way toward the bottom of the cyclone. The incline in the spiral path is neglected.

$$\text{The time the particle takes to reach the bottom} = \frac{2\pi R_{in} N_s}{v_{in}}. \tag{1.3}$$

The time required for the particle in the centrifugal field in the radial direction to reach the wall is:

$$\frac{R - R_{in}}{v_t}. \tag{1.4}$$

The terminal velocity, v_t, of a particle is:

$$v_t = \frac{x^2(\rho_p - \rho_f)}{18\mu}\left(\frac{{v_{in}}^2}{R_{in}}\right). \tag{1.5}$$

Eq. 1.6 must be satisfied in order that the particle reached the cyclone wall before reaching the cyclone bottom.

$$(R - R_{in})\left(\frac{18\mu}{x^2(\rho_p - \rho_f)}\right)\left(\frac{R_{in}}{{v_{in}}^2}\right) \leq \frac{2\pi R_{in} N_s}{v_{in}} \tag{1.6}$$

The particle size x must be above a critical value, which is the 'cut size' x_{50}.

In order to derive x_{50}, the number of spiral turns in the cyclone N_s has to be measured or estimated. Zenz [4], based on experience, obtained N_s as a function of inlet velocity. Rietema [5] related a part of the Eq. 1.6 to total pressure drop Δp over the cyclone and the derived result shows that x_{50} is inversely proportional to the square of the pressure drop and inversely proportional to the cyclone length H, as shown in Eq. 1.7 [1]:

$$C_{y50} := \frac{{x_{50}}^2\left(\rho_p - \rho_f\right)}{\mu} H \frac{\Delta p}{\rho_f Q}, \tag{1.7}$$

where Q is the volumetric flowrate through the cyclone and C_{y50} is a characteristic cyclone number only dependent on geometry.

Although the time-of-flight modeling concept is entirely different in nature from the equilibrium-orbit concept, the resulting efficiency models agree well over a wide range of cyclone designs. Having said that, the behavior of the cyclone vortex is not so simple. For instance, the pressure drop is strongly affected by the diameter of the vortex finder D_x. Supposedly reducing D_x would increase the pressure drop and reduce x_{50}. However, decreasing D_x increases the vortex core spin velocity and tends to reduce the stability of the vortex, which can further cause the 'end of vortex' phenomenon to occur low in the cyclone (to be explained further in Chapter 2).

Even though some models successfully predict the trends in cut size and pressure drop with cyclone body length up to a certain limit, none of the models account for the 'end of vortex' phenomenon, which limits the length of cyclones in practice, or makes performance predictions very uncertain. Therefore investigating the behavior of the 'end of vortex' phenomenon to eventually incorporate this into the theoretical consideration has been a focus of this thesis work.

1.3 Experimental Lagrangian studies of flow in (hydro)cyclones

Experimental Lagrangian studies of the highly turbulent, swirly flow in (hydro)cyclones is not easy, and therefore the records in literature are scarce compared to numerical Lagrangian studies. Peng et al. [6] reported tracking helium-filled soap bubbles as neutrally buoyant tracers in a swirl-tube gas-solid separator using high speed photography. The neutral density bubbles reveal the internal features of the flow and the vortex core, which either centralizes and extends to the bottom of the hopper under the swirl tube, or bends to, and precesses around, the wall of the separator under some conditions, the later is an anomalous phenomenon referred to as the 'end of the vortex' (EOV), as to be explained in Chapter 2.

Chan et al. [7] used positron emission particle tracking (PEPT) to track particles of sizes below 150 μm in gas-solid cyclones under various solids-loading conditions. The particle is located every 4 ms and the spatial resolution is not specified. The PEPT result shows that: At low solids loadings, particles spiral in the cylindrical and the conical sections. At higher solids loadings, particles are captured in the dense wall layer, which moves downward along the wall in the conical section.

Particle trajectories in a hydrocyclone has been obtained by tracking vegetable seeds of 700–900 μm using high-speed camera [8]. Various type of particle routes have been observed depending on the particle size and the entering position at the inlet. In the case of longer residence time, the particle swirls towards the underflow outlet along the cyclone wall while for a few times being drawn to the inner vortex and swirling towards the overflow for a while. The temporal and spatial resolutions of the technique as well as the unit of the cyclone dimensions used in this study are however not given [8].

In this thesis we investigated in detail the trajectories and velocities of the particles and fluid elements, as well as the flow field in a hydrocyclone by using the positron emission particle tracking (PEPT) with verified high temporal and spatial resolutions.

1.4 Numerical simulations of particle flow in (hydro)cyclones

In contrast to the scarce experimental Lagrangian studies for (hydro)cyclones, the numerical methods for investigating the flow and obtaining the pathlines have been actively developed and giving more detailed results. To simulate the complicated swirling turbulent flow in a cyclone requires sophisticated numerical techniques and careful consideration on the turbulence models. It has been reported that the $\kappa - \epsilon$ turbulence model and its variants are inadequate to simulate highly swirling turbulence flow in cyclone separators due to the assumption of isotropic turbulence structure in the formulation [9, 10]. Since the solid loading and volume fraction of dispersed solid particles in (hydro)cyclone separators are usually very small, the particle-particle interaction and

the effect of the dispersed phase on the continuous phase are usually ignored in the simulation of the (hydro)cyclone separators (i.e. one-way coupling). Below some of the studies employing different turbulence models, giving simulated trajectories, will be reviewed.

A simulation conducted by Boysan et al. (1982), as shown in Ref. [11], using a stochastic model to include the influence of the carrier (gas in this case) turbulence on the particle trajectory, shows that the smaller particle swirls close to the wall towards the underflow outlet while being drawn into the inner vortex and swirling towards the overflow outlet for several times. On the cross-section containing the cyclone axial axis, the particle seems to be trapped in a loop and experience recirculation. The random velocity as a result of the stochastic turbulence modelling can be observed on the simulated particle paths. Both recirculation and random velocity were uniquely obtained in this study. As can be seen in other numerical studies discussed below, no such phenomena were shown in the simulated trajectories. However, recirculation has been observed in our PEPT experiments and computational fluid dynamics (CFD) simulation. Random velocity is pronounced as observed by PEPT in some sections of the hydrocyclone under certain operational conditions.

Hsieh and Rajamani [12] obtained 2-D trajectories of particles in a hydrocyclone with various particle sizes and injection positions using modified Prandtl mixing-length model. The particle-fluid momentum coupling is assumed negligible. The liquid-phase flow field is calculated first and then the velocities of the particles with respect to the fluid is computed.

In the research of Krebs Engineers [13] computational fluid dynamics (CFD) is demonstrated as a development tool to eliminate the need to fabricate and test each new hydrocyclone design concept. A higher-order Reynolds stress turbulence model was chosen because it gave good agreement with known velocity profiles. The flow-splits at different vortex finder sizes and particle recovery curves show good agreement between simulations and measurements. Once the flow field has been calculated, the solids are introduced as a post processing stage using Lagrangian particle modeling. The simulated paths of particles of various sizes and in different cyclone geometries were obtained.

Bernardo et al. [14] used Reynolds stress model (RSM) to simulate the flow field inside the gas-solid cyclones with varied inlet section angles. The Eulerian equations were solved for the fluid phase and then Lagrangian equations of motion were integrated for the dispersed phase by tracking individual particles through the flow field. The simulated trajectories depict the influence of different inlet-section angles on the particle traveling route and particle residence time.

Shukla et al. [15] employed the Reynolds stress turbulence model with various discretization schemes to simulate the flow field in a Stairmand gas-particle cyclone, executed in the CFD code Fluent. The trajectories of particles were determined by Lagrangian particle tracking. Particle trajectories of various sizes from the CFD simulation using a trapezoidal scheme were shown. Comparing the modeled grade efficiency curve and cut size using different discretization schemes with the experimental data show that only high order schemes (i.e. Runge-Kutta and trapezoidal) predictions agree very well with the measured values for the entire grade efficiency curve.

Pisarev and Hoffmann [16] used the Large Eddy Simulation (LES) turbulence model to simulate the transient flow pattern in a swirl tube gas/particle separator. The simulated flow field shows that the 'end of the vortex' (EOV) develops at some swirl tube body lengths and certain inlet flowrates. The particles are tracked individually in the flow field by Lagrangian particle tracking. How the EOV influences the particle motion and separation performance is investigated numerically.

Numerical simulations using various turbulence models can be verified and compared with measured flow patterns, pressure drop, flow-splits and the separation efficiency in cyclones. However, it is not easy to compare the simulated trajectories with measurement due to the difficulties in tracking particles with high precision in highly turbulent and complex flow field. In this work we developed the high-resolution particle tracking technique—PEPT, obtained the trajectories in a hydrocyclone under various operation conditions and compared with simulated particle tracks.

Chapter 2

The end of the vortex (EOV)

2.1 'End of vortex' phenomenon

Most of the models of cyclone and swirl tube predict that longer separators perform better, at least considerably longer than the lengths of most commercially available cyclones. Since the inception of the cyclone it has been known that the cyclone or swirl tube cannot be made arbitrarily long. If it is too long, the vortex would destabilize, attach to the side wall (i.e. the vortex core bends), and turn around or 'precesses' around the wall at a high rate, which degrades the performance. Such a phenomenon, known as the 'end of the vortex' (or 'vortex precession') can be observed, perhaps most easily, in liquid swirl tube, where the gas bubbles in the core makes the vortex end's attaching to the wall visible (see Figure 2.1 [1]).

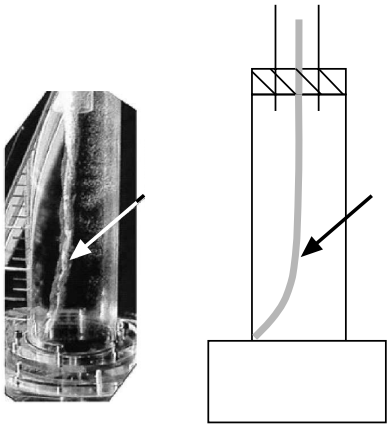

Figure 2.1: The 'end of the vortex' observed in liquid swirl tube [1]. The arrow indicates the vortex core's bending and precessing around the wall. Reprinted from Ref. [1] with permission from Springer Science and Business Media.

The 'end of vortex' phenomenon has been investigated in mainly gas cyclones and swirl tubes. Below gives a review of the experimental observation, numerical simulations, consequences, affecting factors and rationale of the 'end of the vortex'.

2.2 Experimental observation of EOV in gas cyclones and swirl tubes

As general theories and simulations predict, the vortex within a cyclone centralizes and extends down into an open space below the cyclone, where the vortex dissipates or ends on the bottom of the particle collecting chamber. However, in reality a vortex may attach to a surface such as the lower conical/cylindrical walls, or dust hopper, or the top of a dipleg.

The appearance of the 'end of the vortex' has been implied in an early study of erosive wear within a variety of steel cylinder-on-cone gas cyclones with tangential inlets [17]. Sotrch and Pojar [17] measured erosion rates along each cyclone's length as a function of inlet velocity and solids concentration for two different types of abrasive dust: the corundum and ash. The wear is summarised after injecting a fixed total quantity of dust. Plotting the erosion as a function of the axial position shows a peak within the lower cone in some of the cyclone geometries fed with corundum particles. After this peak the erosion magnitude falls off abruptly. As noted in Ref. [1], these peaks in the lower cones were deemed as the results of the vortex instability that caused the 'end' of the inner vortex to attach to, and precess around, the lower cone walls.

Hoffmann et al. [18] observed a closed ring formed at a certain position in the tube section below the cyclone conical section at higher inlet velocities by injecting smoke consisted of condensed vapours of paraffin oil (see Figure 2.2 (b)). This tube section below the cyclone conical section connects the bottom of the cyclone to the dust collection hopper, as shown in Figure 2.2 (a), turning the vortex so that the vortex would not extend into the dust collection hopper and re-entrain already collected dust. A similar method of turning the vortex is often used in industrial cyclone designs. It was found that above a certain inlet velocity the vortex length increased (the ring moves downward) with increasing inlet velocity under otherwise similar conditions (while no clear tendency below that certain inlet velocity). Also, above that certain inlet velocity, smaller vortex finder and higher dust loading had the effect of reducing the vortex length. While the narrow vortex finder was used, after a tracer in the form of a mist had been introduced, the vortex length increased as the wall of the cyclone dried and the apparent wall roughness decreased. The cyclone performed well when the vortex end was in the tube section underneath the conical section. When the vortex end moved up into the conical section, the separation performance dropped considerably and became erratic.

Alexander (1949) [19] has done the pioneering work in predicting the vortex length, i.e. the distance from the bottom of the vortex finder to the position of the 'end of the vortex' (L_n) as shown in Eq. 2.1, where D is the diameter of cyclone cylinder, D_x is the diameter of the vortex finder, a is the length of the inlet, and b is the width of the inlet. But the relation does not predict the strong variation with solid loading, which can also affect the wall roughness, nor the influence of the geometry as observed in Ref. [18].

$$\frac{L_n}{D} = 2.3\frac{D_x}{D}\left(\frac{D^2}{ab}\right)^{1/3} \tag{2.1}$$

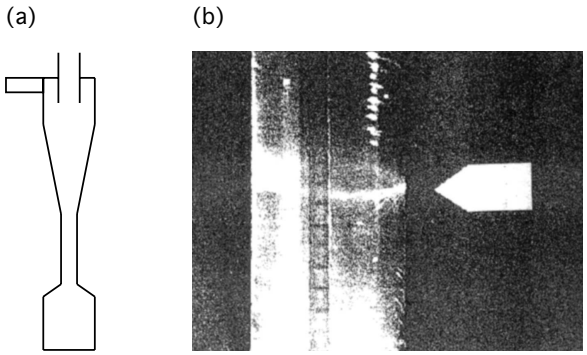

Figure 2.2: (a) The tube section below the cyclone conical section connects the bottom of the cyclone to the dust collection hopper. (b) The ring formation in the tube section underneath a cylinder-on-cone cyclone. Reprinted from Ref. [18], Copyright 1995, with permission from Elsevier.

As discussed above, due to the unsteady nature of the cyclone vortex, both the equilibrium-orbit and the time-of-flight theories do not fully account for the effect of the cyclone length. As shown in Ref. [20] in the experiments the cut size decreases with an increase of the cyclone length until a certain length, after which the cut size of the long cyclone becomes larger than that of shorter cyclones (see Figure 2.3 (b)). This contradicts the predictions of theoretical models and the CFD simulations. The cyclone performance, all other design aspects being equal, once exceeding its optimal length, becomes inferior. The separation efficiency undergoes a dramatic reduction for the longest cyclone length. The extra length becomes ineffective and even harmful.

At the longest length a dust ring was consistently observed on the conical wall of the dust hopper, as indicated by the arrow in Figure 2.3 (a), after operation for half an hour. Under the dust ring the transport of particles was obviously poor since the funnel underneath the ring was partly filled with powder.

In Refs. [6, 21] a sharp increase in the amount of wall deposits below the ring was observed, as shown in Figure 2.4 (a), indicating the inefficient transportation towards the dust outlet. A rotating 'eye of the hurricane' on the inner wall has been observed, as shown in Figure 2.4 (b), in a dust fed cyclone using a strobe light [1, 22].

The pressure measurement on the swirl tube wall at various heights shows periodical troughs at a specific height, as shown in Figure 2.5 (a) [22], which indicates that the end of the low-pressure vortex-core attaches to, and rotates on, the wall at this height. The rotation frequency increases as the flow rate is increased. Figure 2.5 (b) show the pressure profile along the entire cyclone body. Within the conical section the static pressure decreases noticeably, and in the hopper section the wall pressure is observed to undergo a very sudden and significant decrease, where periodical troughs, indicating the precession of the vortex core, are detected. As the solid loading is increased, or when the flow rate is decreased, the 'end of the vortex' was found to occur at higher positions. When the 'end of the vortex' is present, a longer vortex length (i.e. the length from the bottom of vortex finder to EOV) improves the separation efficiency and decreases the

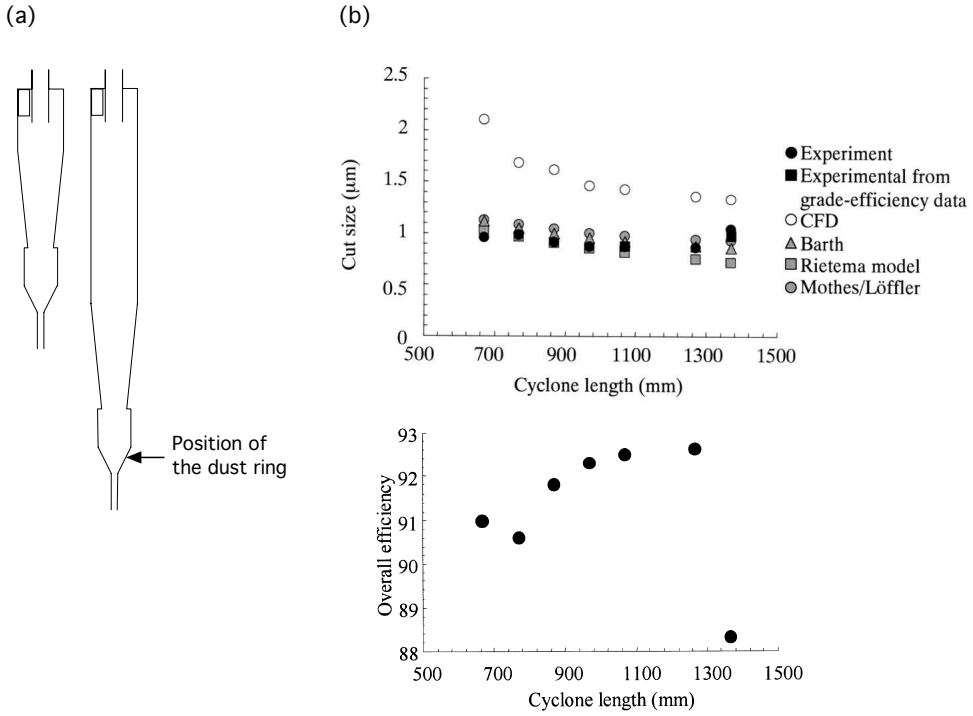

Figure 2.3: (a) The range of cyclone lengths tested in Ref. [20]. The cyclone is lengthened by extending the cylindrical section. (b) Top: Cut size vs. cyclone length. The experimental cut size decreases with an increase of the cyclone length until a certain length. Bottom: Overall efficiency vs. cyclone length. The separation efficiency undergoes a dramatic reduction for the longest cyclone length. Reprinted from Ref. [20] with permission from John Wiley and Sons.

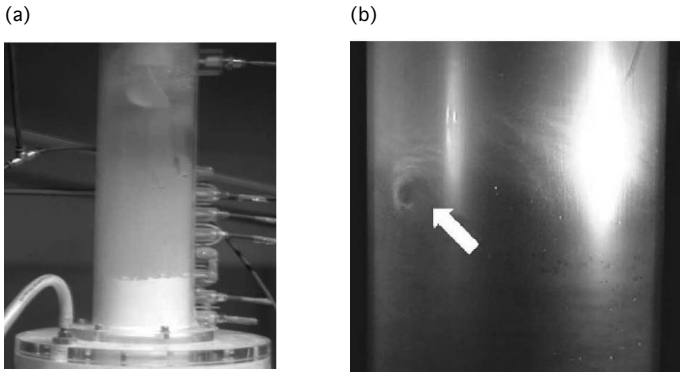

Figure 2.4: (a) A sharp increase in the amount of wall deposits below the ring formed by the 'end of the vortex'. Reprinted with permission from Ref. [21]. Copyright 2006 American Chemical Society. (b) A stroboscopic image of the 'eye' of the vortex core attaching and precessing along the cyclone wall. Reproduced from Ref. [1] with permission from Springer Science and Business Media.

pressure drop.

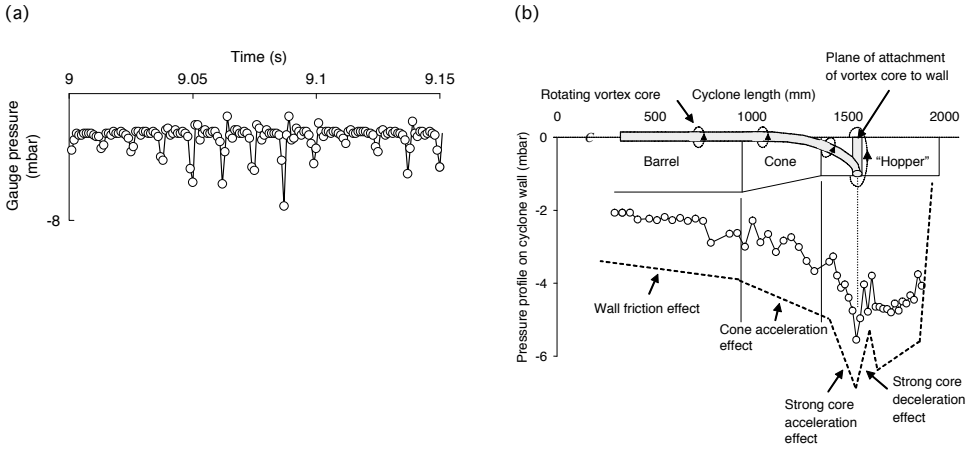

Figure 2.5: (a) Pressure measurement on the swirl tube wall shows periodical troughs at a specific height. Reprinted from Ref. [22], Copyright 2005, with permission from Elsevier. (b) Wall pressure profile showing sharp decrease in pressure in the plane where the vortex attaches to the hopper wall. Reprinted from Ref. [22], Copyright 2005, with permission from Elsevier.

In Ref. [21] the effect of rectifying vanes (pressure recovery vanes) on the flow pattern and separation efficiency of the gas swirl tube was studied. It has been found that, in addition to decreasing the separation efficiency, the pressure recovery vanes seem to destabilize the vortex, probably because it is decreasing the swirl velocity in the separation space. The end of the vortex could be observed in the swirl tube under all experimental conditions tested, except at the highest flow rate without the rectifier and without dust injection, where the core could centralize and the vortex could extend all of the way down to the bottom of the hopper. While the rectifier was installed, a centralized vortex core could not be achieved with any gas flow rate and the wall deposits in the tube under the position of the vortex end can also be seen.

The 'end of the vortex' also appears, visualized by the dust rings, in parallel swirl tubes with a common dust collecting plenum [23]. Unlike the rings observed in the single swirl tube which stays at an axial position, the dust rings observed in parallel swirl tubes were seen to change position and sometimes disappear from sight (while the vortex core is actually attaching to the lip). The dancing rings may be related to the phenomenon of 'cross-talk'. The pressures in the bottom of the tubes with and without the EOV present are likely different, which causes flow from one tube to another. The upflow in a tube further destabilizes the vortex and causes the attaching position of the vortex end to move upward. The pressure measurements on various axial positions of swirl tube walls exhibit periodic troughs, indicating the vortex end's rotating on the wall, which is consistent with the results obtained in single swirl tube as shown in Ref. [22]. The magnitude of the pressure troughs, however, fluctuates considerably, which reflects the dancing ring phenomenon and the related cross-talk.

The vortex core's bending to and rotating on the swirl tube wall has been visualised by illuminating neutral-density helium-bubble tracers, as shown in Figure 2.6 (a) [24]. The

fast precession of the vortex core appears as a conical shape to the naked eyes and on images with long exposure time compared to the period of the rotation.

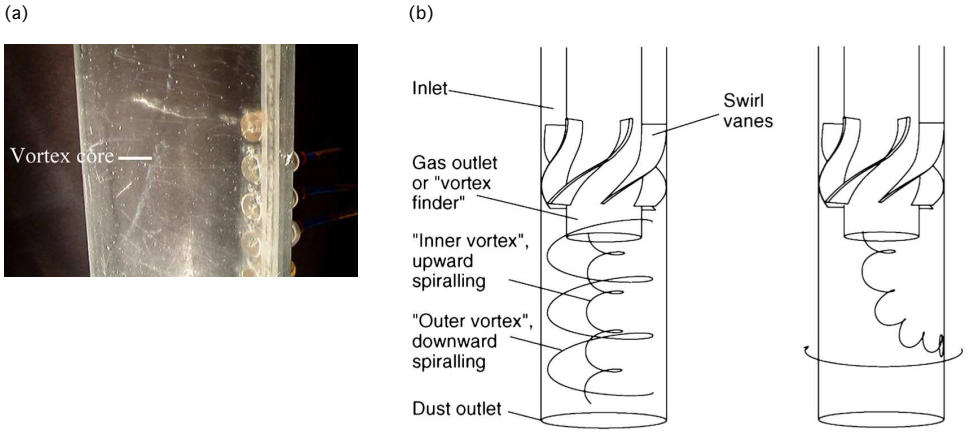

Figure 2.6: (a) The vortex core deviates from the axis of the swirl tube, bends to the wall, and precesses around the wall at the point of the 'end of the vortex'. Reprinted from Ref. [24], Copyright 2010, with permission from Elsevier. (b) Left: Centralized vortex core. Right: Illustration of vortex core bending to and precessing on the wall as observed in (a). Reprinted from Ref. [24], Copyright 2010, with permission from Elsevier.

2.3 Fluid velocities near the wall in the vortex end's attaching area

As mentioned in Section 2.2, while a cyclone was fed corundum solids, an erosion band appeared in the lower cone [17]. Does the erosion band result from the 'end of the vortex'? The sketch in Figure 2.7 illustrates the gas velocity of the 'eye of the hurricane' on the wall. As the end of the vortex is precessing around the inner wall at some precessional frequency f and precessional velocity $\mathbf{v}_p$, the particles in this area will be affected by the tangential velocity at CS $\mathbf{v}_{CS}$ and the vortex core's precessional velocity $\mathbf{v}_p$. The velocity in positions A and B is the superimposed velocity $\mathbf{v}_p + \mathbf{v}_{CS}$.

Examples from Ref. [1] show that the highest velocity around the vortex 'eye' can greatly exceed the inlet velocity. If the solids are abrasive, this intense velocity can lead to severe localized erosion. The erosion band found in the lower cone of the cyclone fed with corundum solids in Ref. [17] effectively depict the path of the precessing vortex end.

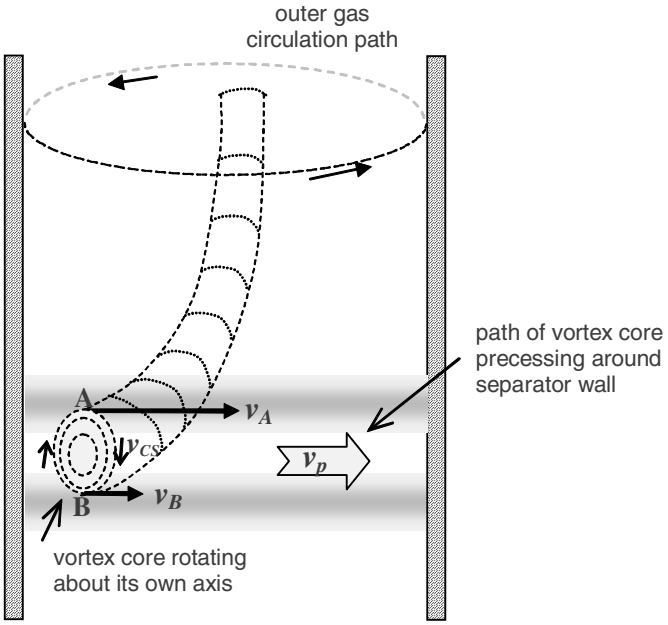

Figure 2.7: Vortex end attaches to and precesses around the inner wall. Reproduced from Ref. [1] with permission from Springer Science and Business Media.

2.4 Consequences of the 'end of the vortex'

2.4.1 Effect of EOV on the separation performance

As the 'end of the vortex' with high spin velocities is rotating on the wall, some of the dust, while being centrifuged and spiraling down the wall, may be re-entrained by the precessing vortex end. The highly unstable flow field at this axial position (the entire plane) significantly disturbs the particles' ordinary downward swirling. This explains the experimentally observed optimal length of cyclones as shown in Figure 2.3 (b) [20], where the extra length not only becomes ineffective but even causes increase in the cut size and significant diminution in the overall efficiency due to appearance of EOV in the longer cyclones.

Moreover, Abrahamsen and Allen [25] claimed that the position of the vortex end is related to the steepness of the grade-efficiency curve near the cut size, i.e. the 'sharpness' of the cut. Considerable mixing of the particles in both dedusting and demisting cyclones was observed at the plane where the precessing vortex 'tail' attaches to the lower walls [1], which explains the change in sharpness.

The occurrence of the 'end of the vortex' in the separation space does not simply limit the effective length but is furthermore detrimental to the efficiency and sharpness. Therefore, the EOV should be carefully avoided as the cyclones are being designed and their operation parameters are being chosen.

2.4.2 Effect of EOV on the integrity of separated products

Since the orderly helical flow of separated products down the walls of the cyclone can be abruptly disturbed as it enters (and becomes momentarily entrapped in) the precessing EOV, the separated products can suffer deterioration due to erosion against the wall driven by the high tangential velocities of the EOV eye. Tacky or sticky particles may also tend to accumulate on the wall below the position of the EOV [1]. This can be ruinous for separating delicate matters, for example separating cell or yeast from liquid using hydrocyclones as used in, e.g., Refs. [26–28].

2.4.3 Effect of EOV on the particle trajectories and the flow field beneath

As observed in Refs. [6, 20], while the vortex ends in the separation space, the cyclones are prone to fouling and clogging, since the transport of particulates along the wall toward the underflow outlet is less efficient below the vortex end.

The particles that have reached the wall, as transported towards the underflow outlet, can be disturbed by the vortex core precession. Pisarev and Hoffmann [16] conducted computational fluid dynamics (CFD) simulations to study the effect of the EOV on the particle motion in gas cyclones. The EOV phenomenon appears in the flow field at certain flowrates. Tracks of particles were obtained by solving the particle equation of motion as the particles were tracked individually in the flow field. While being able to reach the EOV region, the particle is trapped in the 'end' of the vortex core, which is attaching to and precessing on the cyclone wall. The trapped particle moves, depending on the sizes, either irregularly or in small circular patterns around the precessing core on the wall. The prolonged residence time would cause clogging of the cyclone. The intense circular motion on the wall in the EOV region would lead to severer wear.

It appears that, if sufficient height is available, the vortex end's rotating on the wall induces a secondary vortex of weaker intensity below the main or primary vortex, as shown in Figure 2.8. It has not been thoroughly investigated how the particles would be affected by EOV and how effective the secondary vortex is in collecting solids. The work performed in this thesis aims to investigate this inadequately understood area.

2.5 Factors influencing the EOV

The spinning vortex core in cyclones and swirl tubes is similar to a spinning top: The higher the angular momentum, the harder to change its direction. As the angular momentum is reduced, its direction can be altered with less effort. For the spinning top, the precession starts because the vertical angular momentum is affected by the torque arising from the weight times the distance from the center of mass to the tip. In the cyclones and swirl tubes the vortex can be decentralized due to the perturbation in the flow field, e.g. fluctuated upflow in the parallel swirl tubes [23], and factors that consume

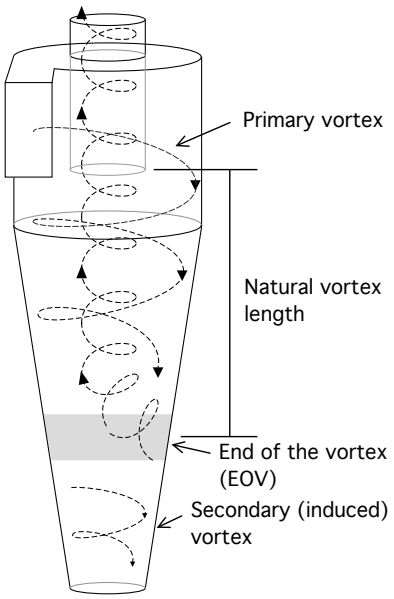

Figure 2.8: When the 'end of the vortex' occurs, the vortex end attaches to the side wall and turns around. This is known as 'vortex precession', since the orientation of the vortex axis is changing. Three rotations appear: one around the core of the vortex and another is the vortex core's rotating on the wall, which then induces a much weaker secondary vortex below the 'end of the vortex'.

vortex's energy and reduce the angular momentum. The force intending to incline the vortex end generates an angular momentum, which causes the angular momentum of the inclined vortex end to swing, leading to vortex end's precessing. Therefore, factors that consume vortex's energy, like friction and drag, will reduce the angular momentum of the vortex and facilitate the formation of the EOV.

As reported in Ref. [17] mentioned in Section 2.2, when a cyclone was fed fly ash particles, no erosion ring occurred in the lower cone. When the cyclone was fed corundum particles, however, an erosion band appeared. The reason, as noted in Ref. [1], could be that, relative to the ash particles, the corundum particles used were much more dense and much larger than the ash particles. The larger corundum particles can increase the effective wall roughness due to their size. Also, the corundum particles erode and roughen the walls to a much greater extent compared to the ash particles. The particle properties, together with the wall roughness that the particles have created, can weaken the angular momentum of the vortex. As losing angular momentum, the vortex tail becomes unstable, decentralised and inclined, attaching to and processing around the lower cone wall, which, as discussed in Section 2.3, produces the observed peak in the erosion profile.

Hoffmann and Stein [1] have pointed out their observation on the factors influencing the vortex stability, EOV, and the vortex length in gas cyclones and swirl tubes. Below, the observations in Ref. [1] and the other above-mentioned references are summarized.

- Operation variables
  - Intermediate solids loadings (tens of grams of dust per cubic meter of gas) can also destabilize the vortex compared to very light loadings (a few grams of dust per cubic meter of gas).Very high loadings would eventually break down the high velocity inner core, and hence no EOV is generated.
  - Above a certain inlet velocity and under similar conditions, increasing inlet velocity can increase the vortex length (the dust ring moves downward).
  - The rotation frequency of the vortex end increases as the flow rate is increased.
  - Enabling the underflow (a bleed flow drawn from the dust hopper) can increase the vortex length.
- Operation conditions
  - Increasing wall roughness (rough liner, eroded walls, wall deposits or higher solids loading) destabilizes the vortex, giving rise to the vortex core bending toward the wall and decreasing the vortex length.
  - Gas backflow from the dust hopper (due to leakage or cross-talk, for instance) can shorten the vortex length.
- Geometry and construction
  - A too small vortex finder diameter can destabilize the vortex, affecting the vortex length.
  - A vortex stabilizing plate or cone can affect the vortex length.
  - The rectifying vanes (pressure recovery vanes) can destabilize the vortex probably because of decreasing the swirl velocity in the separation space.
  - Decreasing the lower cone diameter can change the effective length of the vortex.
  - The parallel swirl tubes with a common dust collecting plenum can destabilize the vortex duo to the 'cross-talk'.

All these factors make it very complicated to construct a universal expression for the natural vortex length. There is much to be understood regarding the unstable flow field and the 'end of the vortex', for predicting position of EOV based on the dimensional and operational variables, controlling the erratic behavior of EOV, and determining how all this affects cyclone design and performance.

Chapter 3

Positron emission particle tracking (PEPT)

3.1 Background

Positron emission tomography (PET), conceptualised in the late 1950s, is today a powerful medical imaging technique used to generate 3-D images of tracer (positron-emitting radionuclide) concentration within the body [29]. The radioisotopes, such as gallium-68 (half-life 68 min) and fluorine-18 (half-life 110 min), emit a positron while undergoing positron decay. The positron travels a few millimeters in solids or liquids before annihilating with an electron. The annihilation produces two gamma photons of 511 keV that travel in opposite directions. If the two gamma photons from an annihilation were detected within a short timing window (i.e. coincidence window), the annihilation event is judged to occur on the line (line of response; LOR) connecting the two detectors. By surrounding the subject under investigation with a large amount of gamma photon detectors and applying tomographic reconstruction algorithms, the 3-D concentration distribution of the radioactive tracers can be revealed. A common medical use of PET is to map the concentrations of a glucose analog, ^{18}F-FDG, which is the glucose molecule with the positron-emitting isotope fluorine-18 replacing the normal hydroxyl group. The PET images show the regional glucose uptake, which could indicate tissue metabolic activity.

The penetration capability of the gamma photons and the ever improved spatial resolution make the PET technique a valuable tool for studying non-medical processes non-invasively. The very first applications include studying the distribution of lubricant in operating engines and test rigs [30, 31]. The positron camera and isotope labelling was used to map the brine displacement in porous geological strata, e.g. oil-reservoir sandstone [32], as well as to investigate the efficiency of extraction of crude oil or kerosene (a good analogue for North Sea crude oil) by slowly flooding with brine, where either the aqueous (brine) phase or the kerosene (oil) phase was labelled with the positron-emitting isotope [32, 33]. While in some of these experiments the specimen were enclosed in a steel tube to simulate a pressure vessel, the PET technique was capable of acquiring data which are unobtainable by using other techniques such as X-ray computerised tomography

(CT). Other non-medical applications of the PET technique include the characterisation of fluid transport in fractured rock [34], imaging extrusion of radio-labelled dough into small moulds, which demonstrates how easily a blockage can form [32], and imaging the labelled powder in a pharmaceutical blender [35]. Dechsiri et al. [36] used PET to study directly the dispersion of pulses of particles in fluidized beds. Cross-sectional bitmaps, 3-D plots, and contour plots of the tracer concentration have been obtained with 1-sec temporal resolution. In order to collect sufficient amount of data, acquisition in the above mentioned applications requires a few seconds to tens of minutes, which is very likely too slow for mapping dynamic processes with time scales below a second. However, if the subject of interest is a particle, its location can be identified using far less data obtained within a shorter time interval, rendering visualisation of the dynamic process possible. The technique named 'positron emission particle tracking (PEPT)' is the focus of this thesis: PEPT has been explored, developed and applied to visualise the flow of both phases in a hydrocyclone, which unveils the mysterious EOV phenomenon and enables more precise and direct investigation into the flow field.

3.2 Introduction to PEPT

Because the penetration of gamma photons can only be stopped by thick layers of concrete, lead, steel and other comparable materials, PEPT is useful for probing processes confined in opaque, complicated structures where the operational matter interacts with the moving parts of the equipment constantly, since in those instances particle tracking by optical techniques, e.g. high-speed cameras (see e.g. [37–39]) or silicon strip detectors [40, 41] is nearly unfeasible.

The application of PET hardware for PEPT use was initiated in the late 1980s. One of the very first particle tracking using PET was to track a 3 mm glass bead containing ^{22}Na in a domestic mixer [42]. The 3-D particles trajectories in mixing process in a powder, a biscuit crumble and a liquid slurry have been obtained. Since then PEPT has been applied to investigate the flow in a variety of equipment and processes, including rotating drums [43–45], various type of mixers [46–51], fluidized beds for various purposes [52–54], extrusion systems [55], stirred grinding mills [56], stirred vessels [57, 58], the pharmaceutical Wurster coating system [59], rolling foodstuff cans [60], multiphase stirred tank reactors [61], casting [62–64], pipes [65, 66], valves [67] and twin screw granulators [68].

3.3 The camera

Several research groups use medical PET systems or reconfigure medically decommissioned PET cameras into modules for non-medical applications [35, 69, 70]. The great advantages of dismantling the medical ring-type cameras into modular ones, and possibly combining modules from two or more cameras, is that it can adapt to the size of the target equipment and can be transported for on-site measurement, for

example the PEPT study on a full-scale fluidized bed at a BP's site [71]. However, reliability problems with the modular cameras have to be taken into consideration [35].

The PEPT facility for this work is co-operated by the University of Bergen and Haukeland University Hospital, making use of the PET camera—the Siemens Biograph TruePoint 3-ring PET/CT system [72, 73]. The cylindrical PET camera is composed of 3 block rings with a gap of a crystal width (see below) between adjacent blocks, and each ring comprises 48 blocks with a gap of one crystal width between adjacent blocks, as shown in Ref. [74]. Each block comprises 13 × 13 Lutetium Oxyorthosilicate (LSO) scintillator crystals, which are then coupled to four PMTs (photomultiplier tubes). Dimensions of each LSO crystal is 4 mm square and 20 mm thick, which gives the PET camera 24336 real crystals, inner diameter of 854.8 mm and axial coverage of 162 mm. The use of advanced Pico 3D electronics enables the system to operate with a coincidence window of only 4.5 ns, reducing the number of random coincidences as compared to older models. The energy window is 425–650 keV. For more details on the detector layout and parameters, see Ref. [73]. In the PEPT experiments the hydrocyclone is inclosed in the cylindrical camera cavity, as illustrated in Figure 3.1.

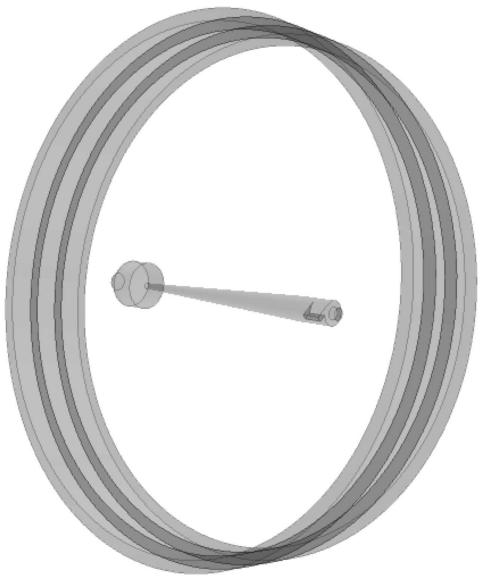

Figure 3.1: Schematic showing the arrangement of the hydrocyclone in the cylindrical 3-ring PET camera with inner diameter of 854.8 mm and axial coverage of 162 mm.

Theoretically two annihilation events producing two LORs from a infinitely small, radioactive particle can already define the location at the cross point. In PEPT one or more particles are labelled with positron emitting isotopes. The centroid of all the radioactive substance distributed on a particle will be defined as the particle position. On a 2-D projection, the LORs do not all cross at a single point not only due to the finite size of the particle but also due to the interaction of radiation with matter as well as the characteristics of the detection system [29], accounts of which are given below.

The primary interaction between matter and the photon at energies around 0.5 MeV is

Compton interaction, where part of the energy of the incoming photon is transferred to a loosely bound orbital electron and cause the electron to be ejected from the atom. The energy loss by the photon comprises the small binding energy and the kinetic energy imparted to the ejected electron, also called the Compton recoil electron. The photon is then deflected through an angle proportional to the amount of energy lost. The result of Compton interaction is that the photon changes direction (i.e., is 'scattered') and loses energy. In addition, the atom where the interaction has occurred is ionized. If one or both of the detected gamma photons have undergone Compton interaction, the LOR would be wrongly ascribed, as shown in Event 3 in Figure 3.2. The energy window of the PET camera (425–650 keV for Biograph TruePoint) therefore allows differentiation (to some extent) between true and scattered coincidences.

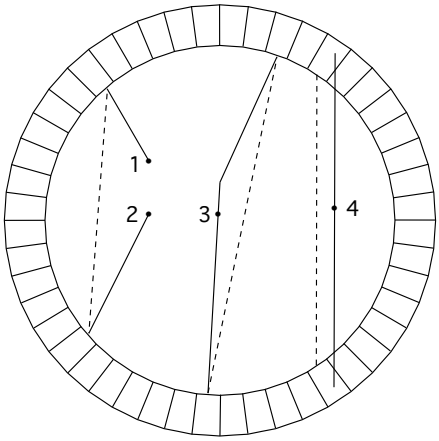

Figure 3.2: Events 1 and 2: Two unrelated events with only one of each photon pair being detected within the coincidence window, which leads to an incorrectly assigned LOR (dashed line). Event 3: One of the gamma photons is scattered leading to falsely assigned LOR. Event 4: The deviating LOR due to the depth-of-interaction of the photons within the detectors. Reprinted from Ref. [74] with permission from Springer Science and Business Media.

Apart from Compton interaction, miss-detection of one gamma photon of an event, or more than two gamma photons hitting detectors within a coincidence window can also result in wrong LORs, as illustrated by Events 1 and 2 in Figure 3.2, termed random coincidence. Miss-detection can be due to the limited detector coverage of the camera (e.g. the Biograph TruePoint camera is a cylinder surrounding the field of view) and the maximum data processing rate of the system, which gives rise to a dead time during which the detector remains insensitive while the system is processing a detection [75]. The number of random coincidences can be reduced by reduction of the dead-time and shortening the timing window. The rate of random coincidences is approximately proportional to the square of the count rate originated from the radioactivity within the subject. Therefore, at high count rates the reduction in random coincidence becomes critical. Biograph TruePoint PET camera employing LSO crystals and advanced electronics improves system dead time and offers a fast coincidence timing window of 4.5 ns for efficient rejection of random events while maintaining high count rate.

Deviation of LORs can be also due to the 'depth of interaction' in the crystals: After a photon enters a detector, it travels a short distance, namely the mean attenuation length of the crystal, before depositing all its energy and being identified. If the photon enters the detector at oblique angle, it may travel to the adjacent detector as the Event 4 in Figure 3.2 shows. This error will become prominent as the photon emitting source moves far away from the center of the field of view (FOV). The higher standard deviation in the positions of a stationary particle when approaching the axial end of the cylinder camera as presented in **Paper I** mainly results from one of the photons from decay events falling outside of the detection cylinder.

As the photon pairs are detected, the identities of the detector pairs are recorded successively in list-mode format. The camera inserts a timing mark into the data stream every millisecond. As the PET camera is used for PEPT, the data processing algorithms for tomographic reconstruction are not applicable. In the Multiphase Group at the University of Bergen we have developed several data processing algorithms, each optimized for different tracking conditions and constantly refines the algorithms for better resolutions. Section 3.5 below will give a detailed account of the algorithms.

3.4 Tracer and labelling

In PEPT one or more particles representing the components of the process under investigation will be followed to reveal the components' traces. The particles are labelled with positron emission isotopes. Two labelling methods—direct activation and ion-exchange—have been reported by Fan et al. [76]. The half-life of ^{18}F, 109 min, is suitable for many laboratory experiments including the cyclone separation process studied in this thesis. Therefore ^{18}F is the most used isotope for PEPT experiments.

In direct activation, a few of the oxygen atoms in the particles are converted into ^{18}F radioisotope by the particle being directly bombarded by a 33 MeV ^{3}He beam. Some short-lived radioisotopes are also produced from other elements of the particles at the same time. Since the radioactivity is proportional to the square of the particle diameter, and considering the experimental time scale and the half-life of ^{18}F, the 'direct activation' is more suitable for labeling a larger particle with a size range from 1 to 10 mm, and also the material must be able to resist a high temperature.

The ion-exchange technique makes use of the different affinity of anions to 'strong-base anion exchange resins':

$SO_4^{2-} > HSO_4^- > I^- > NO_3^- > Br^- > Cl^- > HCO_3^- > HSiO_3^- > F^- > OH^-$.

Firstly the 33 MeV ^{3}He beam from the cyclotron bombards purified water, which facilitates the reaction ^{16}O(^{3}He, n)^{18}Ne $\rightarrow$ ^{18}F. By immersing 'strong-base anion exchange resins with OH group' into the ^{18}F-carrying water and properly agitating the water, the ^{18}F replaces the OH because of its higher affinity to the resin molecule. The radioactivity contained in a single resin bead is controlled by the ion-exchange properties of the resin material, the radioactive anion concentration in the water, and the immersion

time. Because the life-time of the ^{18}F also has an effect, the radioactivity of a resin bead can be maximized between 10-20 min of immersion [76]. The ion-exchange technique can be used to label smaller resin particles with a size below 1000 μm. Note that since many other anions have higher affinity than fluorine, the water has to be highly purified to ensure fluorine's bonding to the resins.

In this thesis the ion-exchange technique is adopted and radioactive water is produced using the cyclotron in Haukeland University Hospital. Porous-structured strong-based anion ion exchange resin beads, Amberlyst A26 OH form (Acros Organics), with a harmonic mean size of 560–700 μm, were immersed into the radioactive water and the mixture was shaken for about 10 min. The resulting radioactivity on each bead can reach 450–1440 μCi, depending on the ^{18}F concentration in the water and the size of the bead. Dissociation and dispersion of ^{18}F in water were checked by the uncertainty in positioning a stationary tracer as function of time, as shown in **Paper I** and **Paper V**. The terminal velocity of the Amberlyst A26 resin beads in water was measured, showing that the behavior of the beads corresponds to that of 90–115 μm particles with density of 2650 kg/m^3 (the density of sand).

The density of the tracer beads can be altered by coating, e.g. with wax, in order to represent particles with different properties. If the particle has low inertia and the same density as the fluid (so that the particle has neutral density), the particle would adjust to changes in flow velocity or direction swiftly and follow the fluid motion faithfully. Therefore, the behavior of the fluid can be appraised by following a neutral-density tracer. Fangary et al. [49] tracked a resin particle of diameter 600 μm and density 1024 kg/m^3 in a stirred vessel containing non-newtonian liquid using PEPT. The particle was reckoned nearly neutrally buoyant because of the low particle-fluid density ratio (1.024) and low terminal settling velocity (in the order of 10^{-14} m/s) in the studied liquid. Moreover, the Stokes number is in the order of 10^{-4} indicating that tracer particle would likely follow the streamlines rather than moving relative to the fluid.

In this work we have made the Amberlyst A26 resin beads neutrally buoyant either by coating the beads with wax or by modifying the density of surrounding liquid (see **Paper VI**). Following the neutrally buoyant tracers by PEPT has revealed the pathlines of the fluid element and the fluid velocity field in a hydrocyclone.

3.5 Data processing

As mentioned in Section 3.3, many effects can cause wrong or deviated LORs. Therefore, special strategies are adopted to eliminate or mitigate the influence of those deficient LORs. The algorithm for PEPT developed in University of Birmingham uses an iterative approach, which starts off by finding the point that minimises the sum of distances, so it is claimed, to all the LORs, and then discards the LORs further than a certain distance from the point and recalculates the point [77]. The action of finding centroid point and discarding LORs is repeated until a certain fraction of the original LORs is left. This optimum fraction varies depending on the geometry and the amount of scattering material that the gamma photons have to pass. In this method executed in University

of Birmingham it is possible that only 5% of the detected events is taken into account in the final calculation [78].

In the Multiphase Group at the University of Bergen we have refined the algorithm developed by Hoffmann et al. [79] as well as developed various data processing strategies to preserve the genuine events and find the center of the tracer particle.

'Method 1' is an iterative approach that starts off by averaging all the cutpoints, i.e. cross points, of LORs in the whole FOV in 2-D, and then discards the points farther than a certain distance from the just-obtained average and recalculates the average. The process of averaging and discarding farther cutpoints is repeated until the spatial window is shrunk to an optimum size which is verified by the lowest standard deviation of positions per millisecond of a stationary particle, as detailed in **Paper III**. The coordinate on the third axis is obtained by averaging the coordinates of the left cutpoints.

'Method 2' starts off by finding the meaningful tracer position using 'Method 1'. Once the tracer is found entering the FOV with satisfactory number of cutpoints in the final window, in the subsequent time step only the cutpoints around the latest found position will be averaged. The process of averaging and discarding farther cutpoints is repeated, as similar to 'Method 1' but starting with a much smaller spatial window, until the spatial window is shrunk to an optimum dimension. 'Method 2' is faster than 'Method 1'. While the positions are forming a streamline or a pathline, they are sure to be continuous in space along the time. Therefore 'Method 2' can eliminate the false cutpoints (resulted from false LORs) in the very beginning of the process in every time step, and there is nearly no chance to find wrong positions even huge fraction of corrupt LORs present (see **Paper VI**).

'Method 3' uses the point that minimises the sum of the *squares*[1] of the distances to the LORs as a reference point. The cutpoints within a certain spatial window around this reference point, rather than the cutpoints within the whole FOV, in a 2-D projection are then averaged. The process of averaging and discarding farther cutpoints is repeated, similar to 'Method 1', until the window is shrunk to an optimum size. 'Method 3' is faster than 'Method 1' since promptly obtaining the initial guess replaces several iteration of averaging and shrinking average window. 'Method 3' is same accurate in most cases. However, the method of minimising the sum of squared distances to the optimum fraction of LORs sometimes gives wrong positions when a huge fraction of corrupt LORs is present.

'Method 4' firstly finds all the cutpoints and fits the counts of the cutpoints in each coordinate with one or multiple (while multiple tracers being presenting) Gaussian or Lorentzian peak function, as demonstrated in Figure 3.3. The algorithm then finds subsequent position around previous position, as similar to Method 3, or fits the peak(s) every time step. 'Method 4' has been verified by tracking two resin beads attaching to a rotation plate, which inclined with around 45 degree to the ground. In the experiments included in this thesis we injected one particle at a time, so 'Method 4' has not been applied to track particles in a hydrocyclone. However, multi-particle tracking can provide

[1]We found that there is no analytical solution to the problem of minimizing the sum of the distances themselves, only the sum of the squares of the distances.

simultaneously unique information of rotational and translational movement of an object in the process, e.g. heat transfer and mixing processes. The multiple-PEPT can also be applied to investigate devision and coalition, e.g. cell devision, as a potential application.

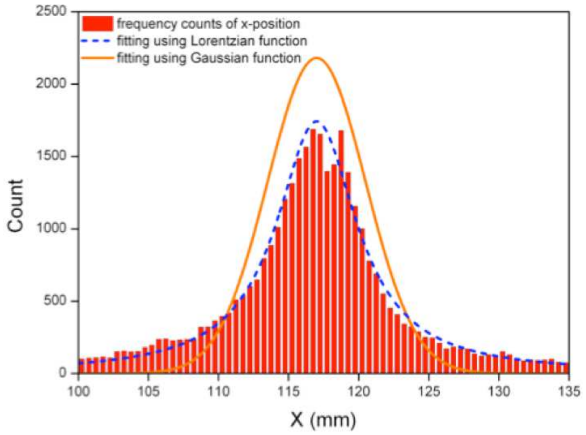

Figure 3.3: The distribution of the cutpoint count can be fitted by Gaussian or Lorentzian function.

As for tracking multiple particles, 'Method 4' works best if the tracers take on similar levels of radioactivity. The method of multiple-PEPT reported in Ref. [80] uses a different algorithm, which is suitable for tracers carrying different levels of radioactivity: It firstly locates the tracer with the strongest radioactivity by using single-PEPT method as described in Ref. [77], which in principle finds the point that minimises the sum of distances to non-corrupt LORs. The LORs used for the location of the tracer with strongest radioactivity are then removed from the data set. The locations of the rest of the tracers are obtained in the same way (also refer to [81, 82]).

As the detector pair information are recorded continuously and the timing mark is inserted into the data stream every millisecond, it is possible to split the data in a millisecond to improve the temporal resolution from 1 ms to 0.5 ms and 0.25 ms, as verified in **Paper III**. The trajectories obtained by positioning the tracer once per 0.5 ms are shown in **Paper III** and **Paper VI**.

Chapter 4

Summary of papers included in the thesis and some unpublished results

4.1 Published papers

Paper I: *Particle flow in a hydrocyclone investigated by positron emission particle tracking*

This paper reported, for the first time, particle tracks in a hydrocyclone obtained by PEPT, showing many interesting features which could not been seen by other techniques. Firstly the developed particle labelling method and particle positioning algorithm were verified. The positioning precision, i.e. the standard deviations of positions, is examined as a function of

i) tracer particle residence time in the water,

ii) the number of 'lines of response' in the final averaging window and

iii) the position in the field of view.

The algorithm has undergone continuously development to improve resolutions, to tackle different noise intensity and types, and to track multiple particles. Some of the development consideration and verification are detailed in **Paper III** and **Paper VI**.

Connecting the consecutive positions obtained every 1 ms in a hydrocyclone forms the trajectory, as shown in Figure 4.1, where the particle swirls towards the underflow outlet after entering the hydrocyclone but experiences abnormal excursions in certain sections as it approaches the underflow outlet. The anomalous excursions include i) The particle reduces its rotation radius and enters the inner vortex of axial upflow, flowing toward the vortex finder for a while, whereafter it is centrifuged outward to the downwardly directed outer vortex again (see Figure 4.2), ii) The particle is trapped by strongly turbulent flow at a given axial position low in the cyclone, moving irregularly for a 'long' period of time. After having negotiated this axial position, the particle restores its swirling motion but

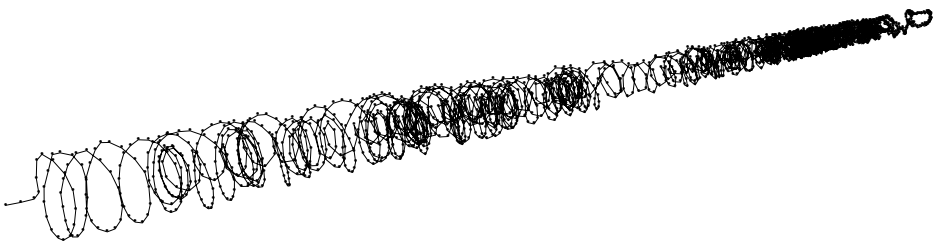

Figure 4.1: An example of a particle trajectory in a hydrocyclone, each point represents a particle position obtained per millisecond. The particle's moving from inlet to underflow outlet takes less than 3 seconds.

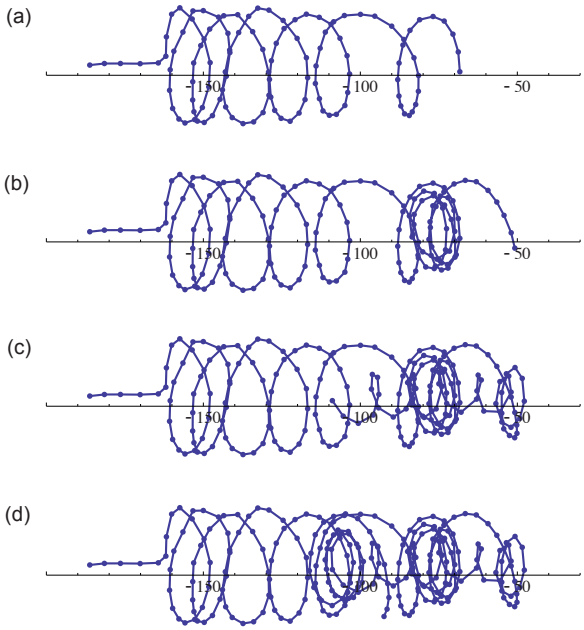

Figure 4.2: The trajectory of a particle from (a) 108 ms to (d) 247 ms of Figure 4.1. In (b) the rotation radius suddenly decreases and the particle, stopping its axial motion toward the particle outlet, rotates for several turns at nearly the same axial position. Subsequently, the particle regains the original radius and resumes its downward motion. However, the radius decreases again in (c), and this time it is pulled into the inner vortex and swirls upward a distance until once again being centrifuged to the outer vortex in (d).

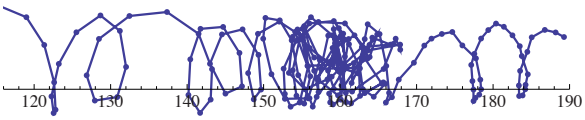

Figure 4.3: The particle is trapped by the unsteady sinuous flow low in the hydrocyclone. Below the 'trapping' position the successive positions are much closer spaced, showing that the particle swirls at a reduced velocity.

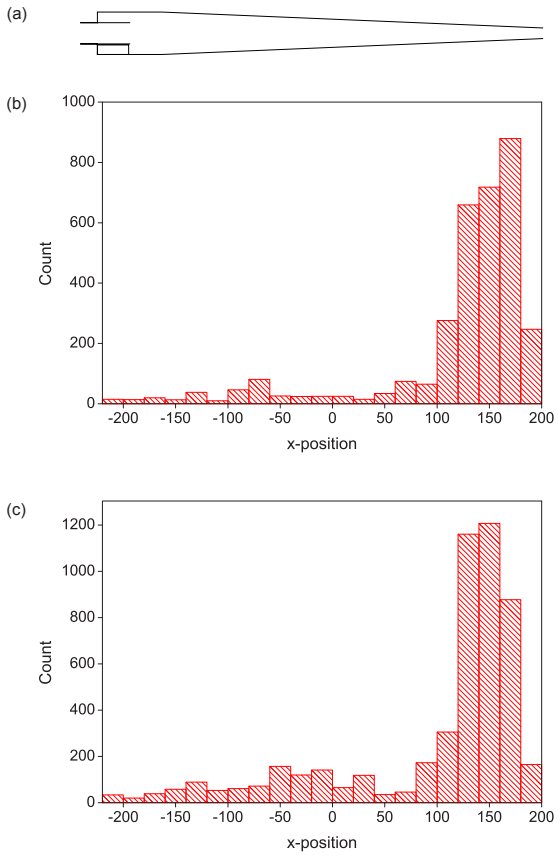

Figure 4.4: The frequency of particle appearance in different sections of the hydrocyclone.

moves much slower as shown in Figure 4.3, where the successive positions are much closer spaced below the position at which it was trapped.

Plotting the frequency of particle appearance in various axial sections of the hydrocyclone (see Figure 4.4) shows that the particles spends a considerable time close to the underflow outlet due to the above-mentioned unsteady sinuous flows and the recurring axial flow reversals.

The much slower swirl after the 'trapping' position as shown in Figure 4.3 indicates the presence of the 'end of vortex' phenomenon—the core of the vortex bending to the wall and rotating around the wall at this position. The rotation of the vortex cored induces a secondary, much weaker, vortex underneath, causing the particle to spiral at a much reduced velocity below the 'end of vortex' position. The possible reasons for the presence of the 'end of vortex' phenomenon were discussed in this paper.

Paper II: *Numerical study of the 'end of the vortex' phenomenon in a hydrocyclone separator*

This paper reported, for the first time, the computational fluid dynamics (CFD) simulations of the 'end of vortex' phenomenon in a hydrocyclone. CFD simulations have been performed using the large eddy simulation (LES) turbulence model to simulate the flow pattern in the hydrocyclone geometry as used in the PEPT experiments in **Paper I**. The turbulence model, algorithm, mesh setup, parameters, initial conditions, and the mesh convergence tests are described.

The simulated cross-sectional static pressure distributions show that the vortex core is already attached to the wall as it forms and subsequently the vortex end descended until gradually approaching and remaining at steady level low in the cyclone body (see Figure 4.5). The rotation of the vortex end around the inner wall was visualized by monitoring the pressure profile on the wall, as shown in Figure 4.6 where the position of the core could be seen as an 'eye' of low pressure, and the rotation frequency was obtained by monitoring the position of the eye during a longer simulation.

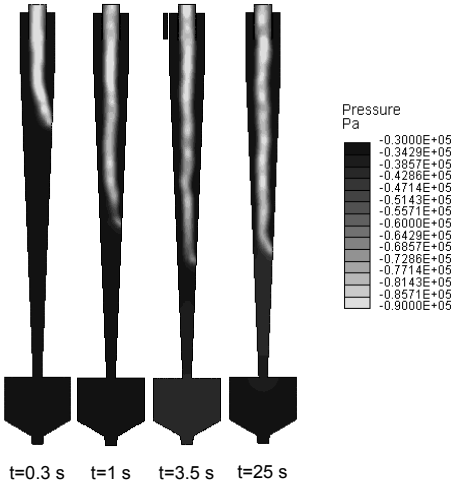

Figure 4.5: Cross-sectional contour plots of static pressure simulated at inlet flow rate of 4 m/s (volumetric flow rate of 3.76 m^3/hr).

The results provides the foundation for further particle tracking simulations, as shown in **Paper V**, where the simulated particle tracks are compared with PEPT-obtained particle tracks and show analogous characteristics.

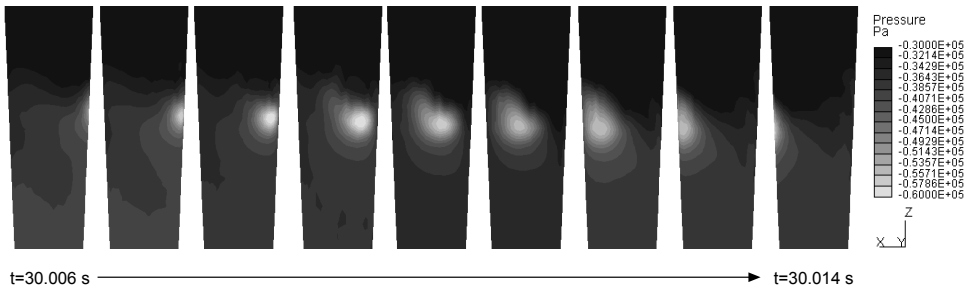

Figure 4.6: Profile plot for the pressure on the wall viewed from a fixed angle. From left to right: one graph per ms from 30.006 s to 30.014 s. The period of the rotation is estimated to be 14 ms, giving frequency of 71.43 s^{-1} in this case.

Paper III: *Using a PET camera to track individual phases in process equipment with high temporal and spatial resolutions: algorithm development*

In this paper the parameters in the positioning algorithm affecting the accuracy of PEPT have been scrutinized. The spatial distribution and density of the cutpoints projected onto $x - y$ plane is extracted and displayed. As the positioning algorithm adopts the gradually-shrinking-window strategy to find the most probable location of the particle, the final window has to be small enough to exclude false cutpoints yet ample enough to enclose the true cutpoints. The 3-D standard deviations of the bead positions as a function of dimension of the final spatial window, as shown in Figure 4.7, shows highest positioning accuracy as the window size reaches 16×16 mm^2.

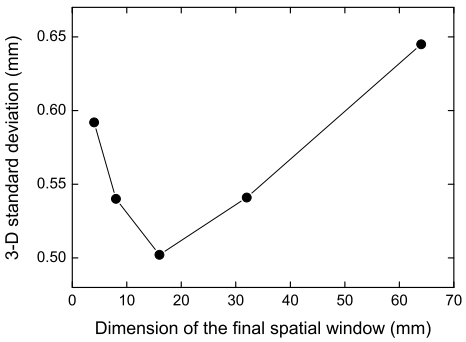

Figure 4.7: 3-D standard deviations of the bead positions as a function of dimension of the final spatial window for averaging the enclosed cutpoints.

As the TruePoint PET camera inserts a timing mark into the data stream every 1 ms, the default temporal resolution is 1 ms. The temporal resolution was enhanced to 0.5 ms and 0.25 ms by splitting up the consecutive data, which, as a tradeoff, results in downgrading the positioning accuracy, as shown in Figure 4.8. The trajectories obtained with temporal resolution of 0.5 ms are shown in this paper and in **Paper VI**.

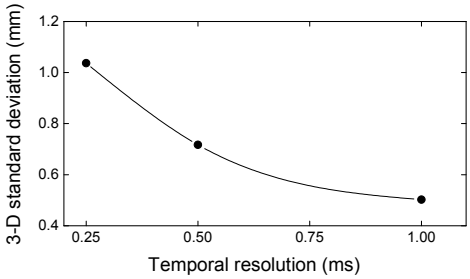

Figure 4.8: 3-D standard deviations of the bead positions as a function of temporal resolution.

Paper IV: *Detecting anomalies in the separation process in a hydrocyclone using a medical PET scanner*

This paper focuses on utilizing PEPT as a means to detect anomalies in the flow field in a hydrocyclone. Tracking the particle firstly shows that the particle spends aberrantly long time in the hydrocyclone operated without underflow compared to the hydrocyclone with 20% underflow (20% of the inflow was let through the underflow outlet). Studying the tracks in detail shows that the particle took excursions around a specific axial position low in the cyclone, which causes the abnormally long residence time, as having been shown in **Paper I**. Cartesian particle positions were then transformed to cylindrical coordinates using the in-house developed cyclone axis finding algorithm, which manifests the anomaly in each velocity component, and allows the flow field to be further quantitatively analysed in **Paper VI**.

The radial, tangential, and axial velocities of the particle were derived from the cylindrical coordinates, showing conspicuous axial reversal and abrupt decay in tangential velocity for the long-residence-time case. Plotting the cylindrical velocity components as a function of axial position indicates the section of anomaly occurring. The velocity components as a function of time indicates the anomaly starting time and period, showing that the particle spent around half of the total residence time being trapped in the anomalous flow section in this case. After escaping from the highly fluctuated velocity section, the particle was transported at lower axial and tangential speeds, which indicates that the 'end of the vortex' has caused the particle's violent and directionless flow followed by weak and inefficient flow.

Paper V: *PEPT: An invaluable tool for 3-D particle tracking and CFD simulation verification in hydrocyclone studies*

This paper mainly focuses on simulating particle trajectories by Eulerian-Lagrangian CFD, as well as comparing the simulation and PEPT results. As obtained in **Paper II**, the 'end of the vortex' (EOV), i.e. the vortex end's bending to the wall and rotating on the wall, has been simulated using the LES (large eddy simulation) turbulence model. 3-D particle trajectories, as shown in Figure 4.9, were obtained using Lagrangian tracking in the pre-calculated, EOV-encompassed fluid flow field. The superposition of simulated particle trajectory on the static pressure, as shown in Figure 4.11, shows a strong correlation between the particle behaviors and EOV.

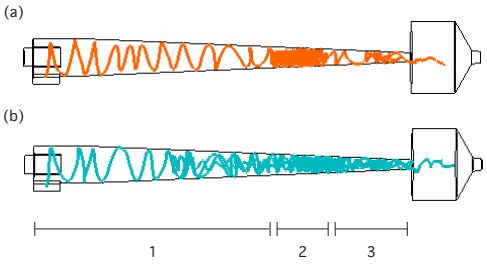

Figure 4.9: CFD simulated particle trajectory.

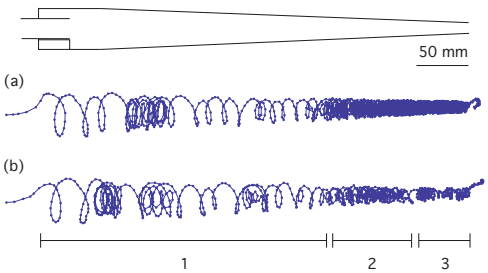

Figure 4.10: The trajectories of a particle in the hydrocyclone under the same operational condition obtained by PEPT. The numbers of effective cutpoints in each millisecond are in the order of 10^5 and 10^3 in (a) and (b), respectively. In (b) Savitzky-Golay filtering method has been applied on a series of 5 positions with a polynomial order of 2 to eliminate the fluctuations due to less numbers of effective cutpoints and the consequent scatter in the particle locations. Detailed elaboration and analysis of varies filtering methods are presented in **Paper VI**.

The particle flow in both simulation and PEPT experiments can be divided into three stages as approximately indicated below Figures 4.9 and 4.10: In the first stage, the particle's regular swirling motion toward the underflow outlet is clearly visible. In the second stage, the particle was affected by a strongly turbulent flow at a specific axial position, as indicated around the arrow in Figure 4.11 (for simulation) and the bar below Figure 4.12 (for PEPT experiment). In the third stage, the particle, having passing the turbulent region, continues its slower spiralling path, as can be seen in Figure 4.12 where the adjacent points are closer after the turbulent section, and often loses its direction and spiral pattern as shown in Figure 4.11 (e) below the arrow (for simulation) and as shown in Figure 4.13 (for PEPT experiment) which is the continuation of Figure 4.12 (b).

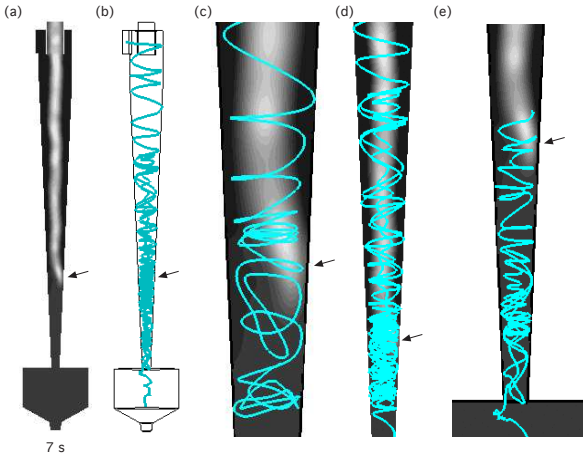

Figure 4.11: The correlation between the particle behavior and the 'end of the vortex' (EOV). The position on the wall where the vortex core bends and attaches is indicated by an arrow. (a) The contour plot of static pressure showing the core attached to the wall at the axial position of EOV. (b) The whole particle track. (c)-(d) Detail showing the particle passing EOV: The particle trapped by the EOV, moving at a disordered pace, drawn into the upward inner vortex, and centrifuged out again. (e) The particle experiencing weak swirling and further axial flow reversals after escaping from the EOV.

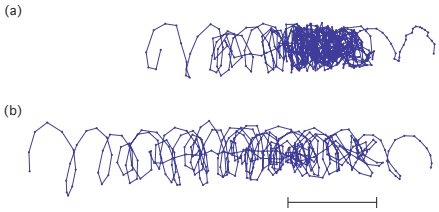

Figure 4.12: The particle's swirling motion is affected by a strongly turbulent flow down in the hydrocyclone. The bar underneath indicates the turbulent region.

Figure 4.13: The particle in Figure 4.12 (b) has passed the turbulent region and continues spiraling in a slower and staggering manner.

The similar particle behaviors obtained by PEPT and CFD simulations confirms that the sudden random movement and the later slow transport, both were also observed by PEPT in **Paper I**, are caused by the 'end of the vortex' phenomenon.

Paper VI: *A Lagrangian study of liquid flow in a reverse-flow hydrocyclone using positron emission particle tracking*

This study aims to investigate liquid flow in the hydrocyclone by following neutral-density particles using PEPT. Both modifying the density of the particle and modifying the density of liquid have been proven feasible to make particles neutral-buoyant. Considering the safety and workability, salt, i.e. NaCl, was chosen as an additive to modify the density without significantly altering the viscosity of liquid. This, however, poses a challenge for positioning the tracer since exchange of the ^{18}F ions by Cl ions would decrease the activity on the particle and the ^{18}F spreading in the liquid could increase the noise. The low signal-to-noise ratio can cause the original algorithm, as described in **Paper III** and applied in **Paper I, IV and V**, to identify wrong tracer positions, of which an obvious example is visible in Figure 4.14 (a). A refined algorithm has been developed to overcome this situation: Rather than locating the particle in the whole FOV for every time step, the refined algorithm takes into account only the 2-D cutpoints around the previous position. In this way, a great part of the noise has been discarded from the outset. Compared with the original algorithm, the refined one can bracket more cutpoints in the final 16^3 mm^3 window, the noise has less effect, and the trajectories are smoother, as shown in Figure 4.14 (b) and other examples in this paper. Smoothing methods, as post-signal processing, including weighted adjacent-averaging, Gaussian filtering, FFT (fast Fourier transform) filtering, and the Savitzky-Golay method, has further been applied to remove noise. The effects of these methods with varied parameters are discussed in the paper.

In fact, it can probably be recommended to apply a low-pass filter with a width of 1 ms as a matter of course to raw PEPT data, since this will filter out scatter due to the noise inherent in the PEPT method and give a clearer picture of the real motion of the particle. However, such filtering can also have detrimental effects, as described in the following paragraphs.

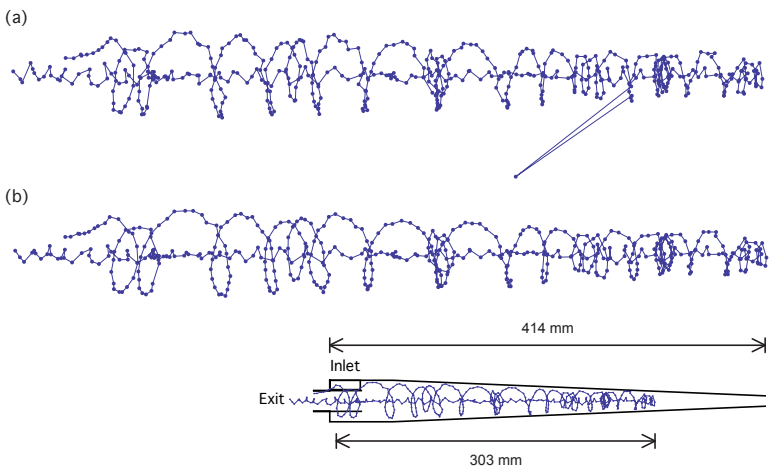

Figure 4.14: (a) Trajectory obtained using (a) algorithm 'Method 1' and (b) refined algorithm 'Method 2' as described in this paper and in Section 3.5. Trajectory duration: 505 ms

The tangential, radial, and axial velocities in the hydrocyclone can be studied in detail by further calculating the coordinates of the tracer. An in-house developed code determines the axis of the cyclone and transforms the Cartesian coordinates of tracer positions to cylindrical coordinates. It is found that in the cylindrical part of the hydrocyclone the tracer accelerates after entering the cyclone through the slot inlet and decelerates while rotating closer to the inlet area. This is consistent with the classical cyclone performance models, where the initial acceleration is due to the constriction of the inlet jet just beyond the inlet and the subsequent deceleration is due to friction with the wall. The tangential velocity as a function of radius can be fitted with equations of a vortex with solid-body rotation in the center surrounded by a region of near loss-free rotation.

The velocity components and the rotation radii as a function of the axial position of the cyclone illustrate the instantaneous turbulence in the flow field. The time series details the relation between the change of radius, the tangential, radial, and axial velocities during turbulence occurrence.

Transforming the coordinates of the smoothed trajectories to cylindrical coordinates with the cyclone axis as the axis of the coordinate system shows that the Gaussian filtering with a width (standard deviation of the Gaussian function) of 1 and the weighted adjacent-averaging method shrink the trajectory toward the cyclone axis and obliterate the characteristics of the 'loss-free vortex'. Therefore, while reducing the impact of noise, the smoothing methods and their parameters have to be carefully chosen to preserve the characteristics of the flow pattern.

4.2 Unpublished results

CFD study on the effect of the underflow in a hydrocyclone

Background

The 'end of the vortex' (EOV) has been experimentally observed in a hydrocyclone using a Lagrangian flow visualisation technique—positron emission particle tracking (PEPT), as shown in **Paper I, IV and V**. The single-phase flow field in the same hydrocyclone geometry has been studied with CFD as presented in **Paper II**, showing that at certain inlet velocities the vortex end deviates from the central axis and bends to the wall of the hydrocyclone body.

In hydrocyclones an underflow fraction is a fraction of the total inflow which is caused to flow out of the underflow outlet. Adjusting the underflow discharge rate can be a means to regulate the underflow density. For instance, in Ref. [2] automatic underflow regulators have been used to help keeping the underflow density stable as the solids content in the feed varies. How the underflow affects the flow and specifically the EOV has been investigated using PEPT in **Paper IV**. In this work, analogous CFD simulations were carried out to numerically study the effect of underflow on the EOV and the particle trajectories. The simulation results are compared with results from the PEPT experiments.

CFD model

In CFD simulations the geometry of the hydrocyclone with a solid collection chamber attached to the underflow outlet was built to comply with that used in the PEPT experiments as presented in **Paper I** and **Paper IV–VI**. The underflow outlet boundary condition was prescribed on the solid collection chamber, the same location as the outlet in the experimental setup. 'Trimmed mesh' were used to generate the grid. The computational mesh consists of 331745 cells.

The fluid in the hydrocyclone in the simulations and experiments was water. Fluid velocities similar to those used in the experimental work were prescribed at the inlet boundary. When underflow was used, the flowrate at underflow outlet was set as 20% of the total flowrate, the same ratio as in the experiments.

Previous experience has shown that LES (Large Eddy Simulation) turbulence model is by far the best for correctly mimicking the effect of the turbulence in the strongly swirling, confined flows in cyclones [83, 84]. In this work, the LES turbulence model, in combination with the subgrid-scale (SGS) model of Smagorinsky, was applied using the commercial CFD package Star-CD. Spatial discretization is performed using MARS (Monotone Advection and Reconstruction Scheme). A three-time-level scheme using the SIMPLE (Semi-Implicit Method for Pressure-Linked Equations) algorithm was used for temporal discretisation. Standard wall functions were used at the wall boundaries.

The two-phase flow was simulated using the Eulerian-Lagrangian approach with one-way coupling. The density of the particles in the simulations was 2560 kg/m^3 and the diameter 90 μm. The particles were assumed to be non-rotating spheres under relatively low shear stress variations to simplify the equation of motion. The forces acting on the particles were thus considered to be linear drag and gravity neglecting the effects of lift forces and unsteady forces, namely virtual mass and the history integral. The equation of motion for the particles was thus:

$$m_p \frac{d\mathbf{u}_p}{dt} = \frac{1}{2} C_d \rho A_p \left|\mathbf{u} - \mathbf{u}_p\right| (\mathbf{u} - \mathbf{u}_p) + m_p \mathbf{g} \tag{4.1}$$

where $\mathbf{u}$ and $\mathbf{u}_p$ are the fluid and particle velocities respectively, C_d is the drag coefficient, ρ is the fluid density, and A_p is the cross-sectional area of the particle measured in a plane perpendicular to its motion.

Mesh convergence tests were carried out using 775488 cells to assure the validity of solutions. The time-dependent pressure distributions simulated using the present mesh and the refined mesh under same conditions resembled each other sufficiently well.

Results and discussion

Figure 4.15 (a) shows the simulated cross-sectional pressure distributions at an inlet fluid velocity of 4 m/s (volumetric flowrate 3.76 m^3/hr) and an underflow discharge of 0.752 m^3/hr (20% of the total flowrate), displaying the vortex core as a trough in the static pressure. Initially, as the vortex is formed, the vortex core can be seen to attach to the wall, but later in the simulation the vortex core seems to be fluctuating and it is not easy to determine where the core ends; the vortex motion seems to be strongly dissipated in the lower part of the cyclone. This represents a clear difference with the case of no underflow, as shown in **Paper II** and **Paper V** as well as in Figure 4.16, where the vortex end was seen to attach to the cyclone wall and remain there around some steady level. This indicates that operating the hydrocyclone with 20% underflow centralizes the vortex, similarly to what has been observed in gas cyclones [85].

Figure 4.15 (b) shows the cross-sectional pressure distribution at simulation time 15.1 seconds and Lagrangian simulations of the track of a single particle superposed on the cross-sectional pressure distribution. As the vortex is gradually dissipates in the bottom of the cone section, the rotational motion of the particle becomes less regular. Overall, in the simulations the particle swirled smoothly and reached the particle collection chamber quickly. Particle tracks obtained in PEPT experiments with inlet velocity 3.76 m/s (volumetric flow rate 3.53 m^3/hr) and 20% underflow discharge are shown in Figure 4.15 (c) as well. Like in the simulations, in the experiment the particle also swirled more or less straight through the hydrocyclone. The particle in the experiments does take many more turns than that in the simulations, probably indicating that the vortex is more intense in the experiments and to a lesser degree dissipated in the bottom.

Comparing the simulated pressure distributions and particle tracks in the case of having 20% underflow discharge with those with no underflow, as shown in Figure 4.16, clearly

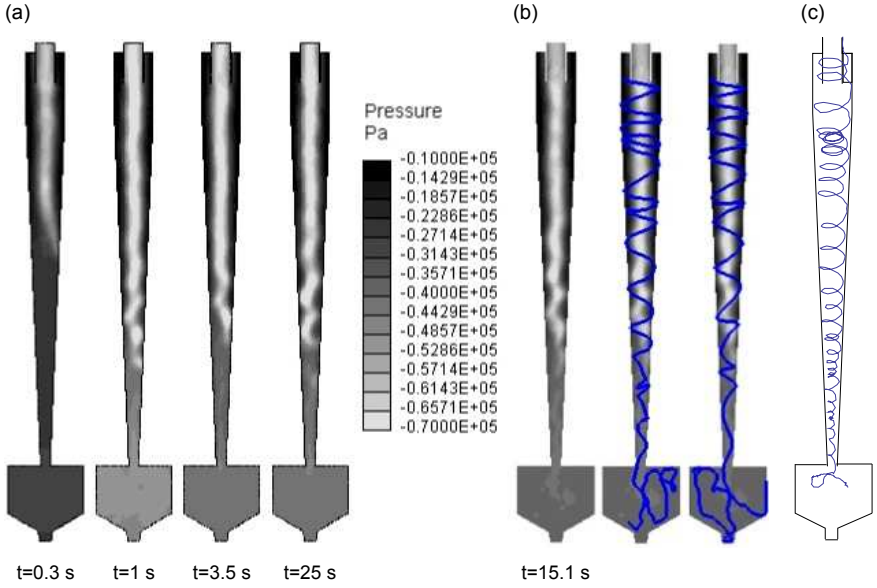

Figure 4.15: (a) Cross-sectional contour plots of the pressure simulated at an inlet flow velocity of 4 m/s and an underflow discharge of 20% of the total flowrate. (b) The cross-sectional pressure distribution after 15.1 seconds and trajectories of particles which pass through the cyclone at around 15.1 seconds. (c) The particle trajectories obtained in PEPT experiments with inlet velocity 3.76 m/s (volumetric flowrate 3.53 m^3/hr) and 20% underflow discharge. The average number of 2-D cutpoints obtained by Method 2, as used in **Paper VI**, in the final 16^2 mm^2 window is 19486. The track duration is 455 ms. Gaussian filtering with a standard deviation of 0.5 has been applied to further remove noise from signals.

shows how the underflow discharge rate affects the flow field and consequently the particle tracks and the particle residence time.

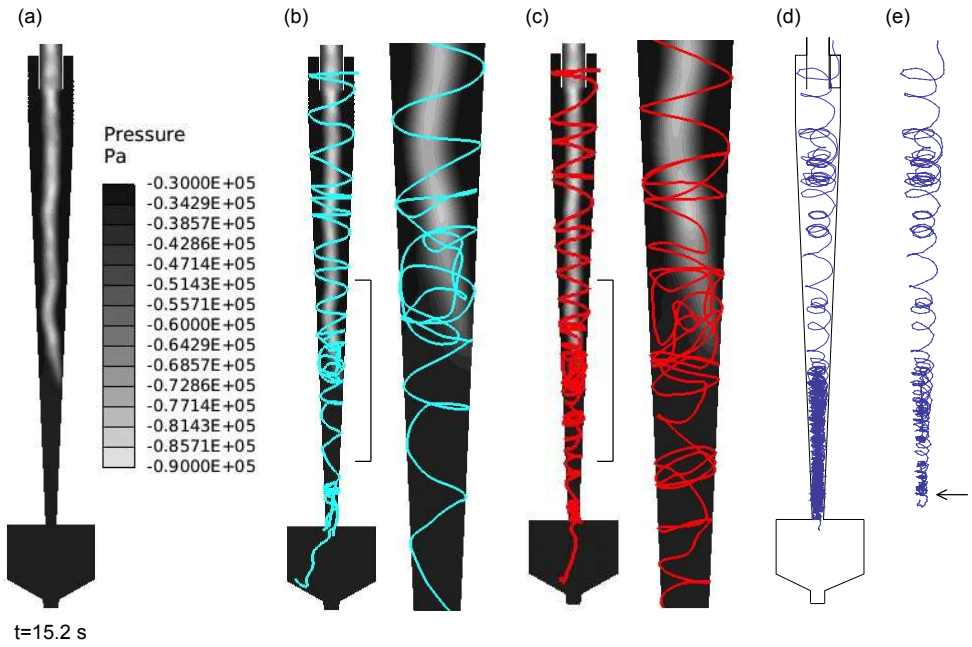

Figure 4.16: (a) Cross-sectional contour plots of the pressure at 15.2 sec simulated at an inlet flow velocity of 4 m/s and no underflow. (b) and (c) The trajectories of particles, which pass the middle of the cyclone at around 15.2 sec and magnifications of the same tracks around the EOV section. (d) The particle trajectories obtained in PEPT experiments with an inlet velocity 3.6 m/s (volumetric flowrate 3.4 m^3/hr) and no underflow. The average number of 2-D cutpoints obtained by Method 2, as used in **Paper VI**, in the final 16^2 mm^2 window is 16604. The track duration is 3020 ms. Gaussian filtering with a standard deviation of 0.5 has been applied to further remove the noise from the signals. (e) The particle positions obtained every ms are closer spaced below the arrow, which indicates an abruptly decreased transport speed after this point. This transition in speed occurred between 845–890 ms. It took less than 0.9 s for the particle to approach the bottom of the cone section. However, due to the likely EOV anomalous flow field, the particle spent around 2 s, experiencing flow reversal and passing through the speed-changing area low in the cyclone for several times, before finally entering the particle collection chamber.

The detailed behaviour of the vortex end during the simulation as it attaches to the wall and descends along it, possibly to a steady position, for the case of no underflow has been shown in **Paper II**. Figure 4.16 shows the cross-sectional pressure distribution and Lagrangian simulations of a single particle at the simulation time 15.2 sec. The picture illustrates how the particle loses its regular swirling motion as it approaches the EOV region and begins to flow irregularly, moving upwardly and downwardly in this region. The particle, after escaping from the EOV region, does not recover its swirling motion very well, as can be seen in Figure 4.16 (c). Even though the particles did restart spiraling under the EOV, their velocities were significantly reduced and the

downward motion of the particles was easily disturbed by turbulence and collision with the wall while passing toward the narrow underflow outlet. It seems that underneath the EOV the swirling flow field of the inner and outer vortex is only weakly present. The reason can be that the vortex core's rotation on the wall induces a much weaker, secondary vortex below the EOV [1]. Similar particle behaviours with disordered paths were also clearly observed in PEPT experiments with similar inlet velocity as show in Figure 4.16 (d), where a sudden decrease in velocity can be observed right after the arrow in Figure 4.16 (e). These phenomena have been observed in experiments with a higher velocity, as shown in **Paper I** and also lower velocities (unpublished). The abruptly weakened flow and inefficient transportation has also been observed in the gas cyclones; a section with particle deposition on the wall is often visible below lowest position of the EOV [16].

Chapter 5

Concluding remarks and further work

In this work we have developed and improved positron emission particle tracking (PEPT), and applied this technique to track particles and quasi-fluid elements in a hydrocyclone. By the methods developed in this work, namely improved radioactivity labelling technique, data processing algorithms and the Siemens Biograph TruePoint 3-ring PET system, the centroid of a tracer with the harmonic mean size of 560–700 μm in air or pure water can be determined every millisecond with a standard deviation of less than 100 μm in all three coordinate directions. The temporal resolution can be further refined to 0.5 and 0.25 millisecond by dividing the time-series data. Efforts have been also placed on de-noising as post data processing for cases where the tracking is conducted in decreased signal-to-noise conditions.

The high-resolution particle tracking makes it possible to observe closely the separation process in a hydrocyclone. The radial, tangential and axial velocities were computed by transforming the Cartesian coordinates to cylindrical coordinates using an in-house algorithm developed to determine the cyclone axis. The PEPT-obtained velocity distributions are compared and fitted with theoretical cyclone velocity distribution functions.

By using PEPT we scrutinized quantitatively the particle behaviors influenced by the 'end of the vortex' (EOV) phenomenon, which has never been experimentally deciphered in high resolution. The detailed difference between the particle velocities affected and unaffected by EOV has been analyzed.

We carried out CFD simulations, employing the LES (Large Eddy Simulation) turbulence model, in a hydrocyclone of geometry and operation conditions identical to the experiments. The simulated pressure distribution shows the EOV occurring. The particle tracks computed using Lagrangian-Eulerian approach agree well with PEPT-obtained particle trajectories for all features reflecting the EOV influence. The Lagrangian particle tracking, verified by PEPT, is proven a credible tool to predict the presence of the EOV and its effect on the particle's travelling and the resulting residence time.

The simulated flow patterns obtained in this work provide prediction on the pressure distribution with the EOV present, as well as precessing frequency of the vortex end, which need to be further juxtaposed with experimental measurements.

Further, CFD simulations of a hydrocyclone using the LES turbulence model and Lagrangian particle tracking simulations have been performed to study the effect of operational conditions on the 'end of the vortex' phenomenon and to compare with results of PEPT experiments. The simulation results show that the EOV was not present in the hydrocyclone with 20% underflow discharge, while it was clearly presented in hydrocyclone with no underflow. In the case of no EOV the particles swirled through smoothly, but in the case of EOV presenting the particles suffered recirculating, disorganized movement, and long residence time. The PEPT-obtained trajectories in these different cases agree well with the simulated tracks.

Preliminary results of experimentally and numerically studying the influence of the inflow rate on the 'natural vortex length' has been obtained in the course of this work and will be further completed.

The theoretical and experimental studies of EOV is essential for modelling the cyclone performance. Suggestions for further work include:

- Compare simulations and experimental measurements of pressure distribution, flow field, and characteristics of the vortex end precessing.
- Study the influence of the inflow and underflow rate, as well as varying cyclone geometries, e.g. symmetrical inlet, on the 'natural vortex length' both experimentally and numerically.
- Conduct CFD simulations with models involving a finer grid to obtain quantitative agreement to predict characteristics and influence of EOV for varied hydrocyclone geometries and operating conditions.
- Based on thorough experimental and numerical investigations, construct a theoretical model based on physical principles to predict the relationship between operation condition, cyclone geometry, wall roughness, natural vortex length, and the precessing frequency of the vortex end.

The development and verification of PEPT technique constitute a great part of this work. PEPT, as utilised herein, has been proven a high resolution technique for visualising complex and dynamic processes. Suggestions for further developing and applying the PEPT technique include:

- Incorporate the time of flight (TOF) information acquired by the TOF PET scanner (see, e.g., [86, 87]) to further reduce noise, accelerate data processing and enhance resolution.
- Apply the multi-particle tracking as described in Section 3.5 to study rotation, collision, devision, coalition, and adhesion.
- Construct the wax coating device to render the tracer density modification, as described in Section 6.6, more controllable and efficient.

Chapter 6

Scientific results

I

Paper I

6.1 Particle flow in a hydrocyclone investigated by positron emission particle tracking

Yu-Fen Chang, Catalin G. Ilea, Øystein L. Aasen and Alex C. Hoffmann

Chemical Engineering Science 66, 18 (2011), 4203–4211

Chemical Engineering Science 66 (2011) 4203–4211

Contents lists available at ScienceDirect

Chemical Engineering Science

journal homepage: www.elsevier.com/locate/ces

Particle flow in a hydrocyclone investigated by positron emission particle tracking

Y.-F. Chang *, C.G. Ilea, Ø.L. Aasen, A.C. Hoffmann

Department of Physics and Technology, The University of Bergen, Allégaten 55, 5007 Bergen, Norway

ARTICLE INFO

Article history:
Received 16 November 2010
Received in revised form
15 March 2011
Accepted 1 June 2011
Available online 15 June 2011

Keywords:
Separation
Multi-phase flow
Turbulence
Visualization
Hydrocyclone
Positron emission particle tracking

ABSTRACT

The flow of a particle through a hydrocyclone acting on water has been studied by positron emission particle tracking (PEPT). The positron-emitting radioactive tracer was ^{18}F. It was found that the activity on an ion-exchange resin particle labeled with ^{18}F did not leach out into the water during the duration of an experiment. In the state-of-the-art PET camera it is shown to be possible to locate the centroid of the tracer particle with a standard deviation of only about 0.2 mm once per ms, making both the temporal and spatial resolution high enough to trace the particle in its very fast motion through the hydrocyclone. The design of the hydrocyclone was a modified Stairmand high-efficiency geometry with a long cone. The results are, among other things, shown as spatial tracks of the tracer particle as it moves through the hydrocyclone. Several interesting features were seen. The particle path, although the particle was much larger than the cut size of the cyclone, exhibited excursions into the inner, upwardly directed, part of the vortex giving rise to recirculatory loops. Moreover, at a particular position low in the cyclone, the particle exhibited a complicated flowpattern moving up and down repeatedly across this position. Careful analysis of the motion is presented, particularly of the motion low in the hydrocyclone, on basis of which it is made likely that this position represents the end of the vortex in the hydrocyclone.

1. Introduction

1.1. Reverse-flow cyclones

We give a short introduction to the flow in reverse-flow cyclones, for those not familiar with them.

In a reverse-flow cyclone the particle-laden fluid is brought to swirl either by being led into the cyclone tangentially or using swirl-vanes (Peng et al., 2005). In the separation space the particles are centrifuged out to the wall, along which they are transported to the particle outlet. The fluid leaves the separator through the 'vortex finder' in the roof of the cyclone. In the cyclone body the axial flow direction is toward the particle exit in outer part of the vortex, referred to as the 'outer vortex', while the axial flow direction is reversed in the 'inner vortex'. The particle transport along the wall to the particle exit is due to the axial flow, not due to gravity, and cyclones will normally work the same whether mounted horizontally or even upside-down.

In general, cyclones will separate large particles better than small ones, and the size, which is just separated with a 50% efficiency, is referred to as the cyclone 'cut size'. In 'hydrocyclones', as we are studying in this paper, the fluid carrying the particles is a liquid, most often water.

1.2. Literature survey

1.2.1. Experimental results for the flow in hydrocyclones

Hydrocyclones are characterized by the performance, e.g. the grade efficiency, the overall efficiency, and the overall pressure loss, and it is important to increase the understanding of the basic phenomena, which have impact on the performance, such as the velocity field and the flow of the dispersed phases.

Phase Doppler anemometry (PDA) is one way of acquiring the velocity distribution and the particle size of a solid phase in a hydrocyclone by detecting laser light scattered by a particle at two angles (e.g. Fisher and Flack, 2002; Marins et al., 2010; Monredon et al., 1992). Another technique, particle image velocimetry (PIV), is also used to determine the mean velocity of particles or droplets (hereinafter termed 'particles') in a hydrocyclone by cross-correlating photo frames containing a number of particles (e.g. Marins et al., 2010).

While the above methods provide the average velocity fields in hydrocyclones, another approach is to track an individual particle of a dispersed phase in space and time, i.e. the Lagrangian tracking. By obtaining the trajectory, it can be seen how a particle reacts to

* Corresponding author. Tel.: +47 55582785; fax: +47 55589440.
E-mail addresses: yu-fen.chang@ift.uib.no (Y.-F. Chang), alex.hoffmann@ift.uib.no (A.C. Hoffmann).

0009-2509/$ - see front matter © 2011 Elsevier Ltd. All rights reserved.
doi:10.1016/j.ces.2011.06.001

and interacts with the flow around it under the specific conditions and any local instabilities can be observed in detail.

Bamrungsri et al. (2008) photographed a dyed oil drop in water hydrocyclones using a high-speed camera. They demonstrated a method to observe the path of a neutral density object in two dimensions. The time resolution is about 2 ms, and the spatial resolution depends on the optical system and the camera sensor construction. In their study, only one section of each hydrocyclone was pictured, but the field of view can be expanded if more cameras are used or by sacrificing some spatial resolution.

Wang et al. (2008) also utilized a high-speed camera to record the motion of a vegetable seed with density of 1.14 g/cm^3 in a water hydrocyclone. Two-dimensional trajectories were plotted by recording the positions in consecutive frames. This study showed different routes that a particle may experience for different reporting outlets or residence times, or as the size or point at which it was injected was changed. Though it is possible to set up another camera in an orthogonal direction to obtain 3-D trajectories and thus calculate the velocity of the particle, the spatial resolution can be a concern.

The 2-D particle paths obtained by Wang et al. (2008) show that local or instantaneous instabilities in the flow field have a huge influence on the particle path, and therefore impacts on the separation performance, something which cannot be revealed by studies of average velocity distributions.

In order to enhance our understanding of the separation mechanism and potential problems, which are essential for theoretical model formulation and design improvements, trajectories from which precise individual velocities and ensemble-average velocity fields can be derived, need to be acquired.

1.2.2. Numerical studies of the particle flow in hydrocyclones

As it is not easy to follow the particle in a hydrocyclone experimentally, computational fluid dynamics (CFD) simulations may serve as an alternative method to illustrate particle trajectories.

Hsieh and Rajamani (1991) presented computed 2-D trajectories of limestone particles in a water hydrocyclone for different entry points and different particle sizes. The trajectories were obtained by solving the particle equation of motion in a pre-calculated liquid flow field, i.e. the Lagrangian particle tracking in a pre-calculated Eulerian simulation.

Neesse and Donhauser (2000) solved numerically for the velocities of the fluid and solid particles in a hydrocyclone for the case of high solid concentrations by modeling adopting iterative algorithms for 2-D time-dependent flow processes. The 2-D paths of individual particles were traced for different feed concentrations. Particles in the cut-size range were found to travel in large convective patterns at higher concentrations, leading to increases in residence time and worse separation.

Cullivan et al. (2003) performed a transient 3-D CFD simulation based on a second-order-accurate pressure-strain Reynolds-stress turbulence model. The 3-D particle tracking featured stochastic turbulent transport of particles. The random nature of the particle paths was accounted for by superimposing stochastic contributions on the particle velocity matching the local turbulence and depending on the particle size. This led to local radial velocity variations, resulting in the particles being drawn into the inner vortex, i.e. the upward core flow, and therefore subject to recirculatory motion in the hydrocyclone.

In Yang et al. (2004), the turbulent flow field in a hydrocyclone was calculated by solving the Reynolds averaged Navier–Stokes and continuity equations using the renormalization group $\kappa-\varepsilon$ turbulence model. 3-D trajectories of particles released from different positions in the hydrocyclone inlet were computed by the Lagrangian particle tracking, i.e. integrating the particle equation of motion in the flow field. The trajectories showed that the paths of the particles were significantly influenced by the positions at which they were injected at the inlet.

1.2.3. Positron emission particle tracking (PEPT) for process technology

The technique, which is the focus of this paper, is 'positron emission particle tracking' (PEPT). Having been developed within the latest 20 years this technique is now used for research in process technology in a few centers around the world. PEPT shares the detection principle with the medical image technique, positron emission tomography (PET). While PET is based on detection of spatially distributed radioactive sources (positron emitters) and image reconstruction techniques, and therefore provides the time-dependent distribution and concentration of radioactively labeled substances, PEPT locates a point-like positron emitter by cross-triangulation (see below). Both the spatial and temporal resolutions are much higher for PEPT than for PET.

Since this method is normally used in the medical world, the camera, with which the detection is carried out, is often referred to as a PET camera.

The radioactive decay process which forms the basis of the detection principle is as follows. The nuclei of the radioisotopes used contain surplus protons and undergo positive beta decay, where a proton is converted into a neutron, a positron and a neutrino. The positron, after having lost energy moving through the medium, annihilates with an electron. For energy conservation, the annihilation usually leads to back-to-back emissions of two gamma photons of 511 KeV each. These are detected by two sensors, and a 'line of response' (LOR) is drawn between them, indicating that the decay event took place somewhere along this line. The position of a point-like tracer labeled with radioisotopes can thus be determined by detecting and cross-triangulating a number of these back-to-back gamma-ray emissions.

Because of the high penetrating power of gamma-rays, tracers in equipment with high solid concentrations, as well as opaque fluids and walls, can be detected unhindered, while those conditions would cause problems using the methods described above. Since different phases can be labeled separately, PEPT is suitable for studying multi-phase flows. For instance, the solid flow in an interconnected fluidized bed system was investigated using PEPT by Stellema et al. (1998). Schaafsma et al. (2006) used PEPT to track a radioactive particle mimicking a granule as it moved in tapered fluidized bed granulators. Depypere et al. (2009) used the technique to visualize and quantify the powder movement inside a 'Glatt-Powder-Coater-Granulator' tapered fluidized bed coater. Chan et al. (2009) studied particle motion in a circulating fluidized bed riser, focusing on PEPT-imaging of the bottom section. In addition to the studies of fluidized beds, PEPT has also been used to study flows in rotating drums (e.g. Ding et al., 2002; Ingram et al., 2005; Parker et al., 1997) and stirred vessels (e.g. Barigou et al., 2009; Fishwick et al., 2005a), flows generated by turbines (Fishwick et al., 2005b; Pianko-Oprych et al., 2009), paste flows (Wildman et al., 1999), inclusion movements in castings (Griffiths et al., 2008, 2010), and other processes.

The possibility of in situ PEPT measurements at industrial plants was demonstrated by Ingram et al. (2007). A portable PEPT camera was constructed to track particle motion in a 750 mm diameter pilot scale pressurized bed in BP's Hull Research and Technology Centre.

The most relevant to the present research is using PEPT to obtain the particle trajectories in gas cyclones at various values of solid loading, axial gas velocity and cyclone diameter (Chan et al., 2009). It was found that at low solid loading, the particles spiral in both cylindrical and conical parts of the cyclone, while at high

solid loading, the particles stop their spiral motion somewhere on the wall and after that move directly down to the dust outlet.

Hoffmann et al. (2005) has conducted an extensive analysis on the scatter of the tracer position within the study on fluidized bed by PEPT. The structure of list-mode data output from Siemens ECAT EXACT HR+ PET camera were interpreted and the spatial resolution of 1 mm per millisecond was obtained. This work laid the foundation for our work using a medical PET camera to study fast-moving particles in a hydrocyclone.

2. Experimental

2.1. The hydrocyclone system

Fig. 1 shows a diagram of the experimental rig, consisting of the hydrocyclone incorporated in a recirculating system. A centrifugal pump (Cotech XKJ-1305S), located downstream of the liquid tank and the particle injector, propels the liquid into the hydrocyclone. The previously labeled (the labeling is described below) tracer particles are charged into the pipe using a syringe connected with a hypodermic needle. The needle with a diameter of 0.5–0.9 mm and a length of 16–25 mm allows for precise control the number of injected particles.

The inlet flow rate and pressure can be regulated by a control valve on the inlet pipe.

Particles with sizes larger than the cut size will be deposited in the dust collection chamber beneath the cone. Fitted to the dust collection chamber is a pipe allowing the use of underflow from the cyclone, equipped with a control valve for controlling the underflow rate. Flow meters and pressure indicators are installed upstream of the hydrocyclone inlet and on the overflow pipe for monitoring the flow rate and the performance of the hydrocyclone. Both the underflow and the overflow return to the tank.

The hydrocyclone used in the experiments is a cylinder-on-cone design with a slot inlet, configured to resemble the geometry of the Stairmand high-efficiency cyclone (Stairmand, 1951) with a modified prolonged cone.

The cone of the cyclone is rather long for a particle-fluid separator, but this type of geometry is widely used in the oil industry for desanding of water. The purpose of the larger project, carried out in collaboration with a major oil company, of which this study is a part, is to extend the application of such desanding equipment to other types of particle-liquid mixtures.

This design has a body diameter of 40 mm and a total length of 414 mm. The cylindrical section measures 60 mm in height, and comprises a slot inlet of 29 mm height and 9 mm width. The diameter and the length of the vortex finder are 20 and 30 mm, respectively. The diameter of the underflow outlet is 10 mm.

The hydrocyclone is made of glass-fibre reinforced polymer and is manufactured by a 'wet lay-up technique': First a metallic mold of the inner geometry of the cyclone is fabricated and its surface is coated with mold-release agent. Then a layer of polymer is spread onto the surface of the mold, followed by a glass-fibre sheet. The polymer and the sheet are applied in turn to a required thickness. During the process it has to be ensured that the glass-fibre sheets are completely wetted and air bubbles are removed. In the end the polymer is cured to form cross-links and harden. The material and the technique are convenient for constructing a small-diameter cyclone with the necessary surface smoothness and pressure resistance.

2.2. Preparation of tracers

To label a tracer particle, the $^{18}O(p,n)^{18}F$ nuclear reaction was carried out with the help of a cyclotron to produce dissolved ^{18}F (half-life, 109.8 min) ions, which can be taken up by organic or inorganic materials through ion-exchange or surface adsorption.

Fan et al. (2006) reported that strong-base anion exchange resins are superior to weak-base anion exchange resins regarding radioactivity uptake because the affinity of ^{18}F ions to the strong-base anion resins is higher. It is also reported that the radioactivity on a single bead depends on both the ^{18}F concentration in the solution into which the particles is immersed and on the immersion time, i.e. when the immersion time exceeds 25 min, the decay rate is greater than ^{18}F exchange rate, and the radioactivity on the particle starts to decrease.

Here the strong anion exchange resin beads Amberlyst A26 Hydroxide Form (Acros Organics) with sizes from 390 to 700 μm were used. A photo taken of a 441 μm bead under the microscope is shown in Fig. 2. Their macroreticular, porous structure provides more binding sites and is therefore beneficial for radioactivity uptake.

The beads were immersed into 0.6 ml water containing ^{18}F and the mixture shaken for about 10 min. By this procedure the activities on the resin beads could reach 450−1440 μCi depending on the concentration of ^{18}F in the solution.

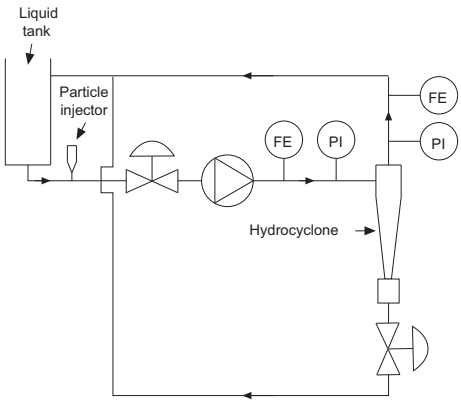

Fig. 1. The hydrocyclone in a circulating system.

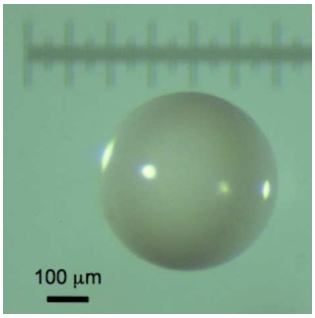

Fig. 2. The strong-base anion exchange resin bead used for these experiments.

2.3. The experimental process and conditions

The complete procedure of an experiment includes:

1. labeling the particles with the radioactive isotope,
2. starting the pump,
3. starting the PET scanner,
4. feeding the radioactive particle into the hydrocyclone rig,
5. locating the final position of the particle, and removing the particle.

In all experiments presented here, the inlet pressure is around 0.8 bar. The pump was started as least 30 s before the particle was injected in order to minimize start-up effects, allowing the flow to reach steady state. The Danckwerts mean residence time for the fluid in the cyclone is about a half second and in the circulating system excluding the cyclone is about 6 s for the present experiments, so that 30 s corresponds to more than four residence times, sufficient, in this single-phase system, to attain steady state in the cyclone.

The radioactive bead was then injected upstream of the pump. Calculated from the positions per millisecond (the positioning algorithm is described below), the particle velocity at the hydrocyclone inlet is around 10.55 m/s. At termination of the experiment, the final position of the bead was determined using a dosimeter. The bead could then be extracted from an outlet on the dust collection chamber. It was checked that the whole system was rid of radioactive objects before the next particle injection.

In the experiments, no air core was formed, since the entire recirculating system was completely filled with liquid and then sealed before operation. An air core may develop when the hydrocyclone is open to the atmosphere during operation such that the low pressure on the hydrocyclone axis causes air to be sucked into the cyclone body (Gupta et al., 2008). If an air core had been present in the system, bubbles would have been seen in the transparent particle collection chamber.

2.4. The scanner and data analysis

As being described above, when the nuclei of ^{18}F undergo positive beta decay, a positron is emitted. The positron annihilates with an electron in the vicinity of its original released place, resulting in a back-to-back emission of two gamma photons of 511 KeV each. The emitted photons are detected by a Positron Emission Tomography (PET) scanner (Siemens TruePoint) with an energy window of 425–650 keV. The scanner consists of three rings of diameter 855.2 mm. Each ring is composed of 48 sensor blocks, and each block has 13×13 lutetium oxyorthosilicate (LSO) scintillator crystals. The dimensions of the scintillation crystal sensors are $4 \times 4 \times 20$ mm. There is one crystal gap separating the blocks in the radial and axial directions (Panin et al., 2007). Each ring, including gaps, thus has 672 crystals (48×13 real crystals and 48 crystal gaps). In the axial direction, the number of crystals is 41 (3×13 real crystals and two crystal gaps), making the axial length of the field of view (FOV) 164 mm.

Two photons are considered to have emanated from one annihilation if they are detected by two sensors within a narrow time window, the so-called 'coincidence window', which is 4.5 ns for this scanner. The coincidence window has to be broad enough to receive almost all true back-to-back emissions, yet to be narrow enough to reject gamma-rays emitted from two annihilations close in time. The data generated from the PET scanner are stored in 'list-mode format'. The list-mode data contain two types of 64-bit words: event words and tag words. One type of tag words, namely timing words, is generated once per millisecond and is a counter of milliseconds. This, therefore, precisely determines the period between the millisecond points reported in this paper. Event words give the locations of the two sensors. By analyzing each event word, a 'line of response' (LOR) can be drawn between the two sensors.

Fig. 3 shows an example of LORs emanating from a point-like source recorded during a fraction of a millisecond. The crossing points, i.e. cutpoints are scattered for a number of reasons, which are discussed below and have to be averaged to obtain the position of the particle. This is done in 2-D in the plane shown in Fig. 3(a). Some false LORs are clearly visible in the image, mainly caused by the detection within the same coincidence window of two gamma photons emanating from two separate annihilations, where in both cases the other photon is not detected. Such events are termed as 'random coincidences'.

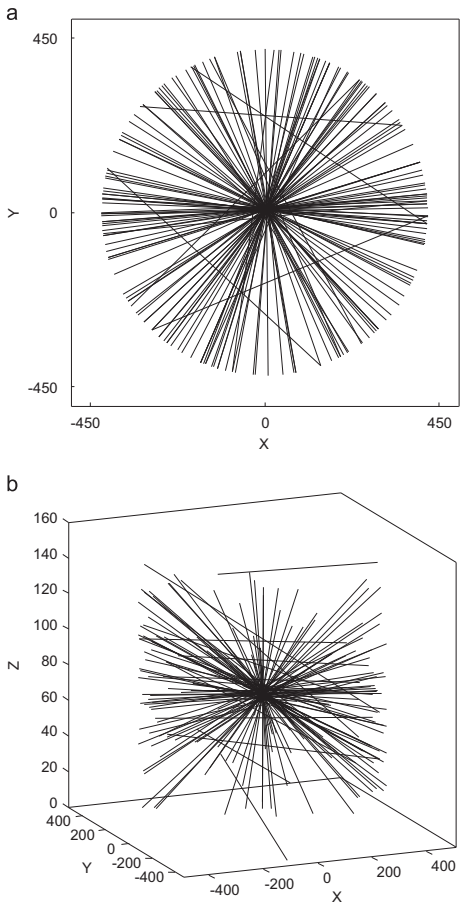

Fig. 3. LORs emanating from a point-like radioactive source during a fraction of a millisecond: (a) a two-dimensional view and (b) a three-dimensional view (z-axis expanded).

The algorithm developed to eliminate false cutpoints and subsequently, in a series of steps, narrow the spatial window containing the best cutpoints and averaging the remaining cutpoints to determine the particle position used by Hoffmann et al. (2005) was adapted and implemented in a Fortran program.

The program firstly reads in the list-mode data for calculating the coordinates of the two sensors. With the coordinates of the two points, the LORs and their 2-D cutpoints can be obtained. The average position of all the cutpoints is used as a preliminary reference point. Then the cutpoints farther than a specific distance from the preliminary average point are eliminated. The averaging and elimination of less good cutpoints are executed in turn a number of times until the spatial window has been narrowed to a few mm^2. A given LOR is eliminated from the analysis if it does not have at least one cutpoint in the current averaging window. Finally, the positions of the remaining cutpoints, i.e. the 'best' cutpoints, are averaged to determine the position of the particle centroid in the plane. The number of LORs, and therefore the number of cutpoints contributing to the final average, depends on the activity on the particle and also to an extent on the location of the particle in the field of view of the PET scanner.

The position of the particle in one of the planes orthogonal to the x–y plane is then determined by simple averaging of the cutpoints between the LORs remaining after the above elimination process.

3. Results and discussion

3.1. The effectiveness of the labeling method and the particle positioning algorithm

Initial measurements of a stationary particle were performed to assess the effectiveness of the labeling and the algorithm determining the particle position.

After the exclusion of out-of-range cutpoints are executed using the algorithm described above, the positions of the particle centroid once or more times per millisecond are determined from the remaining cutpoints falling within the final window with a radius of 4 mm. Analyzing 30-s data from a stationary particle in water, computing one position per millisecond, gives a standard deviation of particle positions of below 0.13 mm in both x and y directions, and below 0.17 mm in the z-direction, which confirms sufficient tracer activity and the effectiveness of the algorithm.

From this point on we will, for brevity, refer to the cutpoints falling within the final window, and therefore contributing to the final spatial average taken as the particle position, as the 'effective' cutpoints.

Fig. 4 shows that there is no significant drop in the number of effective cutpoints while the particle stays in water for 30 s. Compared to the particle residence time in this hydrocyclone, which is less than 3 s (see below), 30 s is a relatively long period. Fig. 4 confirms therefore that ^{18}F forms a stable bond with the particle by our labeling procedure and does not leach off into the water during the period. The activity applied to the particle material and the algorithm give more than 40 000 effective cutpoints per millisecond, ensuring a highly precise positioning of the particle (see below).

3.2. The extent and nature of uncertainty in particle positioning

The standard deviations of 1000 positions, i.e. 1-s data, in the three coordinates are plotted against time in Fig. 5. In this analysis there were about 140 000 effective cutpoints per millisecond.

In the x- and y-directions, the standard deviations in each second are below 0.13 mm. However, in the z-direction, i.e. the axial direction of the cylinder scanner, the uncertainty in the positions is somewhat higher (please note that the vertical axis starts at 0.1 mm), standard deviations being 0.15–0.17 mm. A difference was to be expected, since the x- and y-directions are exactly equivalent, while the detectors subtend a very limited angle to the particle in a plane containing the z-axis. That the standard deviations in consecutive seconds do not increase as the particle stays in water for 30 s again verifies the stable binding of ^{18}F to the particle.

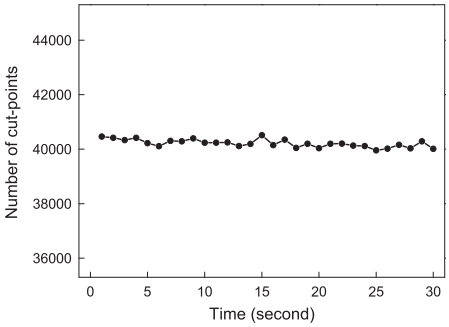

Fig. 4. Number of effective cutpoints as the particle stays in water for 30 s.

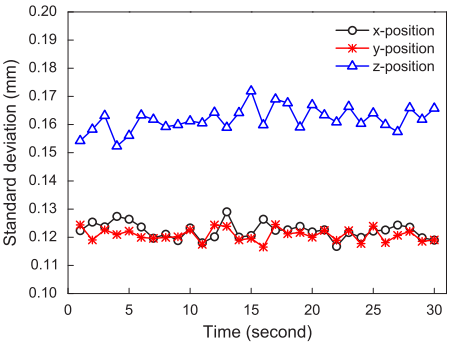

Fig. 5. Standard deviation of the position of the particle centroid as a function of time as the particle stays in water for 30 s.

To study further the scatter in the particle positions, the standard deviations in each coordinate direction obtained for stationary particles are investigated as a function of number of LORs as shown in Fig. 6. The number of LORs per millisecond varies, depending on the activities achieved on the particle. The standard deviations of z-positions are larger than those of x- and y-positions; the reason for this has been discussed above.

The scatter in the LORs and their cutpoints, and therefore in the particle positions, is caused by a number of effects:

1. The positrons emitted from ^{18}F travel a mean distance of 0.6 mm; a maximal distance of 2.4 mm in water before annihilating with electrons (Bailey, 2005).
2. The gamma-rays created from an annihilation are emitted in virtually opposite directions. However, the momenta of the

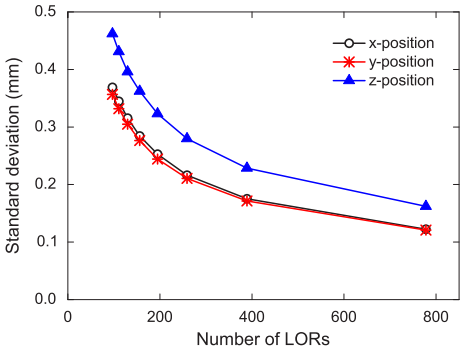

Fig. 6. Standard deviations of the particle positions in each direction as a function of number of LORs.

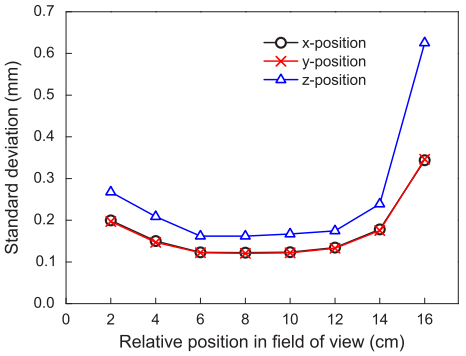

Fig. 7. Standard deviations of positions as a particle is located at a range of z-positions along the axis of the cylindrical scanner FOV.

electron and positron before the annihilation may cause the emission of two gamma photons deviating slightly from 180°.

3. The photon may interact with matter when traveling to the sensor, transferring part of its energy to an orbital electron and deflecting in a different angle (Compton scattering). Although the TruePoint PET scanner operates with an energy window between 425 and 650 keV to filter out signals from such events, some scatter-events with energies higher than the threshold of 425 keV may still be detected.
4. The finite size of the LSO crystal sensors limits the spatial resolution of the LORs, and therefore restrains the precision of cutpoints.
5. Photons penetrate a distance into the sensor crystal before detection. When the position of the source is far from the center of the FOV, the photons will hit the crystals at an angle. This may cause errors as photons may penetrate the material of the crystal that they first hit and be detected in a neighboring crystal. As a result, an LOR is wrongly drawn between the crystals detecting the photon rather than the crystal hit by the photon.

Fig. 6 shows that, as expected, the standard deviations decrease with the square-root of the number of LORs if the number of LORs are large enough for reasonable statistics.

As mentioned above, two photons being detected within the same coincidence window, but emanating from two separate annihilation events for both of which the other photon is not detected is termed as 'random coincidence'. The rate of random coincidences increases approximately with the square of the radioactivity. The ratio of the number of random coincidences to the number of real signals increases as the radioactive source moves closer to the edge of the FOV in the *z*-direction. The camera cannot identify random coincidences as such, but handles an algorithm that determines the *rate* of random coincidences. The elimination process in the positioning algorithm described above should get rid of almost all random coincidence events. Another effect of the source moving closer to the *z*-edge of the FOV is that the number of detected LORs becomes significantly reduced, resulting in a higher standard deviation in the particle positions as illustrated in Fig. 7.

We note at this point that since LORs are detected randomly in time, it is possible to split the millisecond in segments to obtain higher temporal resolutions at the cost of spatial resolution. In the present experiments a temporal resolution down to 0.2 ms was obtainable, and with a temporal resolution of 0.5 ms the spatial resolution was still very good.

3.3. Characterization of the particle

One has to be careful about using the classical cyclone separation models on this hydrocyclone with a rather unconventional design. Nevertheless, these models can give information about the approximate cut size of the cyclone. It was found that the present cyclone, under the conditions used, should have as cut size as a particle that in the field of gravity would settle in water with approximately 0.12 mm/s.

Measurements of the settling velocity of our tracer particles with sizes of 392−683 μm in the field of gravity showed a settling velocity of 7.8–11.1 mm/s. This confirms that the dynamically equivalent diameters of the tracer particles are much larger than the cut size of the hydrocyclone, and thus the particles should be separated out easily.

3.4. The trajectory of the particle

As the coordinates of the particle are determined using the above-mentioned algorithm, both the trajectory and animations of the moving particle can be rendered, allowing us to investigate the path of the particle in detail. Fig. 8 shows an example of a particle trajectory in the hydrocyclone. The temporal resolution, i.e. the time between adjacent points, is 1 ms. The particle moving from inlet to underflow outlet takes less than 3 s.

The animation of a moving particle shows that, rather than directly swirling through the cyclone from inlet to underflow chamber, the particle sometimes moves radially inward, reversing its axial flow direction and flowing toward the vortex finder rotating, as it does so, at a smaller radius and higher frequency. The particle seems to be swept into the inner, upward flowing, part of the vortex for a while, and later centrifuged outward to the downwardly directed vortex again.

In some sections of the cyclone, particular the lower part, where the trajectory traces can be seen to be denser in Fig. 8, the turn-back process even occurs more than 10 times.

While the animation cannot be shown here, Fig. 9 presenting a series of trajectories from 108 ms after the particle enters the hydrocyclone to 247 ms, shows a part of the process just described. In Fig. 9(b), the radius at which the particle rotates suddenly decreases and the particle, stopping its axial motion toward the particle outlet, rotates for several turns at nearly the same axial position. Subsequently, the particle regains the original radius and resumes its downward motion. However, the

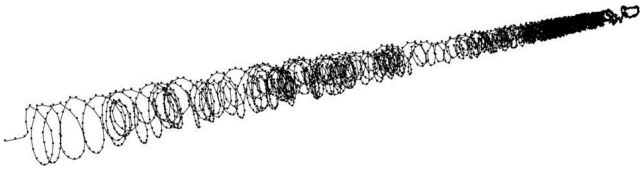

Fig. 8. The trajectory of a particle in a hydrocyclone, each point represents a particle position.

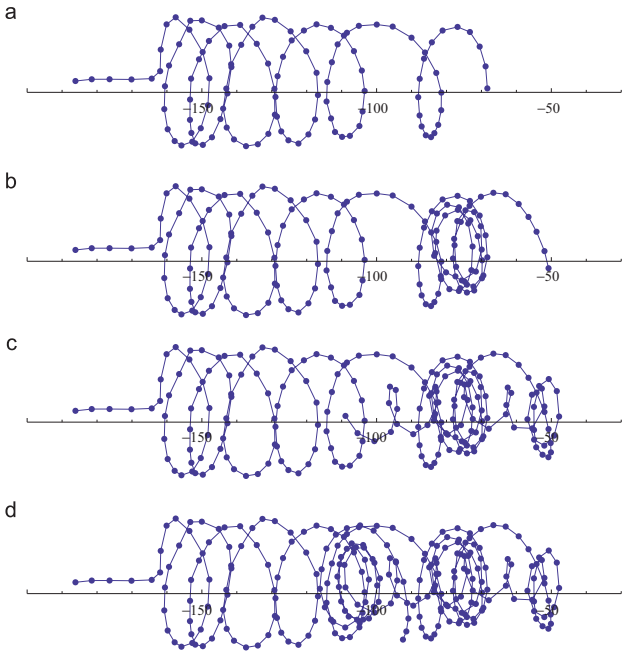

Fig. 9. The trajectory of a particle from (a) 108 ms to (d) 247 ms.

radius decreases again in Fig. 9(c), and this time it is pulled into the inner vortex and swirls upward a distance until once again being centrifuged to the outer vortex in Fig. 9(d).

Low in the conical section, the fluctuations in the swirling motion increase significantly and the motion appears almost disorganized at one axial position. Fig. 10 shows that the particle is experiencing a highly unstable motion while swirling closer to the dust outlet. It seems that the particle is trapped by the strongly turbulent flow at an axial position, moving irregularly for a period of time. After escaping from this area, the swirling motion is restored, but is much slower, which can be seen in the figure by the successive positions being much closer spaced below the 'trapping' position.

These unsteady sinuous flows and the axial flow reversals occur repeated in the section close to the dust outlet, resulting in an increase in residence time in this region. Fig. 11 shows the

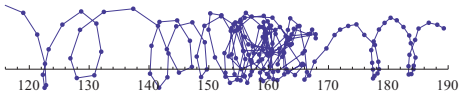

Fig. 10. The particle is trapped by the unsteady sinuous flow low in the hydrocyclone.

frequency of particle occurrence in various axial sections of the hydrocyclone, calculated from the millisecond particle positions. Fig. 11(b) and (c) is from different runs of experiments under the same condition. Fig. 11(a) is included for conveniently relating the *x* positions to the sections in the hydrocyclone. The frequency of appearance shows that the particles spends a considerable time in the bottom part of the hydrocyclone.

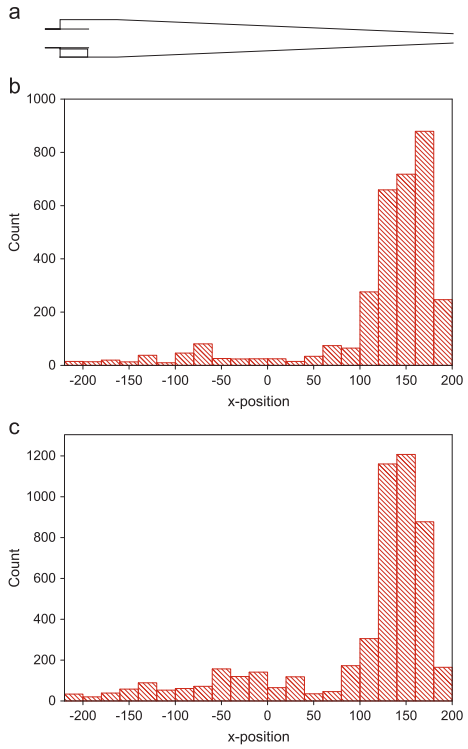

Fig. 11. The frequency of particle appearance in different sections of the hydrocyclone.

One relevant comment in this context is that the cyclone chosen here is quite long, and this may contribute to the irregularities of the flow in the apex region observed.

One possible reason accounting for the behavior of the particle in the lowest region of the hydrocyclone is the presence of the 'end of vortex phenomenon' there, something that significantly influences the behavior of cyclones, as described by Peng et al. (2005). The phenomenon is caused by the core of the vortex bending to the wall of the cyclone and rotating around the wall, resulting in a complicated flow pattern with two rotations: one around the core of the vortex and another of the core itself around the cyclone wall. Below the 'end of the vortex', which—if present—usually occurs at an axial position low in a reverse-flow cyclone separator, there is no primary vortex, but a secondary, much weaker, vortex, induced by the rotation of the core of the primary one, may be present. This secondary vortex may be visible in Fig. 10, where the particle can be seen to continue its spiraling path, but at a much reduced velocity, indicated by the millisecond positions being much more closely spaced. Below the end of the vortex the separation and the transport of the particles along the wall become ineffective.

The presence of the end of the vortex in the cyclone may be due to details of its design, for example the single inlet may cause the core of the vortex to precess more than it would have done if there was more than one tangential inlet. Also the widths of the vortex finder and the dust outlet, the length of the cone, the smoothness of the wall and the use of underflow from the cyclone will influence whether the end of the vortex is present or not. Although these first results thus only represent a few particle tracks, they have already shown many interesting features which could not have been seen by other techniques.

4. Conclusions

It has been shown that the technique of PEPT using modern PET cameras can be used to study high-speed flows with sufficient spatial and temporal resolution to reveal the details of the flow.

The temporal resolution in these measurements was 1 ms, which is also the frequency with which timing words are issued from the camera. However, since the LORs are detected randomly in time, it is possible to split up the millisecond in a number of segments to attain higher temporal resolutions. The present work showed that a temporal resolution down to 0.2 ms was obtainable.

The spatial resolution has been shown to be down to a fraction of a mm, the standard deviations in the positions of the centroid of the tracer particle being in the range 100−200 μm when the temporal resolution is 1 ms.

The flow of a particle in the hydrocyclone has been found to be less regular than expected, the particle taking excursions in the radial direction into the inner, upward flowing, vortex.

It is likely that the flow-instability seen low in the cyclone is due to the presence of the end of the vortex there, the irregular flow pattern of the particle at a given axial position and the much weaker vortex below this position being consistent with this assertion.

PEPT has proven an invaluable tool in understanding the flow in hydrocyclones and manipulating this by design, and a number of further research avenues will be pursued, involving changing the particle and fluid properties, the operational conditions and the geometry of the hydrocyclone.

Acknowledgments

The authors would like to thank Leif E. Sandnes from the University of Bergen and Dr. Tom C.H. Adamsen, Jan Salbu and Øyvind Steimler from the Centre for Nuclear Medicine at Haukeland University Hospital for help with the experimental setup and procedure. Also Dr. Michael E. Casey and William F. Jones from Siemens Molecular Imaging are appreciated for help with interpreting the list-mode data. The Petromaks program by the Norwegian Research Council and Aker Solutions are gratefully acknowledged for funding this work.

References

Bailey, D.L., 2005. Positron Emission Tomography: Basic Sciences. Springer.

Bamrungsri, P., Puprasert, C., Guigui, C., Marteil, P., Bréant, P., Hébrard, G., 2008. Development of a simple experimental method for the determination of the liquid field velocity in conical and cylindrical hydrocyclones. Chemical Engineering Research and Design 86 (11), 1263–1270.

Barigou, M., Chiti, F., Pianko-Oprych, P., Guida, A., Adams, L., Fan, X.F., Parker, D.J., Nienow, A.W., 2009. Using positron emission particle tracking (PEPT) to study mixing in stirred vessels: validation and tackling unsolved problems in opaque systems. Journal of Chemical Engineering of Japan 42 (11), 839–846.

Chan, C.W., Seville, J., Yang, Z.F., Baeyens, J., 2009. Particle motion in the CFB riser with special emphasis on PEPT-imaging of the bottom section. Powder Technology 196 (3), 318–325.

Cullivan, J., Williams, R., Cross, R., 2003. Understanding the hydrocyclone separator through computational fluid dynamics. Chemical Engineering Research and Design 81 (4), 455–466.

Depypere, F., Pieters, J.G., Dewettinck, K., 2009. PEPT visualisation of particle motion in a tapered fluidised bed coater. Journal of Food Engineering 93 (3), 324–336.

Ding, Y.L., Forster, R., Seville, J.P.K., Parker, D.J., 2002. Segregation of granular flow in the transverse plane of a rolling mode rotating drum. International Journal of Multiphase Flow 28 (4), 635–663.

Fan, X., Parker, D., Smith, M., 2006. Labelling a single particle for positron emission particle tracking using direct activation and ion-exchange techniques. Nuclear Instruments and Methods in Physics Research Section A: Accelerators, Spectrometers, Detectors and Associated Equipment 562 (1), 345–350.

Fisher, M.J., Flack, R.D., 2002. Velocity distributions in a hydrocyclone separator. Experiments in Fluids 32 (3), 302–312.

Fishwick, R., Winterbottom, M., Parker, D., Fan, X.F., Stitt, H., 2005a. The use of positron emission particle tracking in the study of multiphase stirred tank reactor hydrodynamics. Canadian Journal of Chemical Engineering 83 (1), 97–103.

Fishwick, R.P., Winterbottom, J.M., Parker, D.J., Fan, X.F., Stitt, E.H., 2005b. Hydrodynamic measurements of up- and down-pumping pitched-blade turbines in gassed, agitated, vessels using positron emission particle tracking. Industrial and Engineering Chemistry Research 44 (16), 6371–6380.

Griffiths, W.D., Beshay, Y., Parker, D.J., Fan, X., 2008. The determination of inclusion movement in steel castings by positron emission particle tracking (PEPT). Journal of Materials Science 43 (21), 6853–6856.

Griffiths, W.D., Parker, D.J., Fan, X., Hausard, M., 2010. Tracking inclusions in aluminium alloy castings using positron emission particle tracking (PEPT). Materials Science and Technology 26 (5), 528–533.

Gupta, R., Kaulaskar, M.D., Kumar, V., Sripriya, R., Meikap, B.C., Chakraborty, S., 2008. Studies on the understanding mechanism of air core and vortex formation in a hydrocyclone. Chemical Engineering Journal 144 (2), 153–166.

Hoffmann, A.C., Dechsiri, C., van de Wiel, F., Dehling, H., 2005. PET investigation of a fluidized particle: spatial and temporal resolution and short term motion. Measurement Science and Technology 16 (3), 851–858.

Hsieh, K.T., Rajamani, R.K., 1991. Mathematical model of the hydrocyclone based on physics of fluid flow. A.I.Ch.E. Journal 37 (5), 735–746.

Ingram, A., Hausard, M., Fan, X., Parker, D.J., Seville, J.P.K., Finn, N., Kilvington, R., Evans, M., 2007. Portable positron emission particle tracking (PEPT) for industrial use. In: Proceedings of 12th International Conference on Fluidization, pp. 13–17.

Ingram, A., Seville, J.P.K., Parker, D.J., Fan, X., Forster, R.G., 2005. Axial and radial dispersion in rolling mode rotating drums. Powder Technology 158 (1–3), 76–91.

Marins, L.P.M., Duarte, D.G., Loureiro, J.B.R., Moraes, C.A.C., Freire, A.P.S., 2010. LDA and PIV characterization of the flow in a hydrocyclone without an air-core. Journal of Petroleum Science and Engineering 70 (3–4), 168–176.

Monredon, T.C., Hsieh, K.T., Rajamani, R.K., 1992. Fluid flow model of the hydrocyclone: an investigation of device dimensions. International Journal of Mineral Processing 35 (1–2), 65–83.

Neesse, T., Donhauser, F., 2000. Advances in the theory and practice of hydrocyclone technique. In: Massacci, P. (Ed.), Proceedings of the XXI International Mineral Processing Congress, vol. 1. Elsevier, pp. A4-69.

Panin, V.Y., Chen, M., Michel, C., 2007. Simultaneous update iterative algorithm for variance reduction on random coincidences in PET. In: 2007 IEEE Nuclear Science Symposium Conference Record, pp. 2807–2811.

Parker, D.J., Dijkstra, A.E., Martin, T.W., Seville, J.P.K., 1997. Positron emission particle tracking studies of spherical particle motion in rotating drums. Chemical Engineering Science 52 (13), 2011–2022.

Peng, W., Hoffmann, A.C., Dries, H.W.A., Regelink, M.A., Stein, L.E., 2005. Experimental study of the vortex end in centrifugal separators: the nature of the vortex end. Chemical Engineering Science 60 (24), 6919–6928.

Pianko-Oprych, P., Nienow, A.W., Barigou, M., 2009. Positron emission particle tracking (PEPT) compared to particle image velocimetry (PIV) for studying the flow generated by a pitched-blade turbine in single phase and multi-phase systems. Chemical Engineering Science 64 (23), 4955–4968.

Schaafsma, S.H., Marx, T., Hoffmann, A.C., 2006. Investigation of the particle flowpattern and segregation in tapered fluidized bed granulators. Chemical Engineering Science 61 (14), 4467–4475.

Stairmand, C., 1951. The design and performance of cyclone separators. Transactions of the Institution of Chemical Engineers 29, 356–383.

Stellema, C.S., Vlek, J., Mudde, R.F., de Goeij, J.J.M., van de Bleek, C.M., 1998. Development of an improved positron emission particle tracking system. Nuclear Instruments and Methods in Physics Research Section A: Accelerators, Spectrometers, Detectors and Associated Equipment 404 (2–3), 334–348.

Wang, Z.-B., Chu, L.-Y., Chen, W.-M., Wang, S.-G., 2008. Experimental investigation of the motion trajectory of solid particles inside the hydrocyclone by a lagrange method. Chemical Engineering Journal 138 (1–3), 1–9.

Wildman, R.D., Blackburn, S., Benton, D.M., McNeil, P.A., Parker, D.J., 1999. Investigation of paste flow using positron emission particle tracking. Powder Technology 103 (3), 220–229.

Yang, I.H., Shin, C.B., Kim, T.H., Kim, S., 2004. A three-dimensional simulation of a hydrocyclone for the sludge separation in water purifying plants and comparison with experimental data. Minerals Engineering 17 (5), 637–641.

Paper II

II

6.2 Numerical study of the 'end of the vortex' phenomenon in a hydrocyclone separator

Yu-Fen Chang, Gleb I. Pisarev and Alex C. Hoffmann

AIP Conference Proceedings 1389, 1 (2011), 183–186

Numerical Study of the "End of the Vortex" Phenomenon in a Hydrocyclone Separator

Yu-Fen Chang, Gleb I. Pisarev, and Alex C. Hoffmann

Department of Physics and Technology, University of Bergen, Allegaten 55, 5007 Bergen, Norway

Abstract. The single-phase flow field in a hydrocyclone was studied numerically using the LES turbulence model. The hydrocyclone geometry and flow conditions are in accordance with previous experimental work. An important phenomenon in cyclone operation, the "end of the vortex," observed in experiments was reproduced in the simulations, where the vortex end deviated from the vortex axis and bent to the wall of the hydrocyclone body. As the vortex end attached to the wall, its rotation (precession) was visualized by monitoring the motion of the low-pressure spot caused by the vortex core on the wall.

Keywords: hydrocyclones, computational fluid dynamics, large eddy simulation, end of the vortex
PACS: 47.11.-j, 47.27.ep, 47.32.Ef.

INTRODUCTION

Reverse-flow cyclones have been used extensively for phase separations in a wide range of applications. The constructions of cyclones are fairly simple, generally categorized in two types: cylinder-on-cone design and swirl tubes [1]. The action of a cyclone is: The mixture enters the cyclone through the inlets which are constructed to cause the mixture to swirl along the inner wall and toward the dense phase outlet, i.e. the underflow outlet as shown in Figure 1 (a). The denser phase is flung onto the wall because of rotation and transported to the underflow outlet, while the lighter phase turns its axial direction, forming an inner vortex, and leaves the cyclone through the overflow outlet, also called the vortex finder. When the continuous phase is a liquid, cyclones are referred to as hydrocyclones, this is the focus of this study.

Despite their apparently simple construction, the flow fields inside are complex, so that significant research efforts have been focused on experimental and numerical studies of cyclones. However, limited by observation techniques, some detrimental phenomena, like the "end of the vortex" [1], are less studied. Recently particle tracks in a hydrocyclone were studied with high temporal and spatial resolutions [2] using the PEPT (positron emission particle tracking) technique, showing the likely presence of the "end of the vortex" and its strong effect on the particle flow. It is therefore desired to further investigate the flow pattern in this type of cyclone and to obtain a detailed understanding of this phenomenon. One approach to achieve this is computational fluid dynamics (CFD) simulations.

A number of CFD simulations have been performed to explore the capability of CFD in predicting the flow pattern, pressure drop, and separation efficiency of hydrocyclones of various geometries and under a range of operation conditions (see e.g. [3]), where one challenge is to employ a proper turbulence model to correctly mimic the effect of the turbulence in the strongly swirling, confined flows. For instance, the standard $k-\varepsilon$ turbulence model has been known to be unsuitable for highly swirling flows, giving velocity profiles in cyclones very different from those obtained in experiments. Hsieh and Rajamani [4] used a modified Prandtl mixing-length model to predict velocity profiles, which agree well with measurements using laser Doppler velocimetry (LDV).

The use of large eddy simulation (LES) turbulence model has been a break-through in CFD [5]. Based on space-filtered equations, LES solves the time-dependent Navier-Stokes equations for the mean flow and the largest eddies, while the effects of smaller eddies are modelled by using a relatively simple subgrid-scale (SGS) model, to a large extent avoiding the empiricism inherent in classical turbulence modelling. Previously, LES was considered too costly, but as computer hardware improves rapidly, LES is used increasingly. Lim et al. [6] studied the flow patterns in a hydrocyclone experimentally and computationally using particle image velocimetry (PIV) and LES turbulence model, respectively, showing good qualitative agreements between velocity vector fields. Recently, flow behaviours in gas swirl tubes were successfully simulated using LES, agreeing very well with experimental measurements [7].

In this present work, CFD simulations using LES were carried out to study the formation of the "end of the vortex" in a hydrocyclone as observed in experimental work of Chang et al. [2].

Numerical Analysis and Applied Mathematics ICNAAM 2011
AIP Conf. Proc. 1389, 183-186 (2011); doi: 10.1063/1.3636698

MODEL DESCRIPTION

CFD models were built to comply with the configuration of the hydrocyclone used in the above-mentioned PEPT experiments in Ref. [2]. Figure 1 (b) and (c) show the dimensions of the hydrocyclone and grid configuration. As pointed out by Derksen [8], in order to realistically model the flow in cyclones, the solid collection chamber needs to be included. "Trimmed mesh" was deployed, which generates a nearly regular mesh in the interior and a precisely fitting mesh at the walls. The dimension of a cubic cell was 1.2 mm. The total number of cells was 331745.

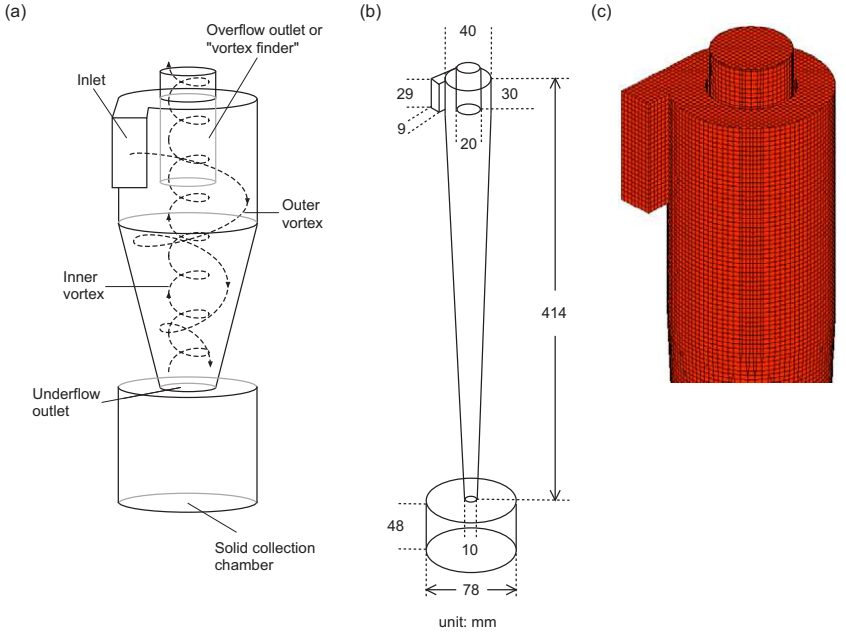

FIGURE 1. (a) Schematic cyclone separator with cylinder-on-cone design equipped with a solid collection chamber, (b) The hydrocyclone dimensions and (c) Grid configuration used in this study.

As mentioned, to simulate the highly complex, turbulent, swirling flow field in hydrocyclones, the turbulence model needs to be carefully chosen. Since LES in other work carried out by some of the present authors has proven to give results that are highly physically realistic and is able to supply values for turbulence properties that are difficult to measure, the LES turbulence model in combination with SGS model of Smagorinsky was applied in this study using the commercial CFD package Star-CD. Transient flow calculations have to be implemented. The MARS differencing scheme was applied. The SIMPLE algorithm with temporal discretization of three-time-level implicit was used.

The fluid in the hydrocyclone in the simulations was water, of which the properties were: density 997.561 kg/m^3, molecular weight 18 kg/kmol, and molecular viscosity 8.8871×10^{-4} kg/ms. The temperature was set 293 K.

The fluid velocities that had been used in the experimental work were prescribed at the inlet boundary. The initial condition was given as no-flow. In the experiments and the simulations, the only fluid outlet was the vortex finder. The no-slip condition was used on the wall boundary. Standard wall functions were used to handle the no-slip boundary condition at wall boundaries.

Mesh convergence tests using 775488 cells were carried out to assure the validity of solutions. The time-dependent static pressure distributions simulated under same conditions did not change significantly upon such mesh refinement.

RESULTS AND DISCUSSION

The "end of the vortex" refers to the vortex spontaneously ending at some point within the cyclone body [9]. As the phenomenon occurs, the vortex end attaches to the side wall and turns around. This is known as "vortex precession," since the orientation of the vortex axis is changing. In order to observe the vortex core, the cross-sectional static pressure distributions at an inlet fluid velocity of 4 m/s (volumetric flowrate of 3.76 m^3/hr) are displayed in Figure 2. It is obvious that the vortex core is already attached to the wall as it formed. Later on the vortex end descended, varying its axial position until gradually remaining around some steady level in the cyclone body.

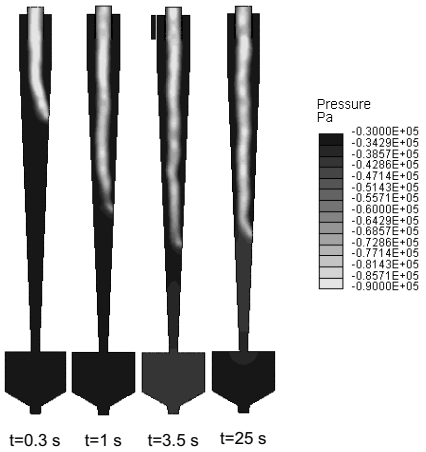

FIGURE 2. Cross-sectional contour plots of the static pressure simulated at an inlet flow rate of 4 m/s.

An important finding observed in Ref. [2] is that the tracer particle, after passing the "end of the vortex" region, continued its swirling motion, but at a much slower speed. The reason for this is that below the "end of the vortex" the particle flows in a much weaker, secondary vortex induced by the vortex core's rotation on the wall. The rotation of the vortex core is visualized in the simulations by extracting the pressure profiles on the wall as shown in Figure 3. The period of the rotation is estimated to be 14 ms, giving a frequency of 71.43 s^{-1}, which is confirmed in a long time series.

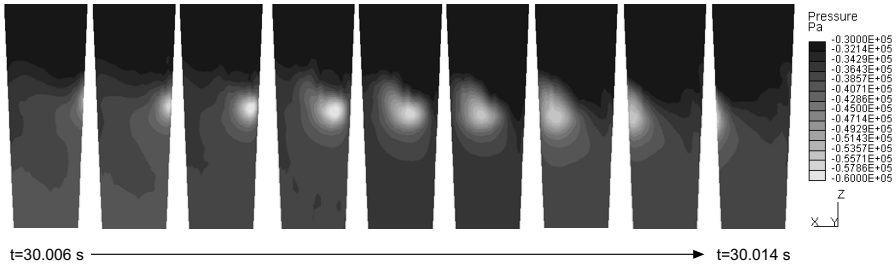

FIGURE 3. Profile plot for the pressure on the wall viewed from a fixed angle. From left to right: one graph per ms from 30.006 s to 30.014 s.

CONCLUSIONS

CFD simulations of a hydrocyclone using the LES turbulence model has been carried out to gain understanding of the "end of the vortex" phenomenon observed in experimental work of Chang et al. [2] using the PEPT technique. The numerically calculated static pressure distributions in the cross section show that the "end of the vortex" was successfully simulated, i.e. the vortex core bent from the hydrocyclone axis and attached to the wall. The axial position of attachment remained around some steady level after a few seconds of simulation. The vortex core's rotation around the inner wall was visualized and the rotation frequency was obtained by monitoring the pressure profile on the wall. The simulated flow field provides a reliable basis for further modelling of the motion of solid particles, even in the presence of the end of the vortex.

ACKNOWLEDGMENTS

The Petromaks program by the Norwegian Research Council and Aker Solutions are gratefully acknowledged for funding this work.

REFERENCES

1. A. C. Hoffmann, and L. E. Stein, *Gas cyclones and swirl tubes: principles, design and operation*, Springer, 2007.
2. Y.-F. Chang, C. G. Ilea, Ø. L. Aasen, and A. C. Hoffmann, *Chemical Engineering Science* **66**, 4203–4211 (2011).
3. A. F. Nowakowski, J. C. Cullivan, R. A. Williams, and T. Dyakowski, *Minerals Engineering* **17**, 661–669 (2004).
4. K. T. Hsieh, and R. K. Rajamani, *AIChE Journal* **37**, 735–746 (1991).
5. H. Versteeg, and W. Malalasekera, *An introduction to computational fluid dynamics: the finite volume method*, Pearson Education Ltd., 2007.
6. E. W. C. Lim, Y.-R. Chen, C.-H. Wang, and R.-M. Wu, *Chemical Engineering Science* **65**, 6415–6424 (2010).
7. G. I. Pisarev, V. Gjerde, B. V. Balakin, A. C. Hoffmann, H. A. Dijkstra, and W. Peng, *AIChE Journal* (in press).
8. J. J. Derksen, *AIChE Journal* **49**, 1359–1371 (2003).
9. W. Peng, A. C. Hoffmann, H. W. A. Dries, M. A. Regelink, and L. E. Stein, *Chemical Engineering Science* **60**, 6919–6928 (2005).

Paper V

6.5 PEPT: An invaluable tool for 3-D particle tracking and CFD simulation verification in hydrocyclone studies

Yu-Fen Chang, Tom C. H. Adamsen, Gleb I. Pisarev and Alex C. Hoffmann

European Physical Journal Web of Conferences 50 (2013), 05001p.1–p.8

V

EPJ Web of Conferences **50**, 05001 (2013)
DOI: 10.1051/epjconf/20135005001

PEPT: An invaluable tool for 3-D particle tracking and CFD simulation verification in hydrocyclone studies

Yu-Fen Chang[1,a], Tom C.H. Adamsen[2,3,b], Gleb I. Pisarev[1,c] and Alex C. Hoffmann[1,d]

[1] *University of Bergen, Department of Physics and Technology, Allegaten 55, 5007 Bergen, Norway*
[2] *Centre for Nuclear Medicine and PET, Department of Radiology, Haukeland University Hospital, Jonas Liesvei 65, 5021 Bergen, Norway*
[3] *University of Bergen, Department of Chemistry, Allegaten 41, 5007 Bergen, Norway*

Abstract. Particle tracks in a hydrocyclone generated both experimentally by positron emission particle tracking (PEPT) and numerically with Eulerian-Lagranian CFD have been studied and compared. A hydrocyclone with a cylinder-on-cone design was used in this study, the geometries used in the CFD simulations and in the experiments being identical. It is shown that it is possible to track a fast-moving particle in a hydrocyclone using PEPT with high temporal and spatial resolutions. The numerical 3-D particle trajectories were generated using the Large Eddy Simulation (LES) turbulence model for the fluid and Lagrangian particle tracking for the particles. The behaviors of the particles were analyzed in detail and were found to be consistent between experiments and CFD simulations. The tracks of the particles are discussed and related to the fluid flow field visualized in the CFD simulations using the cross-sectional static pressure distribution.

1. INTRODUCTION

1.1. Positron emission particle tracking (PEPT)

Positron emission particle tracking (PEPT), a technique to follow moving particles 3-dimensionally, has been applied to studies of flow systems and processes, e.g. fluidized bed (see, e.g., Ref. [1]), pharmaceutical coating process [2], casting process [3], and processing of solid-liquid food mixtures [4]. In addition to laboratory experiments, on-site particle tracking in a pressurized fluidized bed at BP's Hull Research and Technology Center using a portable PEPT camera was demonstrated by Ingram et al. [5]. Different phases can be tracked and studied, e.g. the flows of fluids can be visualized by following neutral density particles, i.e. particles having a similar density to the fluids. Due to the principle used, PEPT serves well in opaque and turbid systems.

PEPT employs the same principle as the medical imaging technique Positron Emission Tomography (PET). The differences lie in the nature of the tracked objects, the data processing and, as a consequence, the resolutions achievable. In PET the spatial distribution of a cloud of tracer is studied using image reconstruction techniques, while in PEPT a point-like tracer is located. PET needs enough counts for processing statistically meaningful histograms and images, whereas theoretically PEPT needs only few events for positioning the tracer. Therefore PEPT can achieve higher temporal and spatial resolution, for example Wildman et al. [6] achieved a temporal resolution of 2 ms with a spatial accuracy of about 1 mm. In this paper, we report particle tracking using a Siemens TruePoint PET camera and an in-house developed data-processing algorithm. A temporal resolution down to 1 ms is easily obtainable with a spatial resolution of 0.33 mm. Particle trajectories in a hydrocyclone are presented and compared with those obtained by CFD (computational fluid dynamics) simulation.

1.2. Hydrocyclone separator

With the main merits of simple construction, fairly high efficiency, and continuous operation capability, cyclones are extensively used for separation or classification of phases according to density, e.g. for gas-solid, liquid-solid, and liquid-liquid separations, where the cut-size requirement for the dispersed phase particles (bubbles, drops or solid particles) is down to a few μm [7,8]. Whenever the carrier phase is a liquid, they are referred to as hydrocyclones. Cyclones have two main types of geometries: swirl tubes and cylinder-on-cone designs. Varying in shape arrangement and operating conditions, hydrocyclones can be designed for liquid-liquid separation, e.g. de-oiling hydrocyclones, and liquid-solid separation, e.g. desanding hydrocyclone, the latter of which is the focus of this study.

In conventional cylinder-on-cone, tangential-inlet cyclones, the mixture enters the cyclone tangentially, forming the outer vortex, as shown in Figure 1. The mixture then swirls toward the bottom of the conical section. The denser phase, e.g. solid particles, experiencing a "centrifugal force", moves toward the wall and leaves the cyclone through the particle outlet (also called underflow outlet). The lighter phase moves toward the central axis, forming an "inner vortex", and leaves the cyclone through the vortex finder. The pressure drop and the separation efficiency for a given dynamically equivalent particle size, namely the collected mass over feed mass, are the most important concerns in the design and application of cyclones. The performance of cyclones is influenced by details of the flow behavior and the interaction between

[a] e-mail: yu-fen.chang@ift.uib.no
[b] e-mail: tom.christian.holm.adamsen@helse-bergen.no
[c] e-mail: gleb.pisarev@ift.uib.no
[d] e-mail: alex.hoffmann@ift.uib.no

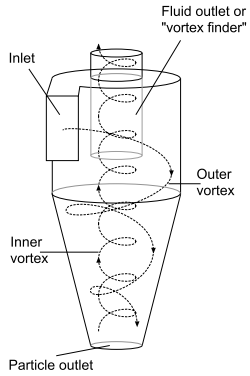

Figure 1. Cyclone separator with cylinder-on-cone design.

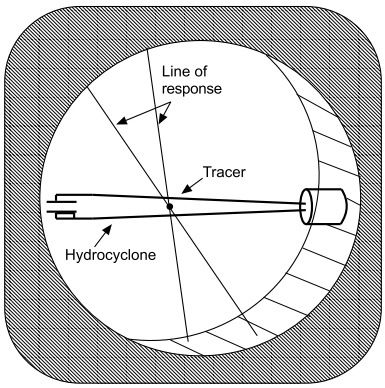

Figure 2. A schematic showing the hydrocyclone surrounded by gamma-ray sensors, the tracer, and the LORs.

different phases, which can be investigated by visualizing the trajectories of particles and fluid elements, the latter represented by neutral density particles. The trajectories of particles are helpful for understanding the separation process and potential problems, e.g. long residence time and clogging, as well as for instigating and verifying new and improved cyclone designs.

Experimentally, particle tracks in hydrocyclones have been acquired using optical setups. Knowles et al. [9] recorded 3-D positions of an anisole droplet acting as a neutral density tracer particle in a hydrocyclone using multi-directional cine-photography. Wang et al. [10] tracked a seed used as a tracer for the solid phase in a hydrocyclone two-dimensionally by means of a high-speed camera. These techniques have provided valuable flow patterns as functions of cyclone geometries and operation conditions, and elucidated efficiencies. However, how the flow behavior and consequently the separation efficiency are influenced by some special phenomena, e.g. the "end of the vortex" [11], often appearing in the complex, highly turbulent flows in cyclones, or some other cyclone-specific flow disturbance or feature is very difficult to observe. For this type of detailed information, techniques with higher temporal and spatial resolutions are required.

1.3. Particle tracking in hydrocyclones using CFD

CFD is increasingly applied for improving the design and separation efficiency of cyclones. Numerically, particles or fluid elements in hydrocyclones can be followed through space and time in a Lagrangian frame of reference. How the particle routes are affected by various parameters, e.g. particle size, entry point, and feed concentration, has been numerically studied using a variety of turbulence models (see, e.g., Ref. [12–15]). For example, Hsieh and Rajamani [12] simulated 2-D trajectories of limestone particles in a water hydrocyclone using Lagrangain particle tracking in a pre-calculated flow field. The CFD simulations of Cullivan et al. [14], based on a second-order-accurate pressure-strain Reynolds-stress turbulence model, showed particles being subjected to recirculatory paths in a hydrocyclone. Comparing trajectories obtained from various CFD models with experimental observations is important for examining the validity of the CFD models and understanding the experimental findings. In the present investigation, CFD models of a hydrocyclone were build to be consistent with the geometry used in PEPT experiments and the trajectories obtained in both are compared in detail.

2. EXPERIMENTAL

2.1. Positron emission particle tracking (PEPT)

The labelling and detection principle in PEPT are, as mentioned above, the same as that used in medical PET [16]. The tracers, which in PEPT are point-like, are labelled with isotopes containing surplus protons and undergoing positive beta decay, where a positron is emitted. After traveling a certain distance (less than 2.4 mm in water [16]), the positron annihilates with an electron, which causes the emission of two gamma photons of 511 keV each, heading in nearly 180-degree opposite directions. As these back-to-back emitted gamma photons are detected by two sensors, the tracer is known to be located somewhere along the line drawn between the sensors, referred to as the line of response (LOR). By cross-triangulation, the location of tracer can be estimated to be the cross-points, i.e. cutpoints (or points of closest proximity due to the scatter inherent in the process), of two or more LORs. Figure 2 schematically shows the gamma photons emanating from a tracer in a hydrocyclone and LORs are drawn between the locations of the detecting sensors.

To create a tracer particle strong base anion exchange resin beads "Amberlyst A26 Hydroxide Form" (Acros Organics) with sizes from 390 to 810 μm as shown in Figure 3 were immersed into the ^{18}F-contained water for about 10 minutes. ^{18}F ions are taken up through ion-exchange when the solution fills and covers the macroreticular, porous beads. In order to maximize the radioactivity on the tracer, the immersion time should

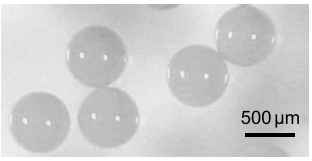

Figure 3. The strong base anion exchange resin beads used in these experiments.

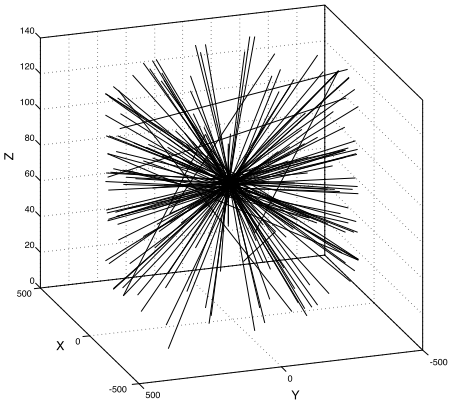

Figure 4. A 3-dimensional view of LORs emanating from a stationary resin bead during about 0.14 millisecond (z-direction expanded).

not exceed 25 minutes and the time between labelling and tracking experiments should be limited, considering the half life of ^{18}F of 109.8 minutes. By this procedure the radioactivity on a single resin bead could reach 450–1440 µCi depending on the concentration of ^{18}F in the solution and the size of the bead.

The gamma-ray sensor array used is a Siemens TruePoint PET scanner with an energy window of 425–650 keV and a coincidence window of 4.5 nanoseconds. The scanner consists of 39 rings of diameter 855.2 mm. Each ring contains 624 lutetium oxyorthosilicate (LSO) scintillation crystal sensors with dimensions of 4 mm × 4 mm × 20 mm. The coincidence window is a narrow time window intending to bracket two signals emitted from one annihilation event. Two photons detected within a coincidence window constitute one LOR. The data from the scanner, stored in "list-mode format", consist of event words, where the information of sensor location is stored. Between the event words, the scanner inserts periodic timing words every millisecond into the data stream. The position of the tracer every millisecond can be determined by finding the best average of the cutpoints of the numerous LORs. Figure 4 shows LORs from a stationary tracer during about 0.14 millisecond, with the z-direction being expanded. Some false LORs appear mainly because the scanner once in a while detects only one of the pair photons from each of two events that both take place within the same coincidence window. An algorithm developed by Hoffmann et al. [17] to eliminate the false cutpoints was tailored and implemented in a Fortran program for this present project.

The concept of the positioning algorithm is as follows [17]. The LOR cutpoints in the x-y-plane are considered first. The first estimation of the particle position in this plane is obtained by averaging the positions of all the cutpoints. Following this, the cutpoints farther than a certain distance from the first estimation are excluded from the next averaging. The process of excluding and averaging was executed several times with gradually shrinking spatial window each time. The diameter of the final spatial window is chosen to minimize the standard deviations of millisecond positions of a stationary tracer. A final window with a radius of 4–8 mm gives the lowest standard deviation, enclosing hundreds to tens of thousands cutpoints in a millisecond, depending on the radioactivity and the location of the particle in the field of view. The cutpoints used for final average, which is taken as the particle position, are referred to as "effective cutpoints".

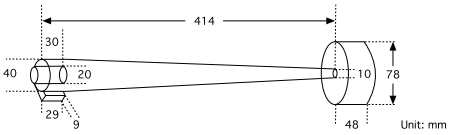

Figure 5. The dimensions of hydrocyclone used in this study.

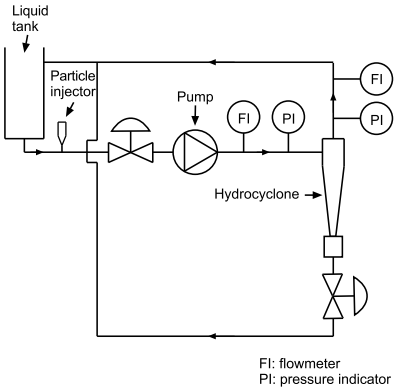

Figure 6. The hydrocyclone in a recirculation system.

2.2. The hydrocyclone and experimental rig

The hydrocyclone geometry used in the experiments and CFD simulations is designed to resemble the Stairmand high-efficiency cyclone [18] with a modified inlet and a prolonged cone. Connected with the particle outlet is a particle collection chamber. The dimensions are shown in Figure 5.

The hydrocyclone is incorporated in a flow loop as shown in Figure 6. The entire flow loop is filled with

liquid to avoid development of an air core in the cyclone. A centrifugal pump pushes the liquid, which is water in this study, through the hydrocyclone. After the liquid has been recirculated several times to minimise start-up effects, the radioactive particle is injected, using a syringe, upstream of the pump.

The settling velocity in water shows that the behavior of resin beads of 390–680 μm in the hydrocyclone corresponds to that of 90–115 μm particles with density of 2650 kg/m^3 (the density of sand). The dynamically equivalent diameters of the resin beads are larger than the cut-size of this hydrocyclone, and thus the resin beads are expected to be separated out.

3. CFD SIMULATION

To simulate the highly complex, turbulent, swirling flow field in cyclones, the turbulence model needs to be carefully chosen. The LES (large eddy simulation) turbulence model allows for explicit resolution of the large eddies in a calculation and implicitly accounting for the small eddies by using a subgrid-scale (SGS) model. Derksen et al. [19] used LES turbulence model and achieved a break-through in the simulation of a reverse-flow gas cyclone, reducing the empiricism involved in CFD and allowing modeling of the complex flow phenomena involved. Also, the LES turbulence model has been demonstrated to successfully simulate the transient flow pattern in confined strongly swirling flow in gas swirl tubes [20]. In this study, 3-D LES turbulence model in combination with the SGS model of Smagorinsky was applied using the commercial CFD package Star-CD. Considering the unsteady flow behavior, transient flow calculations have to be implemented. The MARS differencing scheme was applied. The SIMPLE algorithm with temporal discretization of three-time-level implicit was used.

The geometries of hydrocyclone used in experiments and CFD simulations were, as mentioned, identical. The fluid in the hydrocyclone in the simulations was water, of which the properties were: density 997.561 kg/m^3, molecular weight: 18 kg/kmol, and molecular viscosity 8.8871×10^{-4} kg/ms. The number of cells was 331745. Mesh convergence tests were carried out using 775488 cells to assure the validity of solutions. The static pressure distributions simulated under same conditions did not change significantly upon such mesh refinement.

The initial condition in the hydrocyclone was set as no-flow. The no-slip boundary condition was applied at wall boundaries. The initial fluid velocity was set at the cyclone inlet boundary. In the experiments and the simulations, the only fluid outlet was the vortex finder. The mass flow across the outlet conforms to overall continuity.

3-D particle trajectories were calculated using Lagrangian tracking. In Lagrangian particle tracking a particle is followed in the fluid flow field by integrating Newton's second law: $m(d\mathbf{v}/dt) = \sum \mathbf{F}$ with $\mathbf{v}$ the particle velocity, $\sum \mathbf{F}$ the forces acting on the particle due to the fluid or interaction with the wall of the cyclone and m the particle mass. The inlet flow rate, the particle diameter and density were chosen to be close to the experimental conditions.

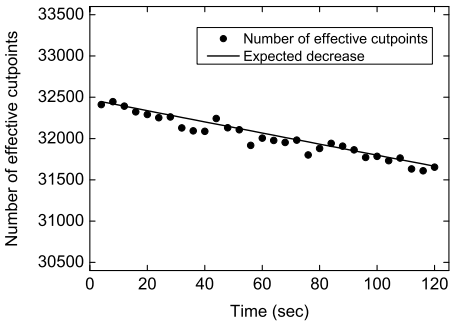

Figure 7. Number of effective cutpoints as the particle stays in water for 120 seconds.

4. RESULTS AND DISCUSSION

4.1. The performance of the labelling method and the particle positioning algorithm

Firstly it was necessary to verify whether the radioactivity would leach off the particle in the water. As the particle moves along with the liquid in the hydrocyclone, measuring the number of effective cutpoints of a moving particle in liquid is preferable. However, considering the number of detected cutpoints is also affected by the position in the field of view, a labelled, stationary resin bead surrounded by water and placed off the center of the field of view was tested. By applying the above-mentioned algorithm (see Sect. 2.1) with a final window of 8 mm to locate the particle, the number of effective cutpoints were found to decrease 3% after 120 s of residence in the water as plotted with dots in Figure 7. Considering the half-life and that the square of the number of cutpoints is proportional to the activity on the particle, the expected decrease can be calculated, plotted as a line in Figure 7. The comparison of measured and expected decrease in the number of cutpoints shows that the decrease is mainly due to the radioactive decay. 120 s is relatively long, since it takes less than 5 s for a tracer particle to traverse the cyclone (see below). Thus the activity on the particle is sufficiently stable during the process investigated in this study.

Although the effective cutpoints slightly decrease, the standard deviations of 4000 positions located once per millisecond do not increase in time during 120 s as shown in Figure 8. The positioning algorithm performs to the same precision during the entire period in spite of the slight decrease in effective cutpoints. Figures 7 and 8 show that when the particle is off the center of field of view (FOV) and with around 32000 effective cutpoints per ms, the standard deviation of less than 330 μm in three directions is achievable. With careful control on the labelling process, the number of effective cutpoint per ms can become as high as around 1.4×10^6, which gives a standard deviation in the particle position below 170 μm in three directions [21].

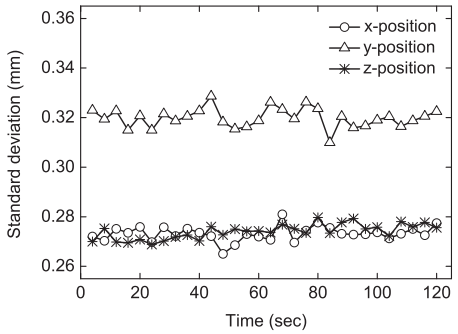

Figure 8. Standard deviation of the position of the particle centroid as a function of time as the particle stays in water for 120 seconds.

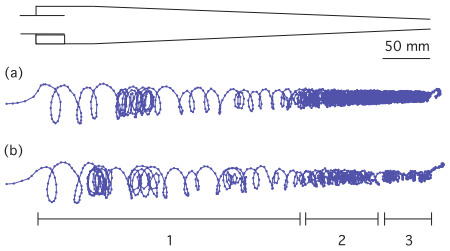

Figure 9. The trajectories of a particle in the hydrocyclone under the same operational condition obtained by PEPT. The numbers of effective cutpoints in each millisecond are in the order of 10^5 and 10^3 in (a) and (b), respectively. In (b) Savitzky-Golay filtering method has been applied on a series of 5 positions with a polynomial order of 2.

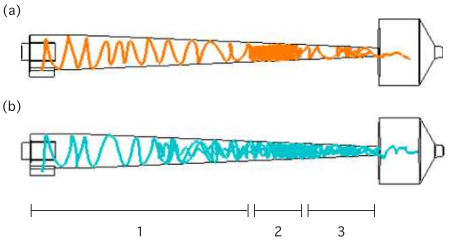

Figure 10. CFD simulated particle trajectory.

4.2. Particle trajectories in the hydrocyclone obtained by PEPT

The trajectory can be drawn after the positions were located once per millisecond, as dotted in Figure 9, using the above-mentioned algorithm. CFD simulated trajectories in Figure 10 have been placed under the experimentally obtained trajectories for convenient comparison (see below).

Figure 9(a) and (b) show the particle trajectories obtained under the same operational condition, where

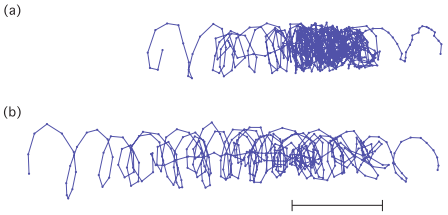

Figure 11. The particle's swirling motion is affected by a strongly turbulent flow down in the hydrocyclone. The bar underneath indicates the turbulent region.

Figure 12. The particle in Figure11(b) has passed the turbulent region and continues spiraling staggeringly.

the numbers of effective cutpoints in each millisecond in Figure 9(a) and (b) are in the order of 10^5 and 10^3, respectively. Figure 9(b) was obtained after applying Savitzky-Golay filtering method [22] using a series of 5 positions with a polynomial order of 2, which shows the capability of tracking a low-radioactive and off-centered (relatively in the FOV) particle by combining the positioning algorithm and Savitzky-Golay filtering method to filter out the positioning inaccuracy.

The track in Figure 9(a) seems denser than that in Figure 9(b). However, investigating the characteristics of the tracks shows identical behaviors. The particle flow in the hydrocyclone can be divided into three stages: In the first stage as approximately indicated below Figure 9, the particle's regular swirling motion toward the underflow outlet is clearly visible, except that in some short time intervals the particle appears to move into the inner, upward flowing vortex and reverses its axial direction, whereafter it is soon centrifuged outward to the downwardly directed vortex again.

In the second stage, when the particle reaches the lower part of the conical section the trajectory traces seem much denser. The particle spends a long time around a specific region. Following the particle in this section shows that the particle was affected by a strongly turbulent flow at a specific axial position as indicated below Figure 11, experiencing disorganized motion and being pulled into the inner vortex for several times. Figure 11(a) and (b) present this turbulent region of Figure 9(a) and (b), respectively. After escaping from the turbulent region, the particle regains its swirling motion, but moves and rotates much slower, indicated by the successive positions being much closer on the trajectory.

In the third stage, the particle, having passing the turbulent region the first time, continues its slower spiraling path and often loses its direction and spiral pattern as shown in Figure 12, which is the third stage of Figure 9(b). The third stage of the trajectory in Figure 9(a)

is not shown since the track is too dense so that no details can be seen. In the third stage of Figure 9(a) the particle swirls slowly, being frequently pulled into the inner vortex and in many times swirling upward to upstream of the turbulent section. Many times of the flow reversals and particle's experiencing the turbulent section make the track very dense. The axial flow reversals occur repeatedly, resulting in a long residence time in this region. As the particle spends such a long time swirling back and forth below and around the turbulent region, the separation and the transport of the particles along the wall will be ineffective in this region.

Similar phenomena were observed in all six experiments under the same conditions as those of Figure 9. The differences are in the number of times for which the particle was pulled into the inner vortex in stage 2 and stage 3, and the distance for which the particle flows upwardly. The residence time in six experiments therefore varied in the range of 0.8–4.8 s.

4.3. CFD simulations: Static pressure distribution and Lagrangian particle tracking

The 3-D particle trajectory shown in Figure 10 was generated using Lagrangian tracking in the fluid field calculated using the LES turbulence model. The particle shown here was injected at 6.7 sec after the beginning of the simulation. The simulated trajectories show very dense tracks in stage 2 as indicated in Figure 10. Magnification of these dense sections reveals similar phenomena to those found in experiments, e.g. disorganized tracks, the particle being pulled into the inner vortex, and slow and erratic transportation below this turbulent region.

The simulated static pressure distributions are presented below to help understand the root cause for this phenomenon.

Cross-sectional contour plots of static pressure at different simulation time for inlet velocity of 4 m/s are shown in Figure 13. As can be seen, the vortex core bends to the wall and rotates on the wall as it forms. Gradually, the vortex core swirls downward, but stops descending and rotates at some level above the underflow outlet. The cross-sectional static pressure distribution and the axial position of the core attachment did not change significantly after 5.5 sec of simulation. This phenomenon is known as the "end of the vortex" [11]. As the phenomenon occurs, three rotations appear in cyclone: one around the core of the vortex and another is the vortex core's rotating on the wall, which then induces a much weaker secondary vortex below the "end of the vortex".

The comparison and superposition of particle trajectory on the static pressure shows a strong correlation between the particle behaviors and the "end of the vortex". The trajectory in Figure 10(a) is further analyzed in Figure 14, where the particle was injected at a small radius. Figures 14(a) and (b) show that a dense track appears around the vortex core's axial position of attachment to the wall, which is indicated by an arrow in the graph. Figures 14(c) and (d) shows that the particle swirls close to the core-attached position, and then is dragged into the inner vortex, flowing upwardly. Such process occurs

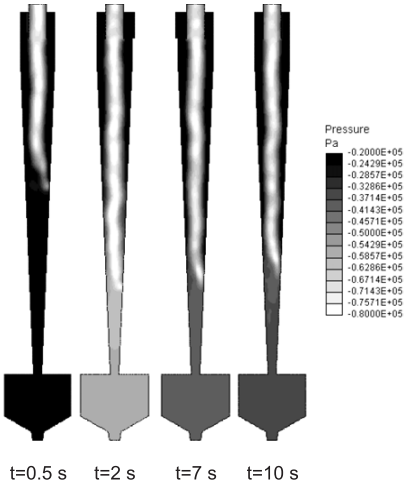

Figure 13. The cross-sectional contour plots of static pressure simulated at inlet velocity of 4 m/s.

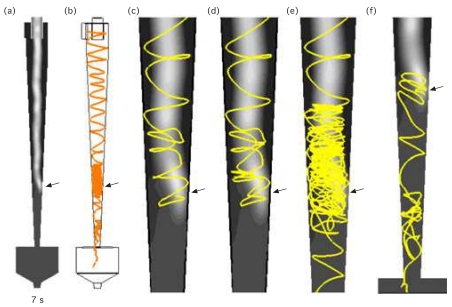

Figure 14. The correlation between the particle behavior and the "end of the vortex". The position on the wall where the vortex core bends and attaches is indicated by an arrow. (a) The contour plot of static pressure showing the core attached to the wall at the axial position of the "end of the vortex". (b) The whole particle track. (c)-(e) Detail showing the particle passing the "end of the vortex": The particle drawn into the upward inner vortex and centrifuged out again for several times. (f) The particle experiencing weak swirling and further axial flow reversals after escaping from the "end of the vortex".

several times, which causes the very dense track as shown in Figure 14(e). In Figure 14(f) the particle has left the "end of the vortex" region, transported in the induced, much weaker, secondary vortex, and occasionally runs arbitrarily, which resembles those found in the PEPT trajectory as shown in Figure 12.

Figure 15 presents the comparison and superposition of particle trajectory in Figure 10(b) on the static pressure. The particle was injected in the center of the inlet. In Figure 15(c) the particle suddenly loses its original swirling pace near and below the core-attached position, and in Figure 15(d) the particle trajectory from entering

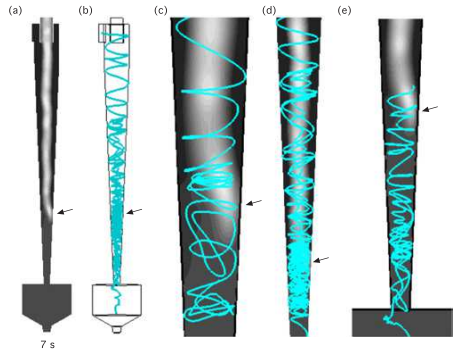

Figure 15. The correlation between the particle behavior and the "end of the vortex". The position on the wall where the vortex core bends and attaches is indicated by an arrow. (a) The contour plot of static pressure showing the core attached to the wall at the axial position of the "end of the vortex". (b) The whole particle track. (c)-(d) Detail showing the particle passing the "end of the vortex": The particle trapped by the "end of the vortex", moving at a disordered pace, drawn into the upward inner vortex, and centrifuged out again. (e) The particle experiencing weak swirling and further axial flow reversals after escaping from the "end of the vortex".

to leaving the "end of the vortex" region shows that the particle flow upwardly for a longer distance compared to Figure 14(e). After leaving the "end of the vortex" region, the particle flows upwardly a few times before finally entering the particle collection chamber, which corresponds to the particle behavior found in the third stage of the PEPT trajectory in Figure 9(a).

In the simulations of 120 particles, all the trajectories are obviously affected by the "end of the vortex" whether the particle is injected well within the inlet or close to the cyclone wall. The differences, resembling those in PEPT experiments, are in the number of times the particle is pulled into the inner vortex, and the distance that the particle flows upwardly each time. The residence time of the simulated particle in the hydrocyclone shown in Figure 14 and Figure 15 is approximately 1 sec. In the cases where more flow reversals take place, the residence times increase correspondingly.

These magnified sections together with the static pressure distribution show that the particle behaviors obtained by PEPT and CFD simulations are very similar, although the simulated "end of the vortex" position is higher than that observed in the experiments possibly because the wall friction has not been simulated precisely. As demonstrated by the CFD simulations, the "end of the vortex" phenomenon was found to be the likely cause for the irregular path of the particle in the lower section of the hydrocyclone.

5. CONCLUSION

In this study, particle tracking by the "PEPT" technique with high temporal and spatial resolutions has been accomplished and utilized to study the flows of particles in a hydrocyclone. Several interesting and unexpected events have been observed in the trajectory. The numerically calculated particle trajectories obtained by Lagrangian tracking in a LES simulated fluid field correspond to the experimental results very well. Further investigation into the simulated static pressure distributions reveals that the "end of the vortex" phenomenon caused the particle to flow irregularly and caused difficulties for the particle separation in the lower section of the hydrocyclone.

High precision PEPT has been demonstrated to be an invaluable tool for 3-D particle tracking and CFD simulation verification. Since solids, oil droplets, and gas bubbles may all be labelled, PEPT can be further developed for studying flows of various media in diverse processes.

The authors would like to thank the mechanical workshop at the University of Bergen and the Centre for Nuclear Medicine at Haukeland University Hospital for help with the experimental setup and procedure. Also Siemens Molecular Imaging is appreciated for help with interpreting the list-mode data. The Petromaks program by the Norwegian Research Council and Aker Solutions are acknowledged for funding this work. The Akademia program by Statoil is appreciated for funding the conference presentation.

References

[1] F. Depypere, J.G. Pieters, K. Dewettinck, Journal of Food Engineering **93**(3), 324 (2009)
[2] S. Fitzpatrick, Y. Ding, C. Seiler, C. Lovegrove, S. Booth, R. Forster, D. Parker, J. Seville, Pharmaceutical Technology pp. 70–78 (2003)
[3] W.D. Griffiths, D.J. Parker, X. Fan, M. Hausard, Materials Science and Technology **26**(5), 528 (2010)
[4] P.G. Fairhurst, M. Barigou, P.J. Fryer, J.P. Pain, D.J. Parker, International Journal of Multiphase Flow **27**(11), 1881 (2001)
[5] A. Ingram, M. Hausard, X. Fan, D.J. Parker, J.P.K. Seville, N. Finn, R. Kilvington, M. Evans, *Portable Positron Emission Particle Tracking (PEPT) for Industrial Use*, in *Proceedings of 12th International Conference on Fluidization* (2007), pp. 13–17
[6] R.D. Wildman, J.M. Huntley, D.J. Parker, Physical Review Letters **86**(15), 3304 (2001)
[7] A.C. Hoffmann, L.E. Stein, *Gas cyclones and swirl tubes: principles, design and operation* (Springer, 2007), ISBN 3-540-43326-0
[8] L. Svarovsky, M.T. Thew, eds., *Hydrocyclones: analysis and applications* (Kluwer Academic Publishers, Boston, 1992), ISBN 0-7923-1876-5
[9] S.R. Knowles, D.R. Woods, I.A. Feuerstein, The Canadian Journal of Chemical Engineering **51**(3), 263 (1973)
[10] Z.B. Wang, L.Y. Chu, W.M. Chen, S.G. Wang, Chemical Engineering Journal **138**(1-3), 1 (2008)
[11] W. Peng, A.C. Hoffmann, H.W.A. Dries, M.A. Regelink, L.E. Stein, Chemical Engineering Science **60**(24), 6919 (2005)

[12] K.T. Hsieh, R.K. Rajamani, AIChE Journal **37**(5), 735 (1991)
[13] T. Neesse, F. Donhauser, *Advances in the theory and practice of hydrocyclone technique*, in *Proceedings of the XXI International Mineral Processing Congress*, edited by P. Massacci (Elsevier, 2000), pp. A4-69–A4-76
[14] J. Cullivan, R. Williams, R. Cross, Chemical Engineering Research and Design **81**(4), 455 (2003)
[15] I.H. Yang, C.B. Shin, T.H. Kim, S. Kim, Minerals Engineering **17**(5), 637 (2004)
[16] D.L. Bailey, D.W. Townsend, P.E. Valk, M.N. Maisey, eds., *Positron emission tomography: basic sciences* (Springer, 2005), ISBN 1-85233-798-2
[17] A.C. Hoffmann, C. Dechsiri, F. van de Wiel, H. Dehling, Measurement Science and Technology **16**(3), 851 (2005)
[18] C. Stairmand, Transactions of the Institution of Chemical Engineers **29**, 356 (1951)
[19] J.J. Derksen, H.E.A. Van den Akker, AIChE Journal **46**(7), 1317 (2000)
[20] G.I. Pisarev, A.C. Hoffmann, W. Peng, H.A. Dijkstra, Applied Mathematics and Computation **217**(11), 5016 (2011)
[21] Y.-F. Chang, C.G. Ilea, Ø.L. Aasen, A.C. Hoffmann, Chemical engineering Science **66**(18), 4203 (2011)
[22] A. Savitzky, M.J.E. Golay, Analytical Chemistry **36**(8),1627 (1964)

Bibliography

[1] A. C. Hoffmann and L. E. Stein. *Gas cyclones and swirl tubes: principles, design and operation*. Springer, 2007.

[2] M. W. Mikhail, A. I. A. Salama, and R. Burns. Fine particles removal from oil sand tailings by hydrocyclone. *CIM bulletin*, 90(1015):86–90, 1997.

[3] W. Barth. Berechnung und auslegung von zyklonabscheidern auf grund neuerer untersuchungen. *Brennstoff-Wärme-Kraft*, 8(1):1–9, 1956.

[4] F. A. Zenz. Cyclone — design tips. *Chemical Engineering*, pages 60–64, 2001.

[5] K. Rietema. Het mechanisme van de afscheiding van fijnverdeelde stoffen in cyclonen. *De Ingenieur*, 71 jaargang(39):ch59–ch65, 1959.

[6] W. Peng, A. C. Hoffmann, H. W. A. Dries, M. Regelink, and K.-K. Foo. Neutrally buoyant tracer in gas cleaning equipment: a case study. *Measurement Science and Technology*, 16(12):2405–2414, 2005.

[7] C. W. Chan, J. P. K. Seville, X. F. Fan, and J. Baeyens. Particle motion in CFB cyclones as observed by positron emission particle tracking. *Industrial and Engineering Chemistry Research*, 48(1):253–261, 2009.

[8] Z.-B. Wang, L.-Y. Chu, W.-M. Chen, and S.-G. Wang. Experimental investigation of the motion trajectory of solid particles inside the hydrocyclone by a Lagrange method. *Chemical Engineering Journal*, 138(1-3):1–9, 2008.

[9] A. Horvath, C. Jordan, and M. Harasek. Influence of vortex-finder diameter on axial gas flow in simple cyclone. *Chemical Product and Process Modeling*, 3(1):1–26, 2008.

[10] H. Shalaby, K. Pachler, K. Wozniak, and G. Wozniak. Comparative study of the continuous phase flow in a cyclone separator using different turbulence models. *International journal for numerical methods in fluids*, 48(11):1175–1197, 2005.

[11] M. Narasimha, M. Brennan, and P. Holtham. A review of CFD modelling for performance predictions of hydrocyclone. *Engineering Applications of Computational Fluid Mechanics*, 1(2):109–125, 2007.

[12] K. T. Hsieh and R. K. Rajamani. Mathematical model of the hydrocyclone based on physics of fluid flow. *AIChE Journal*, 37(5):735–746, 1991.

[13] T. Olson and R. V. Ommen. Optimizing hydrocyclone design using advanced CFD model. *Minerals Engineering*, 17(5):713–720, 2004. Hydrocyclones '03.

[14] S. Bernardo, M. Mori, A. P. Peres, and R. P. Dionísio. 3-D computational fluid dynamics for gas and gas-particle flows in a cyclone with different inlet section angles. *Powder Technology*, 162(3):190–200, 2006.

[15] S. K. Shukla, P. Shukla, and P. Ghosh. Evaluation of numerical schemes for dispersed phase modeling of cyclone separators. *Engineering Applications of Computational Fluid Mechanics*, 5(2):235–246, 2011.

[16] G. I. Pisarev and A. C. Hoffmann. Effect of the "end of the vortex" phenomenon on the particle motion and separation in a swirl tube separator. *Powder Technology*, 222:101–107, 2012.

[17] O. Storch and K. Pojar. Die problematik des verschleißes von fliehkraftabscheidern. *Staub Reinhalt. Luft*, 30(12):501–506, 1970.

[18] A. C. Hoffmann, R. de Jonge, H. Arends, and C. Hanrats. Evidence of the 'natural vortex length' and its effect on the separation efficiency of gas cyclones. *Filtration & Separation*, 32(8):799–804, 1995.

[19] R. M. Alexander. Fundamentals of cyclone design and operation. *Proceedings of the Australasian Institute of Mining and Metallurgy*, 152-153:203–228, 1949.

[20] A. C. Hoffmann, M. de Groot, W. Peng, H. W. A. Dries, and J. Kater. Advantages and risks in increasing cyclone separator length. *AIChE Journal*, 47(11):2452–2460, 2001.

[21] A. C. Hoffmann, W. Peng, H. Dries, M. Regelink, and K.-K. Foo. Effect of pressure recovery vanes on the performance of a swirl tube, with emphasis on the flow pattern and separation efficiency. *Energy & Fuels*, 20(4):1691–1697, 2006.

[22] W. Peng, A. C. Hoffmann, H. W. A. Dries, M. A. Regelink, and L. E. Stein. Experimental study of the vortex end in centrifugal separators: The nature of the vortex end. *Chemical Engineering Science*, 60(24):6919–6928, 2005.

[23] W. Peng, A. C. Hoffmann, H. Dries, M. Regelink, and K.-K. Foo. Reverse-flow centrifugal separators in parallel: performance and flow pattern. *AIChE Journal*, 53(3):589–597, 2007.

[24] W. Peng, D. Christensen, S. Jacobsson, E. Kvinnesland, and A. C. Hoffmann. Studies of the flow in and around gas dedusters and demisters using neutrally buoyant tracer. *Chemical Engineering Journal*, 158(1):11–18, 2010.

[25] J. Abrahamsen and R. W. K. Allen. The efficiency of conventional return-flow cyclones at high temperatures. *IChemE Symposium Series*, 99:31–43, 1986.

[26] E. A. Elsayed, R. A. Medronho, R. Wagner, and W. D. Deckwer. Use of hydrocyclones for mammalian cell retention: separation efficiency and cell viability (part 1). *Engineering in Life Sciences*, 6(4):347–354, 2006.

[27] I. C. Bicalho, J. Mognon, J. Shimoyama, C. H. Ataíde, and C. R. Duarte. Separation of yeast from alcoholic fermentation in small hydrocyclones. *Separation and Purification Technology*, 87:62–70, 2012.

[28] A. A. Pinto, I. C. Bicalho, J. Mognon, C. R. Duarte, and C. H. Ataíde. Separation of Saccharomyces cerevisiae from alcoholic fermentation broth by two commercial hydrocyclones. *Separation and Purification Technology*, 120:69–77, 2013.

[29] D. L. Bailey. *Positron emission tomography: basic sciences*. Springer, 2005.

[30] M. Hawkesworth, M. O'Dwyer, J. Walker, P. Fowles, J. Heritage, P. Stewart, R. Witcomb, J. Bateman, J. Connolly, and R. Stephenson. A positron camera for industrial application. *Nuclear Instruments and Methods in Physics Research Section A: Accelerators, Spectrometers, Detectors and Associated Equipment*, 253 (1):145–157, 1986.

[31] P. A. E. Stewart, J. D. Rogers, R. T. Skelton, P. L. Salter, M. J. Allen, R. Parker, P. Davis, P. Fowles, M. R. Hawkesworth, M. A. O'Dwyer, J. Walker, and R. Stephenson. Positron emission tomography — a new technique for observing fluid behaviour in engineering systems. In J. M. Farley and R. W. Nichols, editors, *Non-Destructive Testing*, pages 2718–2726. Pergamon, 1988.

[32] M. R. Hawkesworth, D. J. Parker, P. Fowles, J. F. Crilly, N. L. Jefferies, and G. Jonkers. Nonmedical applications of a positron camera. *Nuclear Instruments and Methods in Physics Research Section A: Accelerators, Spectrometers, Detectors and Associated Equipment*, 310(1–2):423–434, 1991.

[33] E. A. van den Bergen, G. Jonkers, K. Strijckmans, and P. Goethals. Industrial applications of positron emission computed tomography. *The International Journal of Radiation Applications and Instrumentation (Part E)*, 3(4):407–418, 1989.

[34] D. Gilling, N. L. Jefferies, P. Fowles, M. R. Hawkesworth, and D. J. Parker. The application of positron emission tomography to the study of mass transfer in fractured rocks. In *Symposium P – Scientific Basis for Nuclear Waste Management XIV*, volume 212 of *MRS Online Proceedings Library*, 1990.

[35] D. J. Parker, T. W. Leadbeater, X. Fan, M. N. Hausard, A. Ingram, and Z. Yang. Positron imaging techniques for process engineering: recent developments at Birmingham. *Measurement Science and Technology*, 19(9):094004, 2008.

[36] C. Dechsiri, E. A. van der Zwan, H. G. Dehling, and A. C. Hoffmann. Dispersion of particle pulses in fluidized beds measured by positron emission tomography. *AIChE Journal*, 51(3):791–801, 2005.

[37] M. Bourgoin, N. T. Ouellette, H. Xu, J. Berg, and E. Bodenschatz. The role of pair dispersion in turbulent flow. *Science*, 311(5762):835–838, 2006.

[38] Y. Gasteuil, W. L. Shew, M. Gibert, F. Chillá, B. Castaing, and J. F. Pinton. Lagrangian temperature, velocity, and local heat flux measurement in Rayleigh-Bénard convection. *Physical Review Letters*, 99(23):234302–1–234302–4, 2007.

[39] W. L. Shew, Y. Gasteuil, M. Gibert, P. Metz, and J.-F. Pinton. Instrumented tracer for Lagrangian measurements in Rayleigh-Bénard convection. *Review of Scientific Instruments*, 78(6):065105, 2007.

[40] G. A. Voth, A. La Porta, A. M. Crawford, E. Bodenschatz, C. Ward, and J. Alexander. A silicon strip detector system for high resolution particle tracking in turbulence. *Review of scientific instruments*, 72(12):4348–4353, 2001.

[41] A. La Porta, G. A. Voth, A. M. Crawford, J. Alexander, and E. Bodenschatz. Fluid particle accelerations in fully developed turbulence. *Nature*, 409(6823):1017–1019, 2001.

[42] G. Field, J. Bridgwater, T. Beynon, and J. Botterill. Mechanics of powder mixing using positron emission tomography. *Nuclear Instruments and Methods in Physics Research Section A: Accelerators, Spectrometers, Detectors and Associated Equipment*, 310(1–2):435–436, 1991.

[43] D. J. Parker, A. E. Dijkstra, T. W. Martin, and J. P. K. Seville. Positron emission particle tracking studies of spherical particle motion in rotating drums. *Chemical Engineering Science*, 52(13):2011–2022, 1997.

[44] Y. L. Ding, R. Forster, J. P. K. Seville, and D. J. Parker. Segregation of granular flow in the transverse plane of a rolling mode rotating drum. *International Journal of Multiphase Flow*, 28(4):635–663, 2002.

[45] A. Ingram, J. P. K. Seville, D. J. Parker, X. Fan, and R. G. Forster. Axial and radial dispersion in rolling mode rotating drums. *Powder Technology*, 158(1-3): 76–91, 2005.

[46] J. Bridgwater, C. J. Broadbent, and D. J. Parker. Study of the influence of blade speed on the performance of a powder mixer using positron emission particle tracking. *Chemical Engineering Research & Design*, 71(A6):675–681, 1993.

[47] J. Jones and J. Bridgwater. A case study of particle mixing in a ploughshare mixer using positron emission particle tracking. *International Journal of Mineral Processing*, 53(1):29–38, 1998.

[48] B. Laurent and J. Bridgwater. Continuous mixing of solids. *Chemical Engineering & Technology*, 23(1):16–18, 2000.

[49] Y. S. Fangary, M. Barigou, J. P. K. Seville, and D. J. Parker. Fluid trajectories in a stirred vessel of non-newtonian liquid using positron emission particle tracking. *Chemical Engineering Science*, 55(24):5969–5979, 2000.

[50] H. P. Kuo, P. C. Knight, D. J. Parker, A. S. Burbidge, M. J. Adams, and J. P. K. Seville. Non-equilibrium particle motion in the vicinity of a single blade. *Powder technology*, 132(1):1–9, 2003.

[51] P. M. Portillo, A. U. Vanarase, A. Ingram, J. K. Seville, M. G. Ierapetritou, and F. J. Muzzio. Investigation of the effect of impeller rotation rate, powder flow rate, and cohesion on powder flow behavior in a continuous blender using PEPT. *Chemical Engineering Science*, 65(21):5658–5668, 2010.

[52] F. F. Snieders, A. C. Hoffmann, D. Cheesman, J. G. Yates, M. Stein, and J. P. K. Seville. The dynamics of large particles in a four-compartment interconnected fluidized bed. *Powder Technology*, 101(3):229–239, 1999.

[53] B. P. B. Hoomans, J. A. M. Kuipers, M. A. M. Salleh, M. Stein, and J. P. K. Seville. Experimental validation of granular dynamics simulations of gas-fluidised beds with homogenous in-flow conditions using positron emission particle tracking. *Powder Technology*, 116(2-3):166–177, 2001.

[54] S. H. Schaafsma, T. Marx, and A. C. Hoffmann. Investigation of the particle flowpattern and segregation in tapered fluidized bed granulators. *Chemical Engineering Science*, 61(14):4467–4475, 2006.

[55] R. D. Wildman, S. Blackburn, D. M. Benton, P. A. McNeil, and D. J. Parker. Investigation of paste flow using positron emission particle tracking. *Powder Technology*, 103(3):220–229, 1999.

[56] J. Conway-Baker, R. W. Barley, R. A. Williams, X. Jia, J. Kostuch, B. McLoughlin, and D. J. Parker. Measurement of the motion of grinding media in a vertically stirred mill using positron emission particle tracking (PEPT). *Minerals engineering*, 15(1): 53–59, 2002.

[57] Y. S. Fangary, M. Barigou, J. P. Seville, and D. J. Parker. A langrangian study of solids suspension in a stirred vessel by positron emission particle tracking (PEPT). *Chemical engineering & technology*, 25(5):521–528, 2002.

[58] R. P. Fishwick, J. M. Winterbottom, D. J. Parker, X. F. Fan, and E. H. Stitt. Hydrodynamic measurements of up- and down-pumping pitched-blade turbines in gassed, agitated vessels, using positron emission particle tracking. *Industrial and Engineering Chemistry Research*, 44(16):6371–6380, 2005.

[59] S. Fitzpatrick, Y. Ding, C. Seiler, C. Lovegrove, S. Booth, R. Forster, D. J. Parker, and J. Seville. Positron emission particle tracking studies of a Wurster process for coating applications. *Pharmaceutical Technology*, pages 70–78, 2003.

[60] P. W. Cox, S. Bakalis, H. Ismail, R. Forster, D. J. Parker, and P. J. Fryer. Visualisation of three-dimensional flows in rotating cans using positron emission particle tracking (PEPT). *Journal of Food Engineering*, 60(3):229–240, 2003.

[61] R. Fishwick, M. Winterbottom, D. Parker, X. Fan, and H. Stitt. The use of positron emission particle tracking in the study of multiphase stirred tank reactor hydrodynamics. *Canadian Journal of Chemical Engineering*, 83(1):97–103, 2005.

[62] W. D. Griffiths, Y. Beshay, D. J. Parker, and X. Fan. The determination of inclusion movement in steel castings by positron emission particle tracking (PEPT). *Journal of Materials Science*, 43(21):6853–6856, 2008.

[63] W. D. Griffiths, Y. Beshay, D. J. Parker, X. Fan, and M. Hausard. The application of positron emission particle tracking (PEPT) to study the movement of inclusions in shape castings. In J. Campbell, P. N. Crepeau, and M. Tiryakioglu, editors, *Shape Casting: 3rd International Symposium 2009*, pages 231–238, 2009.

[64] W. D. Griffiths, D. J. Parker, X. Fan, and M. Hausard. Tracking inclusions in aluminium alloy castings using positron emission particle tracking (PEPT). *Materials Science and Technology*, 26(5):528–533, 2010.

[65] C. W. Chan, J. Seville, X. Fan, and J. Baeyens. Solid particle motion in a standpipe as observed by positron emission particle tracking. *Powder Technology*, 194(1):58–66, 2009.

[66] P. G. Fairhurst, M. Barigou, P. J. Fryer, J.-P. Pain, and D. J. Parker. Using positron emission particle tracking (PEPT) to study nearly neutrally buoyant particles in high solid fraction pipe flow. *International Journal of Multiphase Flow*, 27(11): 1881–1901, 2001.

[67] C. W. Chan, J. Seville, X. Fan, and J. Baeyens. Particle motion in L-valve as observed by positron emission particle tracking. *Powder Technology*, 193(2):137–149, 2009.

[68] K. T. Lee, A. Ingram, and N. A. Rowson. Twin screw wet granulation: the study of a continuous twin screw granulator using Positron Emission Particle Tracking (PEPT) technique. *European Journal of Pharmaceutics and Biopharmaceutics*, 81 (3):666–673, 2012.

[69] C. S. Stellema, J. Vlek, R. F. Mudde, J. J. M. de Goeij, and C. M. van den Bleek. Development of an improved positron emission particle tracking system. *Nuclear Instruments and Methods in Physics Research Section A: Accelerators, Spectrometers, Detectors and Associated Equipment*, 404(2-3):334–348, 1998.

[70] A. Buffler, I. Govender, J. J. Cilliers, D. J. Parker, J. P. Franzidis, A. Mainza, R. T. Newman, M. Powell, and A. van der Westhuizen. PEPT Cape Town: a new positron emission particle tracking facility at iThemba LABS. In *Proceedings of International Topical Meeting on Nuclear Research Applications and Utilization of Accelerators*, volume 173. International Atomic Energy Agency, 2009.

[71] A. Ingram, M. Hausard, X. Fan, D. J. Parker, J. P. K. Seville, N. Finn, R. Kilvington, and M. Evans. Portable positron emission particle tracking (PEPT) for industrial use. In *Proceedings of 12th International Conference on Fluidization*, pages 13–17, 2007.

[72] Siemens. *Inside Biograph TruePoint PET/CT*.

[73] V. Y. Panin, F. Kehren, C. Michel, and M. Casey. Fully 3-D PET reconstruction with system matrix derived from point source measurements. *Medical Imaging, IEEE Transactions on*, 25(7):907–921, 2006.

[74] Y.-F. Chang and A. C. Hoffmann. A Lagrangian study of liquid flow in a reverse-flow hydrocyclone using positron emission particle tracking. *Experiments in Fluids*, 56(1):1–14, 2015.

[75] G. B. Saha. *Physics and radiobiology of nuclear medicine*. Springer Science & Business Media, 2012.

[76] X. Fan, D. J. Parker, and M. D. Smith. Labelling a single particle for positron emission particle tracking using direct activation and ion-exchange techniques. *Nuclear Instruments and Methods in Physics Research Section A: Accelerators, Spectrometers, Detectors and Associated Equipment*, 562(1):345–350, 2006.

[77] D. J. Parker, C. J. Broadbent, P. Fowles, M. R. Hawkesworth, and P. McNeil. Positron emission particle tracking — a technique for studying flow within engineering equipment. *Nuclear Instruments and Methods in Physics Research Section A: Accelerators, Spectrometers, Detectors and Associated Equipment*, 326 (3):592–607, 1993.

[78] M. Wang. *Industrial Tomography: Systems and Applications*. Elsevier, 2015.

[79] A. C. Hoffmann, C. Dechsiri, F. van de Wiel, and H. Dehling. PET investigation of a fluidized particle: spatial and temporal resolution and short term motion. *Measurement Science and Technology*, 16(3):851–858, 2005.

[80] Z. Yang, D. J. Parker, P. J. Fryer, S. Bakalis, and X. Fan. Multiple-particle tracking — an improvement for positron particle tracking. *Nuclear Instruments and Methods in Physics Research Section A: Accelerators, Spectrometers, Detectors and Associated Equipment*, 564(1):332–338, 2006.

[81] Z. Yang, X. Fan, P. J. Fryer, D. J. Parker, and S. Bakalis. Improved multiple-particle tracking for studying flows in multiphase systems. *AIChE Journal*, 53(8): 1941–1951, 2007.

[82] Z. Yang, X. Fan, S. Bakalis, D. J. Parker, and P. J. Fryer. A method for characterising solids translational and rotational motions using multiple-positron emission particle tracking (multiple-PEPT). *International Journal of Multiphase Flow*, 34(12):1152–1160, 2008.

[83] G. I. Pisarev, A. C. Hoffmann, W. Peng, and H. A. Dijkstra. Large eddy simulation of the vortex end in reverse-flow centrifugal separators. *Applied Mathematics and Computation*, 217(11):5016–5022, 2011.

[84] G. I. Pisarev, V. Gjerde, B. V. Balakin, A. C. Hoffmann, H. A. Dijkstra, and W. Peng. Experimental and computational study of the "end of the vortex" phenomenon in reverse-flow centrifugal separators. *AIChE Journal*, 58(5):1371–1380, 2012.

[85] A. Gil, C. Cortés, L. Romeo, and J. Velilla. Gas-particle flow inside cyclone diplegs with pneumatic extraction. *Powder Technology*, 128(1):78–91, 2002.

[86] M. E. Casey. Improving PET with HD-PET + Time of Flight. Technical report, Siemens Molecular Imaging, Knoxville, TN, 2008.

[87] B. Jakoby, Y. Bercier, M. Conti, M. Casey, B. Bendriem, and D. Townsend. Physical and clinical performance of the mCT time-of-flight PET/CT scanner. *Physics in Medicine and Biology*, 56(8):2375–2389, 2011.